Department of Physics and Astronomy,
University of Canterbury, Private Bag 4800,

Christchurch, New Zealand

Time distribution analysis

for flasher data and simulations

in the IceCube neutrino detector

A thesis submitted in partial fulfilment of the requirements for the degree of Master of Science

Sarah Bouckoms 84018662

Masters Part II: June 10^{th}, 2011

Supervisor: Dr. Jenni Adams

Abstract

The IceCube neutrino observatory is located in the deep glacial ice below the South Pole. IceCube consists of over $5,000$ photomultiplier tubes regularly spaced throughout a cubic kilometre volume of ice. The photomultiplier tubes are receptive to the light produced by high energy neutrino interactions. As a means of evaluating our understanding of the physics of light propagation, a comparison was made between the data taken from artificial light sources and Monte Carlo simulations of these events. The evaluation was done by comparing the shape of the light arrival-time distributions. The three icemodels compared were the Additionally Heterogeneous Absorption (AHA), South Pole Ice - 1 (Spice) and South Pole Ice - Mie (Spice Mie). The artificial light sources used are LEDs, known as flashers, located within each of the detector modules. The data set used in this study was taken on string 63 with single-photoelectron settings (one LED). Various orientations of the flashing LED and relative position of the light source in the detector, were studied over 15 depths in instrumented ice. Through a χ^2 comparison and distribution characteristics it was found that for the majority of cases, simulations which used the Spice Mie ice model matched the data best. There were, however, some isolated cases in which simulations using the Spice 1 or AHA ice models matched the flasher data best.

Contents

List of Figures

List of Tables

Chapter 1

Preamble

This section is being written after the submission of my thesis. Here I have included some further plots that I have run and details on correcting the run settings.

After examination of this thesis it was discovered that some of the files used to run PPC did not have the parameters which they were believed to have in them. The effect of the changed scripts is in the detail of the results rather than the general conclusions.

When setting the PPC simulation settings for the icemodels, there were several files I altered. There were also files that I did not change, which I did not mention. They were kept the same for all runs. However, one setting, which contained the information was not changed and it should have been changed. Since this discovery new runs have been performed and indeed there is a difference. While it does not change the overall conclusions of the thesis, it should be noted and corrected for those who may continue this work in the future.

The file that should have been changed was the cfg.txt file. This included four different variables: The oversize factor, the DOM efficiency, the HG/SAM % and the g value. The oversize factor is the amount by which the DOM was enlarged to decrease the simulation time. By having a larger target, the number of electrons recieved will reach a higher number in a shorter amount of time. The DOM efficiency is as it says, the efficiency of the DOM. The third variable is the percentage between the Henyey-Greenstein equation and the SAM equation, which were used in combination to make the scattering function. Finally the g value represents $\cos\theta$, the photon scattering angle, in the HG and SAM equations. This was a defining feature between the different icemodels.

The correct values for these settings in the different ice models are in Table 1:

Settings in the cfg.txt file for different icemodels				
ice model	Oversize factor	DOM efficiency	% HG/SAM	g value
AHA	5	0.95	0	0.8
SPICE 1	5	0.95	0	0.8
SPICE MIE	5	1.0	0.45	0.95

1.1 shifted time distributions with chi squared comparisons

Below are the scripts run with the correct settings in the configuration file, cfg.txt as shown in table 1. The number of photons was adjusted to have the same settings as done in the thesis. The time distributions are also shifted to achieve the lowest possible chi squared value. This was done by running the same scripts as on the time distributions in my thesis work. From these plots while a marginal difference may be noted in the plots an exact change is hard to pin down. This is why in the next section a comparison is done between the chi squared values of the runs under different settings. Please note that while the distributions have changed the overall result that the Spice Mie icemodel best fits the data remains uncontested.

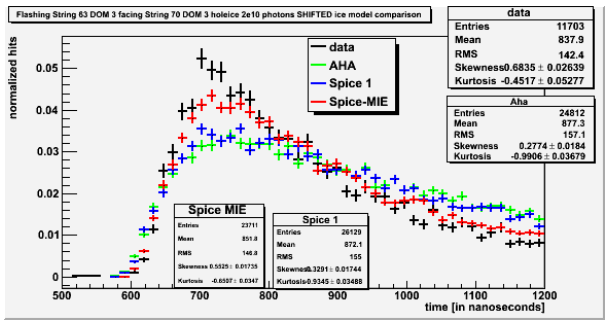

(a) facing across 2e10 photons - χ^2AHA= 13.67, Spice 1 = 11.425, Spice Mie = 2.817

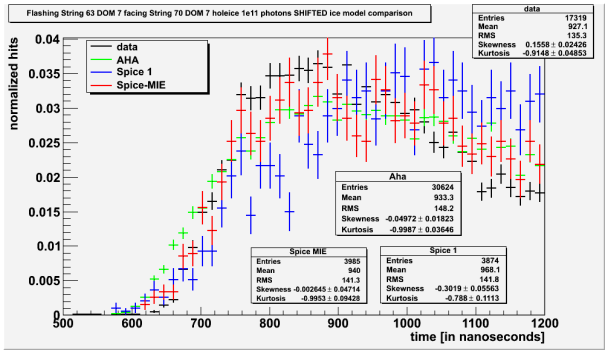

(b) facing across 1e11 photons - χ^2AHA= 8.18, Spice 1 = 5.71, Spice Mie = 1.91

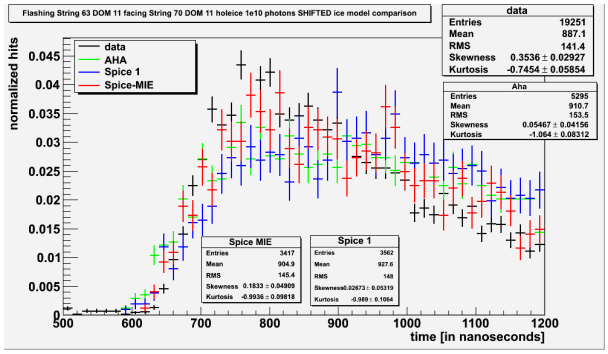

(c) facing across 1e10 photons - χ^2AHA= 5.53, Spice 1 = 4.42, Spice Mie = 2.33

Figure 1.1: Post Thesis Studies Flasher data and icemodel comparison flashing String 63 facing String 70 receiving directly across χ^2.

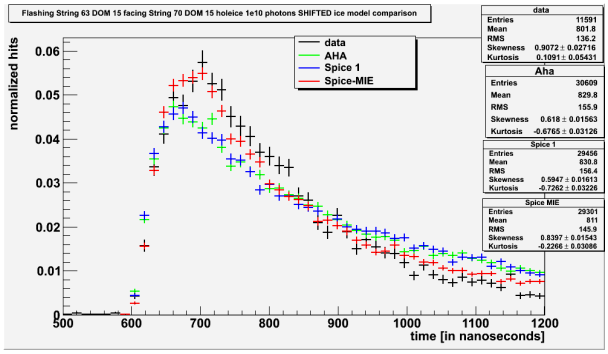

(a) facing across 1e10 photons - χ^2AHA= 8.73, Spice 1 = 9.38, Spice Mie = 3.11

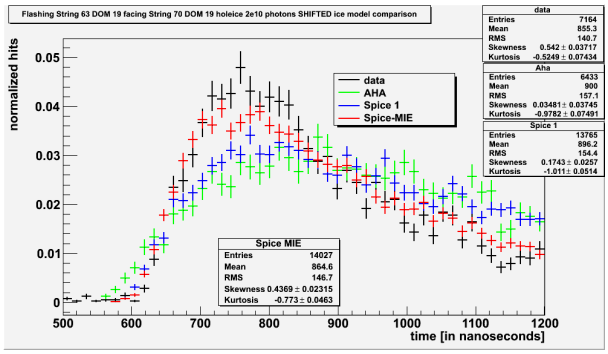

(b) facing across 2e10 photons - χ^2AHA= 8.408, Spice 1 = 7.27, Spice Mie = 2.49

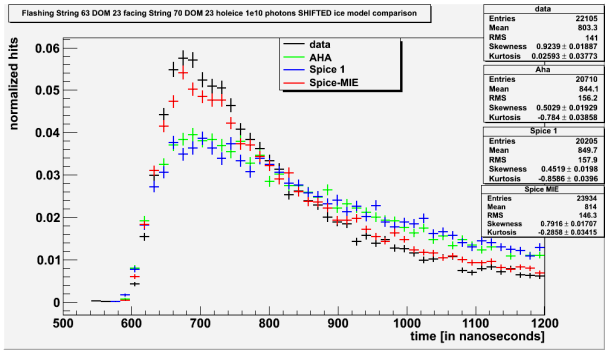

(c) facing across 1e10 photons - χ^2AHA= 17.8, Spice 1 = 21.453, Spice Mie = 2.88

Figure 1.2: Flasher data and icemodel comparison flashing String 63 facing String 70 receiving directly across χ^2

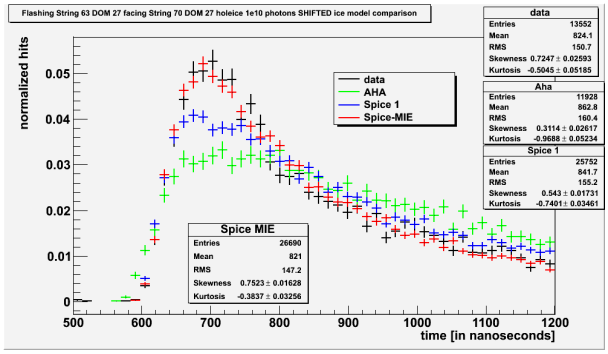

(a) facing across 1e10 photons - χ^2AHA= 11.45, Spice 1 = 4.55, Spice Mie = 1.71

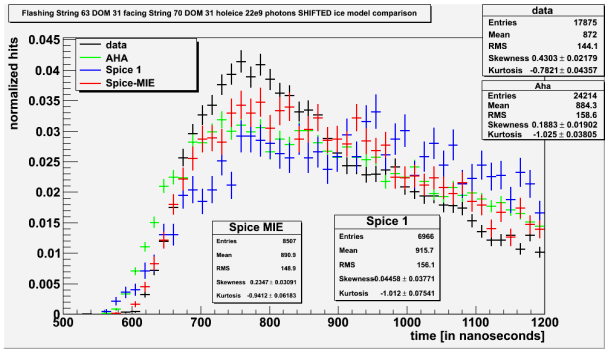

(b) facing across 22e9 photons - χ^2AHA= 11.69, Spice 1 = 11.19, Spice Mie = 2.95

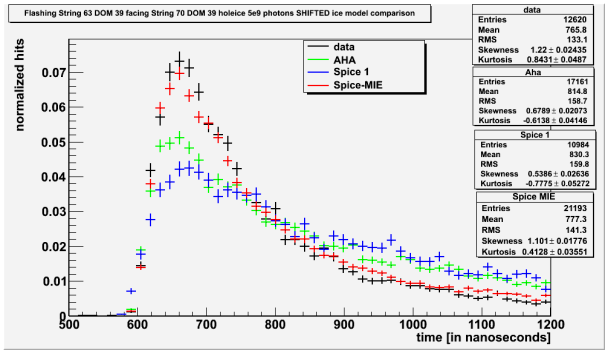

(c) facing across 5e9 photons - χ^2AHA= 16.11, Spice 1 = 23.2, Spice Mie = 1.96

Figure 1.3: Flasher data and icemodel comparison flashing String 63 facing String 70 receiving directly across χ^2

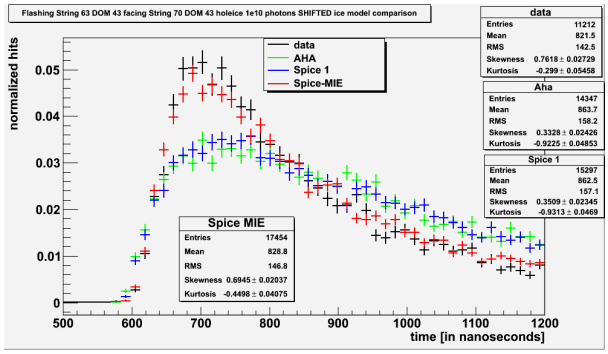

(a) facing across 1e10 photons - χ^2AHA= 11.74, Spice 1 = 10.5, Spice Mie = 1.68

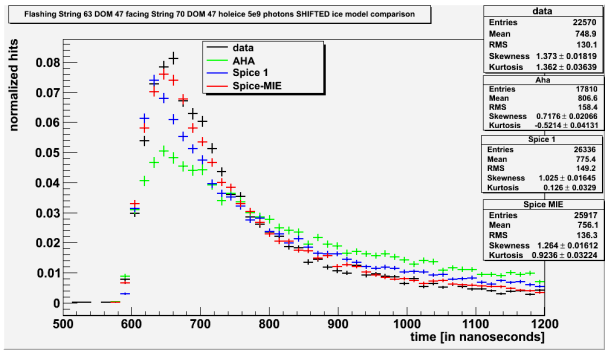

(b) facing across 5e9 photons - χ^2AHA= 30.7, Spice 1 = 12.92, Spice Mie = 2.83

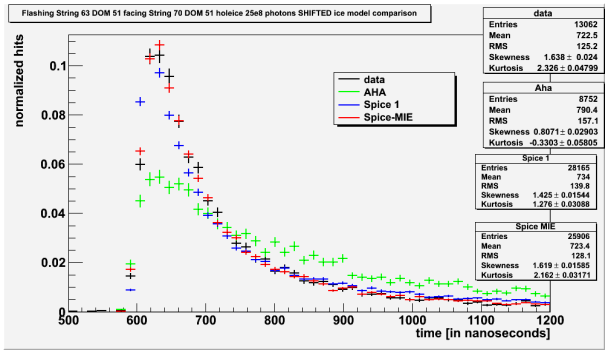

(c) facing across 25e8 photons - χ^2AHA= 24.375, Spice 1 = 6.02, Spice Mie = 1.44

Figure 1.4: Flasher data and icemodel comparison flashing String 63 facing String 70 receiving directly across χ^2

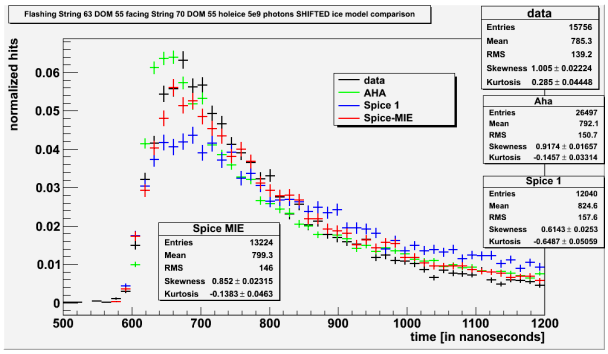

(a) facing across 5e9 photons - χ^2AHA= 7.97, Spice 1 = 10.07, Spice Mie = 2.36

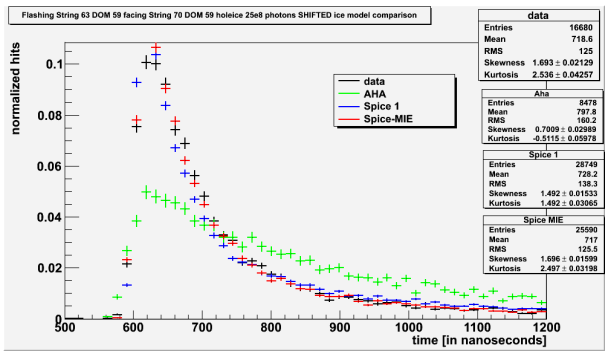

(b) facing across 25e8 photons - χ^2AHA= 37.11, Spice 1 = 7.51, Spice Mie = 1.87

Figure 1.5: Flasher data and icemodel comparison flashing String 63 facing String 70 receiving directly across χ^2

1.2 chi2 comparison plots

While these plots are useful, as found in my thesis, conducting a statistical analysis test is of more use. In this section, a comparison is made between the chi squared values found in my thesis and those found in the post thesis study. The first plot, Figure 1.6a shows the time distributions with no shifts where as 1.6b shows the shifted data. Th ice plots below show that the most significant changes are found in the AHA and Spice 1 icemodel. Spice Mie shows very little change in the shifted and non-shifted time distributions. This would lead to confirmation that I simulated all the runs with the configuration files meant for Spice Mie.

Figure 1.6a and Figure 1.6b show the results with all three icemodels overlapping. This is useful for an overall comparison, it does not clearly display the differences in each individual icemodel. Further below, Figure 1.7 a, b, and c, show the shifts for each individual icemodel, AHA, Spice 1 and Spice Mie respectively. Separating the icemodels gives a clear representation for each one. It is not obvious that any patterns can be detected with the changes in the configuration file however, there does appear to be a larger change in the deeper ice.

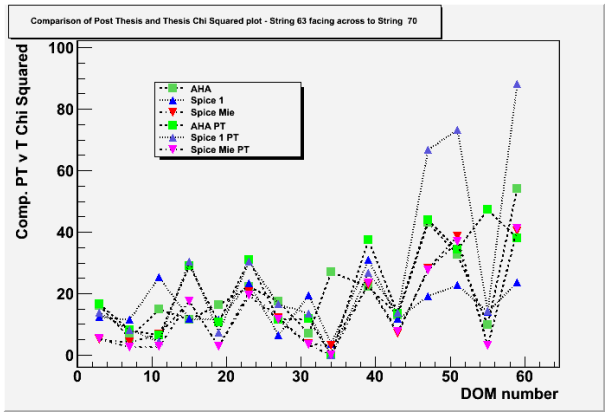

(a) facing across

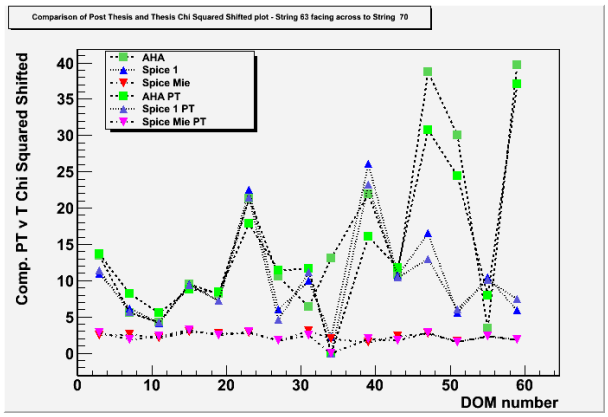

(b) facing across shifted

Figure 1.6: Post thesis v thesis results: String 63 facing String 70 receiving directly across χ^2

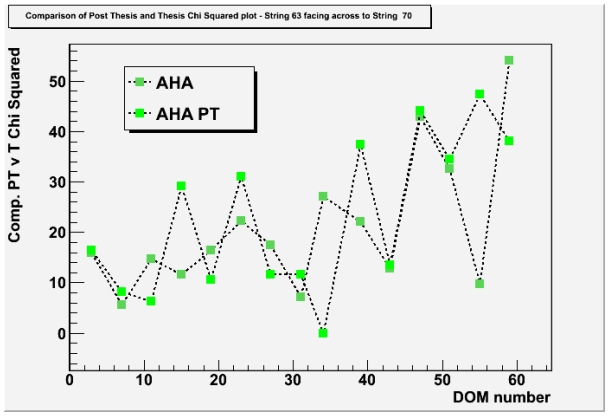

(a) facing across aha

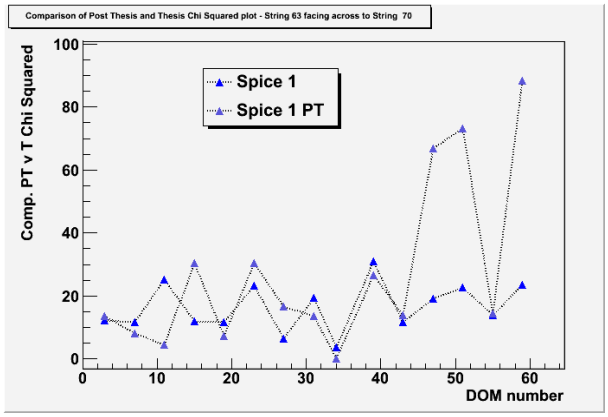

(b) facing across sp1

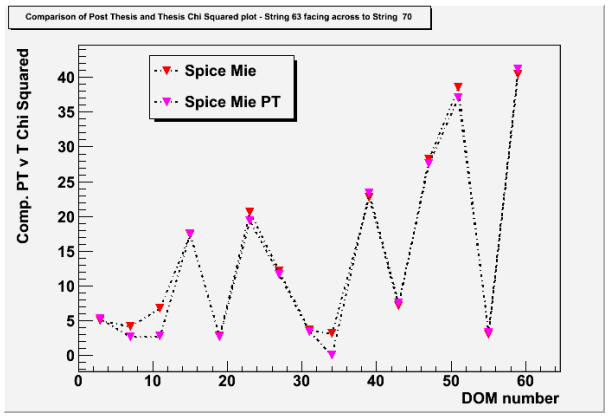

(c) facing across mie

Figure 1.7: Post thesis v thesis SHIFTED results expanded: String 63 facing String 70 receiving directly across χ^2

Chapter 2

Physics of neutrinos and detection principles

2.1 Introduction

In the 1770s when James Cook crossed below 60 degrees south into the Southern Ocean he declared the territory so horrible to the extent that "the world will derive no benefit from it" [1]. Scientists have proven Captain Cook wrong by conducting experiments in the extreme environment of Antarctica. IceCube, the largest neutrino observatory, is a prime example of this. At the South Pole, IceCube has been built to detect high-energy neutrinos of astrophysical origin. The observatory is primarily a grid of light-receptive detectors deployed into holes drilled in the ice. Results from IceCube will contribute to a wide variety of fields including astronomy, cosmology and particle physics.

Before confirmation of their discovery, neutrinos were referred to as the "ghost particles" or "the little one that is not there" [2]. Originally proposed in 1930 by Wolfgang Pauli, neutrinos were his solution to energy inbalance in beta decay [3]. They are so elusive that they remained undiscovered for 26 years after Pauli's postulation.

In 1956 Clyde Cowan and Fred Reines detected the first neutrino. They worked with a 33 m^3 liquid detector surrounded by 13 m to 20 m of paraffin (kerosene) and lead to diminish background radiation [4]. They detected a positron and neutron pair originating from a collision between a neutrino and proton [5].

To detect neutrinos of higher energies, larger neutrino detectors were required to compensate for lower fluxes [6]. By 1965 neutrino observatories had grown such that they were able to detect the first atmospheric neutrinos [7]. Detection mediums diversified to include huge vats of liquid chemicals placed in mine shafts and submarines. Nonetheless, these were by modern standards, small scale observatories, only practical for observing solar and atmospheric neutrinos which have a high flux. At higher energies, the interaction cross section is larger, however there is a lower expected flux of neutrinos [8]. It is

estimated that at high-energy, on the order of PeV, the flux can decrease to a rate of two events a year in one km^2 area [9].

To combat the low flux of high-energy neutrinos a larger detector is needed. It is impractical and expensive to build a detector of liquid chemicals large enough to feasibly study high-energy neutrinos. Ice fulfilled the requirements for a new detection medium. The large quantities of pure glacial ice available at the South Pole is an ideal medium for neutrino detection as ice is a large, transparent and inexpensive medium.

The first high-energy neutrino detector built at the South Pole was the Antarctic Muon And Neutrino Detector Array (AMANDA). AMANDA was the predecessor of the larger neutrino observatory, IceCube. Both AMANDA and IceCube were created by drilling deep holes into the ice, lowering strings into the holes and allowing the ice to refreeze. In the cubic kilometre array, IceCube has over $5,000$ detectors attached to the strings. The array of detectors stretches from $1,400$ m to $2,450$ m below the surface ice. The density of dust particulates varies throughout the instrumented volume of ice. Dust is naturally airborne by volcanic eruptions, sandstorms or various other climatic phenomena. The dust in the ice of the detecting region of IceCube was deposited in the late Pleistocene era [10] and over this time the dust levels varied irregularly. The amount of dust particulates present in a given layer of ice greatly affects light propagation, which is the primary detection method. In order to correctly quantify the light from a neutrino interaction, a good understanding of the ice is important.

The rest of this chapter continues with a discussion on applicable background physics, Chapter 3 discusses other particle detectors. Chapter 4 explains the ice properties relevant to light propagation, including absorption, scattering, and the characterization of these properties which are the quantities tabulated as a function of depth to form a particular model. Chapter 6 presents the results which are then discussed in Chapter 7. Chapter 8 explores a systematic study of the angle of the LEDs followed by the conclusion.

2.2 The neutrino

Neutrinos are very elusive as they have virtually no mass and no electric charge, with interactions limited to those of the weak force. They are one of six spin-half elementary particles included in the lepton family [11]. Neutrinos have an intrinsic property called flavour. These flavours consist of the electron, muon and tau neutrino. While the sun only produces electron neutrinos, most of the astrophysical objects targeted by IceCube are expected to produce neutrinos with a $1:2:0$ flavour ratio [12–16]. Over astronomical distances oscillations between flavours occur generally producing a $1:1:1$ ratio [17]. IceCube is looking for high-energy neutrinos of all flavours above 1×10^{10} eV from astrophysical origins [13].

2.3 Charged current and neutral current interactions

When a neutrino interacts with a nucleon it can do so via a neutral current (NC) interaction, when a Z^0 boson is exchanged, or a charged current (CC) interaction, with a $W^{\pm}$ boson exchange. Both bosons are carriers of the electroweak force [3]. From either reaction, a hadronic cascade is produced when energy is transfered from the neutrino to the quarks of the nucleons. The debris from the nucleon hadronises and secondary interactions produce a cascade of particles. This cascade is referred to as a hadronic cascade as its inititiating particles are hadrons. In a NC interaction the path of the neutrino is minimally deflected, and the neutrino remains intact with approximately 25% energy loss [6]. If there is a CC interaction then a charged lepton of the associated flavour is created carrying 50% to 80% of the neutrino's energy [16]. The lepton particle will behave differently depending on the flavour, as discussed later in this chapter.

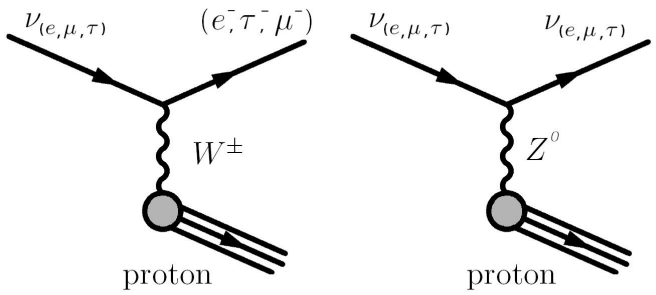

(a) Charged Current (b) Neutral Current

Figure 2.1: Neutrino interactions of neutral current and charged current. The neutrino interacts with atomic nuclei and the bosons transfer the energy to a hadronic cascade and the outgoing lepton. The nature of the outgoing lepton depends on the type of interaction and the flavour of the incoming neutrino.

2.4 Cerenkov radiation

Methods of neutrino interaction are indirect in that they involve studying the products of a neutrino interaction rather than relying on the neutrino to interact with the detector itself. One method of detecting relativistic particles is through the observation of Cerenkov radiation. Cerenkov radiation is created when the velocity of a charged particle is greater than the local speed of light in the medium,

$$v > c/\sqrt{\epsilon(\omega)}, \tag{2.1}$$

where $\epsilon(\omega)$ is the macroscopic dielectric constant [18]. The Cerenkov radiation appears as a wave front of light following the particle in a conical fashion as depicted in Figure 2.2. The angle is given by,

$$\cos\theta = 1/\beta\sqrt{\epsilon(\omega)}. \tag{2.2}$$

In ice the angle is approximately 41 degrees, the signature angle of Cerenkov radiation [16, 19]. This cone of radiation is most intense at higher frequencies and can be detected by photomultiplier tubes.

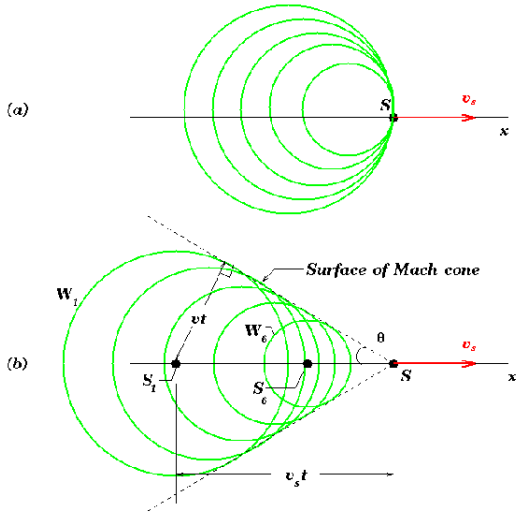

Figure 2.2: Cerenkov radiation.

2.5 Signatures

As mentioned in Section 2.3 a neutrino interacting with a nucleon results in a hadronic cascade. The charged particles in the hadronic cascade produce Cerenkov radiation which may be observed. If the interaction is neutral current, then the hadronic cascade is the only visible product as the neutrino will escape undetected. If, on the other hand, it is a charged current interaction, a charged lepton of the same flavour as the neutrino is produced. Each of these charged leptons has unique interactions in the ice resulting in a different light pattern and detection signature. The three flavours are discussed below.

2.5.1 Electron signature

A charged lepton such as an electron can initiate an electromagnetic cascade which proceeds through bremsstrahlung radiation and pair production. Bremsstrahlung radiation is produced when a particle is deflected and produces a photon [18]. The photon then produces an electron and positron pair (see Figure 2.3). The electrons and positrons produce further bremsstrahlung photons and pair production continues in a cascading effect. The cascade continues until the energy of the particles decreases to a

level insufficient for pair production and then energy lose by ionization occurs. As with all the charged leptons, the Cerenkov emission and track length vary depending on the energy of the initial particle [6].

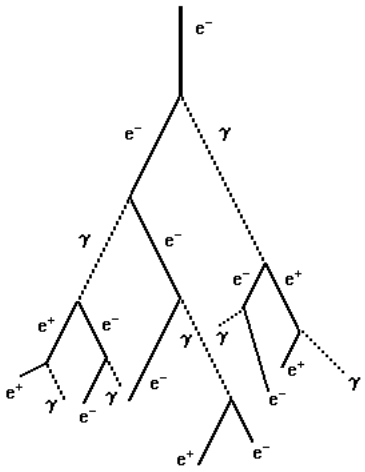

Figure 2.3: Electron and positron pair production creating bremmstrahlung radiation in cascades.

The Cerenkov light emitted by the cascade is initially in a cone whose angle is given by the Cerenkov angle. However, for all but ultra-high energies, the overall length of the cascade is relatively short in comparison with the spacing of the IceCube detector strings. This means that the light from a cascade is essentially emitted from a point-source region. Scattering of the light then leads to cascades appearing spherical, with centre around the interactoin vertex [17], making directional information from the incident neutrino difficult to decipher.

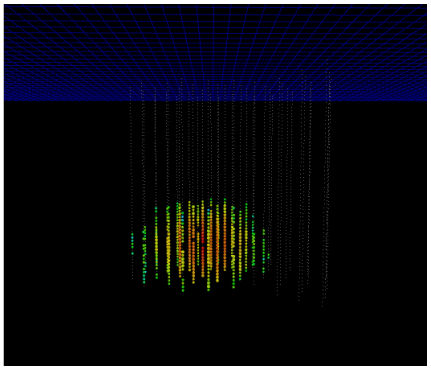

Figure 2.4: Electron cascade originating at DOM 50 in the detector from Monte Carlo data.

2.5.2 Muon signature

The muon does not interact as readily as an electron so it can travel long distances in the ice. The muon has the longest track length of any of the flavours, ranging up to several kilometres. A muon's lifetime is

long enough such that as it interacts, it leaves a trail of electrons and positrons along the path it takes. For a muon, the main light output is its own Cerenkov radiation. The light detected from a muon track will also include Cerenkov radiation from stochastic processes such as bremmstrahlung radiation that initiates a mini shower.

The differences in the light distribution makes the electron cascade-like signature distinctly different from the muon's track-like signature.

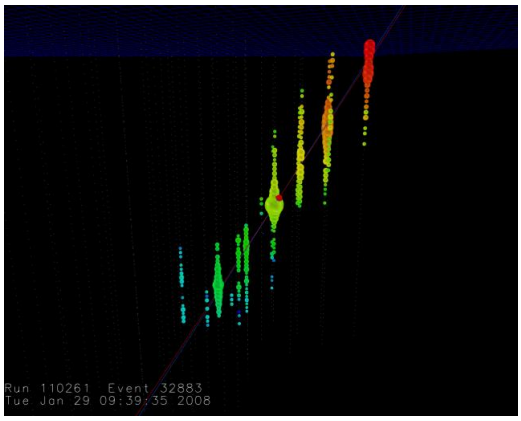

Figure 2.5: A Muon track in IceCube detector.

2.5.3 Tau signature

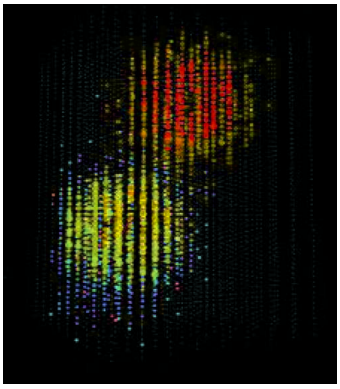

Figure 2.6: A simulated double-bang event with an energy of a few PeV in IceCube. Coloured circles represent hit channels, with red circles hit earliest and violet circles latest. Circle size corresponds to number of detected photons [8].

The last flavour of lepton to be discovered was the tau. The short track length, on the order of tens of metres, allows both the initial vertex cascade and electromagnetic or hadronic cascade from tau decay to occur within the detector. This two-cascade signature is referred to as a double bang and is displayed in Figure 2.6). Tau neutrino events have not yet been observed in IceCube.

Chapter 3

Neutrino detectors

In the 1970s neutrino detectors were huge vats of expensive chemicals built far below the surface of the earth. These detectors targeted reactor, solar and atmospheric neutrinos. Higher energy neutrinos are expected to orginate from the same sources that produce high-energy cosmic rays. In the 1980s development towards neutrino detectors which might be able to detect astrophysical neutrinos began. The low expected fluxes dictates the size of the instrumented volume and the optimal spacing of the photomultiplier tubes. The greater the energy of neutrinos which are targeted then the greater spacing between optical modules which will suffice. In most cases the detectors were optimised to detect neutrinos with energies upward of 10 TeV. Studying high energy neutrinos will allow scientists to better understand extragalactic objects capable of accelerating particles to such high energies. However for dark matter searches, which look for neutrinos produced from the annhilations of dark matter particles collected in the centre of the sun or earth, then a lower energy range of neutrinos is expected. A closer spacing of the optical detectors is needed to be able to detect neutrinos from this source.

The first observatory to study neutrinos through optical detection was the Deep Underwater Muon and Neutrino Detection (DUMAND) project. This group of international scientists used the deep sea near Hawaii as a medium for studying particles from astrophysical origin. This was done by using photomultiplier tubes to detect Cerenkov radiation emitted by muons produced in neutrino interactions with the surrounding water [20]. Shortly after deployment of the photomultiplier tubes in the water a leak occurred causing the project to be canceled in 1995 [21]. Ground breaking results in research and development by DUMAND lead to the next high energy neutrino telescopes.

The Baikal Deep Underwater Neutrino Telescope (BDUNT) was one of the first successful neutrino telescopes to be built in water. It is located deep below the surface of Lake Baikal in Siberia [22]. The telescope was constructed between 1998 and 2003 [23] and is still recording data today. The telescope has

an umbrella-like structure with 11 cable strings suspended with weights attached to maintain a vertical direction [23, 24]. Just over 200 optical modules are deployed [23].

3.1 Neutrino telescopes in the Mediterranean Sea

Much of the focus for astrophysical neutrino detection, located in Europe, has been in the Mediterranean. The Cubic Kilometre Neutrino Telescope (KM3NeT) [25] is the name given to a kilometre-scale detector planned to rival IceCube in sensitivity. The KM3NeT collaboration is made up of groups who have been working on three separate efforts. The three projects are the Neutrino Extended Submarine Telescope with Oceanographic Research (NESTOR) [26], the NEutrino Mediterranean Observatory (NEMO) [27] and the Astronomy with a Neutrino Telescope and Abyss environment RESearch group (ANTARES) [28]. Each has focused on different locations and detection strategies with the KM3NeT design planned to take the best aspects from all three. In the next sections each of these three projects will be outlined along with the current plans for KM3NeT.

NESTOR is a collaboration of scientists formed in 1989 to begin theoretical work for the neutrino experiment [29]. The NESTOR observatory is located 15 nautical miles off the coast of Pylos, Greece [30]. The main structure of NESTOR consists of a tower with layers containing six arms each with two photomultiplier tubes attached. Like the telescopes already introduced, NESTOR is designed to detect Cerenkov radiation produced by muons as a result of neutrino interactions.

The NEMO group, consisting of 100 Italian scientists was formed in 1998 [27, 31]. This group set out to locate and test the best site, equipment and tools necessary for the success of a cubic kilometre detector. The NEMO group proposed the southernmost coast of Sicily, Capo Passero on the abyssal plateau in the Ionian Sea [31]. From December 2006 to May 2007, a small tower was deployed with four layers, each with two groups of two optical modules.

ANTARES is piloted by over 150 European collaborators [28]. The site for the detector, 40 km [24] off the French coast South of Toulon, was chosen as it is able to view the galactic center 67% of the time [32]. ANTARES construction began in 2001 [33]. The first detector line was deployed in February 2006 and operational by March that year [34]. 12 string with groups of optical modules, totally $1,000$, have been fully operational since 2008 [28].

A giant cubic kilometre detector is the next logical step with the expereince gained from smaller telescopes helping to develop best practice for deep sea neutrino telescopes. The pilot projects ANTARES, NEMO and NESTOR [35], along with other European research groups, have formed the Cubic Kilometre Neutrino Telescope (KM3NeT) collaboration. The objectives of KM3NeT are similar to previous detectors. High energy neutrino and particle physics will be extended to new levels with higher energy

and angular resolution provided by the larger detector. The plans of KM3NeT are still being negotiated.

Between IceCube and KM3NeT, both northern and southern hemispheres will be observed allowing a whole sky survey to be produced. KM3NeT is planned to exceed IceCube's sensitivity with the improved optical qualities of sea water over Antarctic ice. The detector hopes to take advantage of the low light scattering to obtain high angular resolution with low background noise [35]. The size of the observatory will also allow for higher energy neutrino detection.

3.2 Neutrino telescopes in Antarctica

The advancement of technology has allowed for neutrino telescopes to be built in more and more remote locations. This is epitomized deep in the ice sheets of Antarctica. Working in Antarctica brings a diverse range of difficulties: scientist support, transportation, and coping with an extreme environment. However, the remote location offers many benefits for neutrino observing such as low background radiation, stable optical properties, and most importantly, a large inexpensive medium [36]. Economic constraints have previously limited the building of an observatory large enough to detect ultra high-energy neutrinos. Thus using a naturally occurring medium is ideal. Placing the telescope directly at the South Pole was optimal for logistical support offered by the Amundsen-Scott South Pole Station. The discussion thus far has been based around detectors in large bodies of liquid water, but now we turn to the focus of this thesis, a neutrino detector built in Antarctic ice.

The first Antarctic and largest neutrino telescope at the time was AMANDA, the Antarctic Muon And Neutrino Detector Array. See Figure 3.1 for a scale diagram showing AMANDA and IceCube. AMANDA's size allowed for the detection of the highest energy neutrinos yet [37]. As with many astronomy projects, working with a new detection medium provided insight and rasied problems that were not initially anticipated.

After several years of preparation, the construction of AMANDA began in 1993 with an exploratory phase [38]. Known as AMANDA-A, this first stage consisted of four strings of detectors deployed between 800 m and 1,000 m [38]. Due to the large amount of scattering caused by air bubbles in the ice at such a shallow depth, the second phase, AMANDA-II was deployed at a depth of 1,545 m to 1,978 m. Upon completion in 2000 there was a total of 677 detectors frozen into the ice [15]. Its final shape covers a cylinder with a height of 500 m and diameter of 200 m [39] to encompass 1.6×10^7 m^3 [15]. In this larger configuration, approximately 1,000 neutrino events per year were recorded [13].

The detectors were pressurized glass spheres enclosing photomultiplier tubes designed to detect Cerenkov radiation. This method has allowed for the study of neutrinos in the energy range in the GeV to EeV range [36].

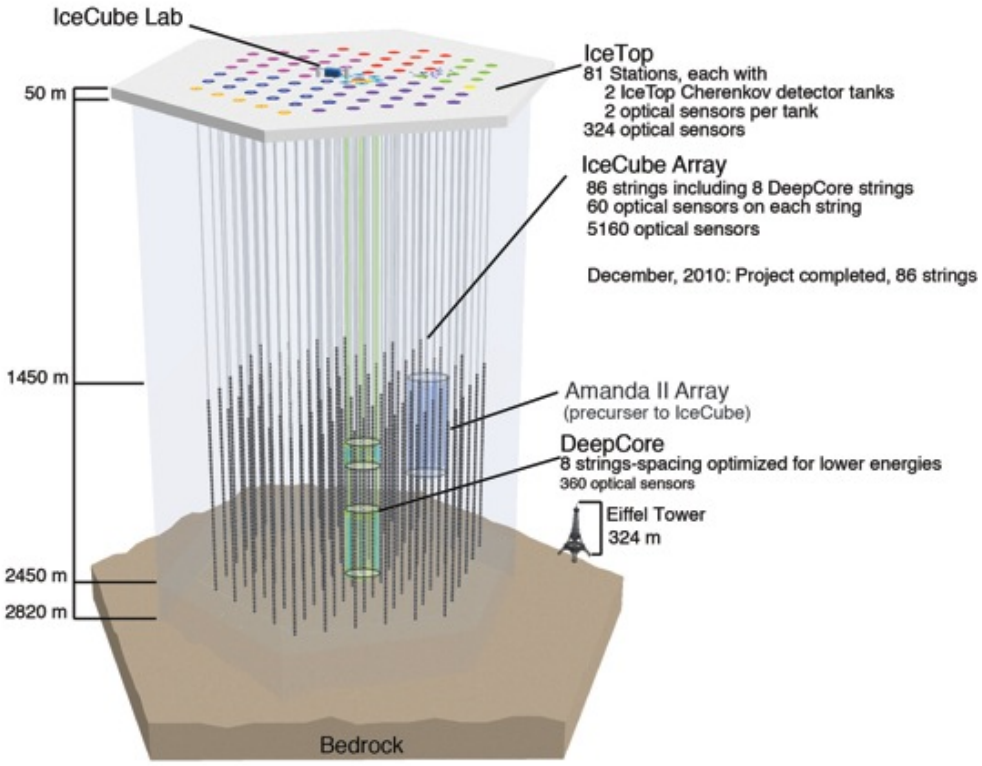

Figure 3.1: Image of the IceCube neutrino Observatory with the precursor AMANDA.

The absorption length of light in ice was found to be around 100 m whereas it is only a few metres in sea ice or laboratory ice [37]. This provides for remarkably good seeing conditions. The effects of air bubbles and dust particulates were also investigated. A significant increase in particulates was located between $900 - 1,000$ m deep. This increase is believed to be caused by an increase in dust concentrations during the last ice age [37].

Due to the advancements made with AMANDA, motivation increased for a neutrino observatory of larger scale, further extending the flux of neutrinos which could be investigated. Improvements to AMANDA were made in the design, construction methods and electronic hardware. These were then tested in prototype strings within the AMANDA configuration [40]. With the success of the prototype testing, the next generation of neutrino detectors continued to grow.

Completed on December 18, 2010, the newest neutrino telescope, IceCube, lies beneath the surface of the ice at the South Pole, Antarctica. Despite being such an inhospitable environment for humans, the Antarctic ice is an ideal medium for detection as it is a large, economical, transparent medium for light propagation.

The logistical support is provided by the United States Antarctic Program. The National Science

Foundation (NSF) and US Congress are the primary financial supporters of the project, providing several hundred million US dollars. The experiment is coordinated by the IceCube collaboration, an international team of over 200 scientists.

Due to the nature of Antarctica, the working season is limited to early October till late February. During that period, construction of the detector is carried out. Using an enhanced hot water drill, a team of engineers deployed a total of 86 strings with cables allowing communication between the detectors and the surface. Each hole takes approximately 40 hours to drill and 11 additional hours to deploy each string [13].

Each string is equipped with 60 detectors in the form of Digital Optical Modules (DOMs) contained in netball sized spheres made of borosilicate glass. Each DOM consists of a main-board circuit, and a PhotoMultiplier Tube (PMT). Evenly spaced around the board are 12 flashers or light emitting diodes (LEDs), used to simulate light sources in the ice. Before shipment, each sphere is tested to $10,000$ psi to ensure it can withstand the pressure of the deep ice. Along each string the DOMs are placed between $1,450$ m and $2,450$ m below the surface of the ice. The distance between strings varies between 111.5 m and 155.2 m, and they are on average at 125 m apart. The vertical distance between each DOM is 17 m. In total, there are $5,160$ DOMs spread throughout a cubic kilometre [8].

IceTop is a surface air shower detector designed to detect cosmic rays. It extends the detectable energy spectrum to neutrinos greater than 300 TeV. Kept on the surface above each string, IceTop is made of tanks with two DOMs frozen in place. IceTop can also be used for calibration purposes [16]. To detect neutrinos of lower energies, down to 10 GeV, an extra six strings are drilled into the heart of IceCube; this denser configuration is known as DeepCore. As well as extending the energy range, DeepCore is also used to veto atmospheric neutrino events and calibrate for the background of atmospheric neutrinos [16].

Environmental impacts

The science conducted in Antarctica comes at a price: apart from the monetary value, there is also a negative environmental impact. In order to preserve the unique environment of Antarctica for future generations, the Antarctic Treaty was adopted in 1959 [41]. This document calls for the use of the Antarctic Treaty Area solely for "peaceful purposes" (Article I) and "scientific investigation" (Article II) [41]. An additional document, the *Protocol on Environmental Protection to the Antarctic Treaty* was written in 1991 to 'protect the Antarctic environment and dependent and associated ecosystems' [42]. In Article 11 the Committee of Environmental Protection (CEP) was appointed while Article 8 strengthens and clarifies the definition of environmental impact [42]. Depending on the degree of impact of proposed activities, different procedures must be followed. Annex 1 outlines the procedures for a 'more than minor or transitory impact'. The Antarctic Treaty System obliges parties to investigate impacts of scientific activity. In the case of IceCube, the National Science Foundation prepared a preliminary environmental assessment, then a more thorough evaluation was required in the form of a Comprehensive Environmental Evaluation (CEE). This report required a description of the activity including location, duration, cumulative effects, possible amendments, uncertainties and accident management. Construction impacts were also included, such as the amount of fuel used, the estimated number of persons on the ice and aerosols emitted into the air [43]. It also required an in-depth account of IceCube's goals and motivation. In August 2004, the report was made freely available and submitted to the CEP for review at the Antarctic Treaty Consultative Meeting. Proposed suggestions were incorporated into the document and it was believed that while the impact from the activities would be great, the science was justifiable [43]. Regular monitoring and inspections have taken place since the beginning of construction to verify predicted impacts. By following this procedure, IceCube has complied with all necessary regulations set forth by the Antarctic Treaty System.

Chapter 4

Properties of the Ice

The South Pole ice is of greater purity than any laboratory ice [44, 45]. Despite this there are still many particulates, such as soot, dust grains, and sea salts deposited in the ice [10]. Different climatic periods or geological events, such as volcanic eruptions, influence the number of particulates present in the atmosphere. As the particulates settle they become frozen in the ice. The compacted ice has varying types and densities of particulates resulting in stratified regions in the IceCube detector.

The particulates affect the way light propagates through the ice. They affect the light through absorption and scattering, which changes the path of the photons. As there are many different types of particulates it is not straightforward to related the amount of absorption with the amount of scattering [10]. For instance, particulates such as sea salt crystals and liquid acid drops have high scattering rates but very minimal absorption; conversely, soot has high absorption but causes little scattering [10]. Thus to understand the complex nature of light propagation in ice, not only does the density of the particulates need to be accounted for but also the type of the particulates. An accurate description of light propagation in different regions of the ice is vital to be able to accurately characterise the origin and energy of detected neutrinos.

4.1 Absorption

The absorption of a medium is characterised by the absorption length, defined as the distance a photon travels before the survival probability decreases to $1/e$. The absorption length is often expressed through its reciprocal, the absorption coefficient. Figure 4.1 plots the absorption coefficient as a function of depth for the three ice models used in this study. A model of wavelength dependent absorption is given,

$$a(\lambda) = A_U e^{-B_u \lambda} + C_{dust} \lambda^{-\kappa} + A_{IR} d^{-\lambda_o/\lambda}. \tag{4.1}$$

The second term, C_{dust}, maps the concentrations of dust as it varies with depth. The dust grain size and composition are represented by κ. The first and third term describe absorption of light caused by ice. The first term focuses on the effects at the ultraviolet end of the electromagnetic spectrum, whereas the third term focuses on the far infrared end of the electromagnetic spectrum. In the ultraviolet range, a phenomena knows as "Urbach tail" is described; however, since IceCube is sensitive to wavelengths greater than 300 nm, this term is negligible [10] and the equation can be written as such:

$$a(\lambda) = C_{dust}\lambda^{-\kappa} + A_{IR}d^{-\lambda_\circ/\lambda}. \tag{4.2}$$

4.2 Scattering

Scattering describes the deflection of photons as they interact with the air bubbles or particulates in the ice. Most of the scattering in the upper ice is caused by air bubbles. Below 1350 m, the air bubbles are compressed into air-hydrate crystals due to the increased pressure [10]. This is one of the main motivating factors for locating IceCube below this depth. Wide distributions of photon arrival time show that for large distances the photons undergo many scatterings [45]. The distance over which the randomization of the scattering angle occurs is called the effective scattering length, λ_e and is given by

$$\lambda_e = \frac{\lambda_s}{(1 - \langle\cos\theta\rangle)}, \tag{4.3}$$

where $\langle\cos\theta\rangle$ is the average cosine of the scattering angle and λ_s is the geometric scattering length. When the scattering is anisotropic, the effective scattering length is much greater than the geometric scattering length ($\lambda_e >> \lambda_s$). The effective scattering coefficient for each ice model is plotted in Figure 4.2.

Since the wavelengths used are similar in size to the spherical particles, Mie theory can be used to describe the scattering. The Henyey-Greenstein function is most appropriate to describe the scattering angle distribution as the light emitted from a source is scattered in the forward direction [46]. The Henyey-Greenstein scattering angle function is:

$$p(\cos\theta) = \frac{1}{2}\frac{1 - \langle\cos\theta\rangle^2}{(1 + \langle\cos\theta\rangle^2 - 2\langle\cos\theta\rangle\cos\theta)^{3/2}}. \tag{4.4}$$

For values where $\langle\cos\theta\rangle = 1$, the light is mostly scattered forward. When $\langle\cos\theta\rangle = 0$ the scattering is isotropic and when $\langle\cos\theta\rangle = -1$, the scattering is backwards [46]. In the IceCube detector, the values of $\langle\cos\theta\rangle$ used to describe the scattering of particulates in ice are between 0.8 and 0.94 [47].

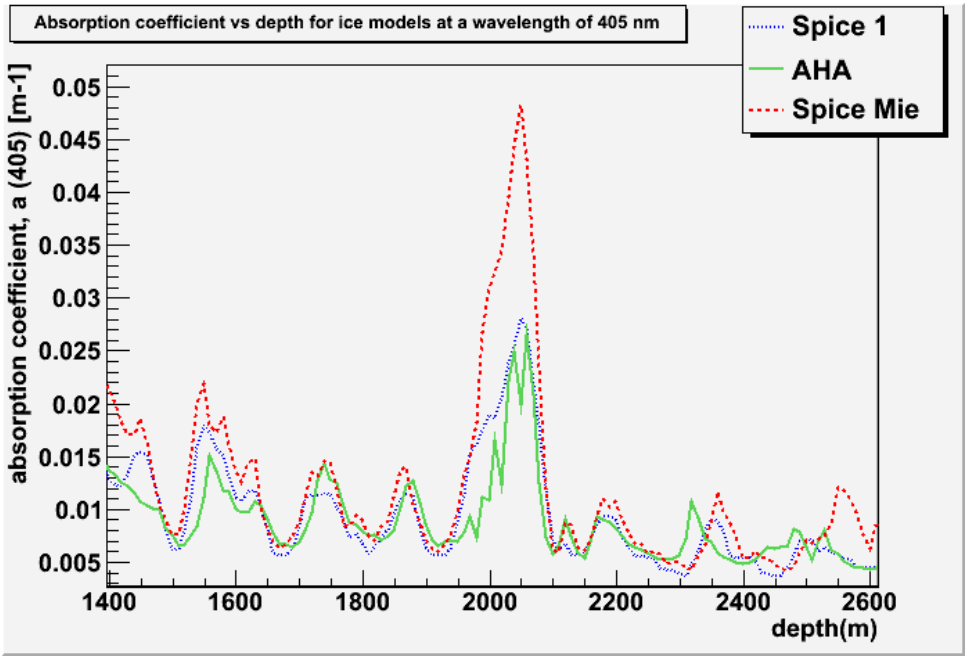

Figure 4.1: Comparisons of absorption coefficient of different ice models at a 405 nm wavelength.

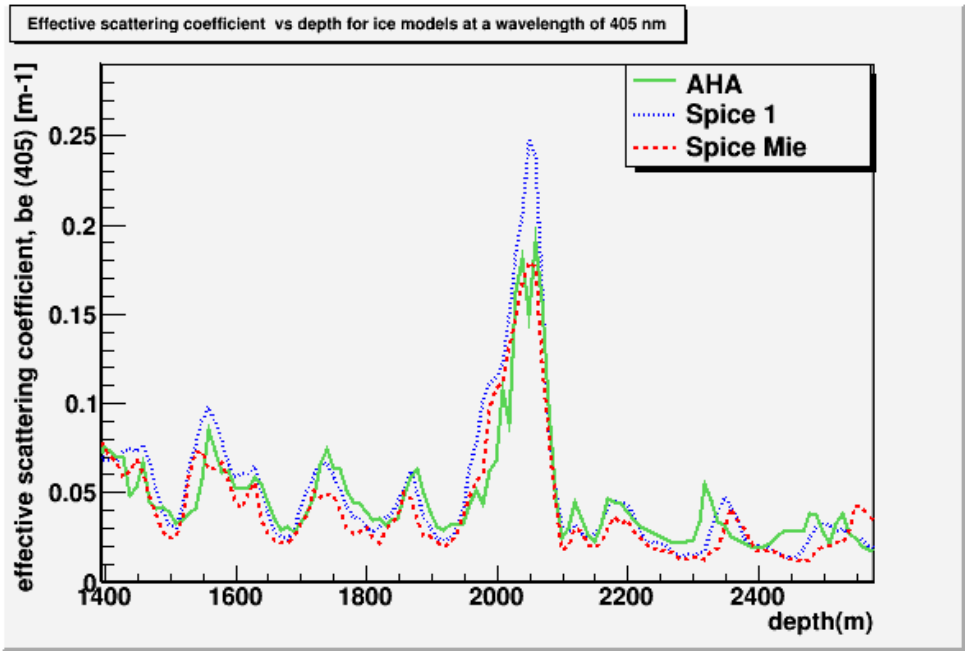

Figure 4.2: Comparisons of the effective scattering coefficient of different ice models at a 405 nm wavelength.

4.3 Six parameter ice description

The absorption and scattering properties are dependent on the size, type of particulate, dust concentration, scattering angle and wavelength. To describe the wavelength and depth dependent scattering and absorption properties of the South Pole ice, a six parameter model is used.

The first two of the six parameters, are the absorption and scattering coefficients at 400 nm $\lambda_a(400)$ and $b_e(400)$. This wavelength is chosen as it is approximately the wavelength of the artificial light sources which were used to investigate the ice properties. The remaining four variables, α, κ, A_{IR} and a_{dust}, are needed in expressions which allow the absorption and scattering coefficients at other wavelengths, to be extrapolated from those at 400 nm.

These expressions are:

$$b_e(\lambda[nm]) = (\frac{\lambda}{400})^{-\alpha} b_e(400), \tag{4.5}$$

and

$$a(\lambda[nm]) = (\frac{\lambda}{400})^{-\kappa} a_{dust}(400) + A_{IR} e^{-\lambda_o/\lambda}. \tag{4.6}$$

The variable κ is dependent on the dust grain size and composition, and is assumed to be independent of depth. A_{IR} describes the absorption due to molecular absorption that is only seen in the far infrared wavelengths. At smaller wavelengths, absorption is restricted to mostly dust particulates. The final factor is the levels of dust present, a_{dust} which varies with depth. These six factors produce the backbone of the ice models. In all the models tested in this study, only $b_e(400)$ and $a(400)$ vary as a function of depth with the remaining four parameters being the same at all depths. The values for absorption and scattering for each model are found by comparing simulations of artificial light sources with data, as will be discussed in Section 4.5.

4.4 Propagation length

In many situations it is not possible to measure the scattering and absorption properties of a medium separately. Consider the case of detecting beamed light at some distance from an emitter. The fluence will have dropped between the source and detection site but this will be due to both absoprtion of the emitted light and scattering of the light from its initial direction. For this reason a quantity called the propagation length is often used which is a combination of scattering and absorption.

The propagation length is characterized in the equation [10] :

$$N(d \geq 5\lambda_e)) \propto \frac{1}{d} e^{\frac{-d}{\lambda_p}}, \tag{4.7}$$

where N is the number of photons, d is the distance between emitter and detector and λ_p is the propagation length defined as:

$$\lambda_p = \sqrt{\frac{\lambda_a \lambda_e}{3}}. \tag{4.8}$$

The propagation length is a combination of the absorption length (the reciprocal of the absorption coefficient given in Equation 4.1) and the effective scattering length defined in Equation 4.2.

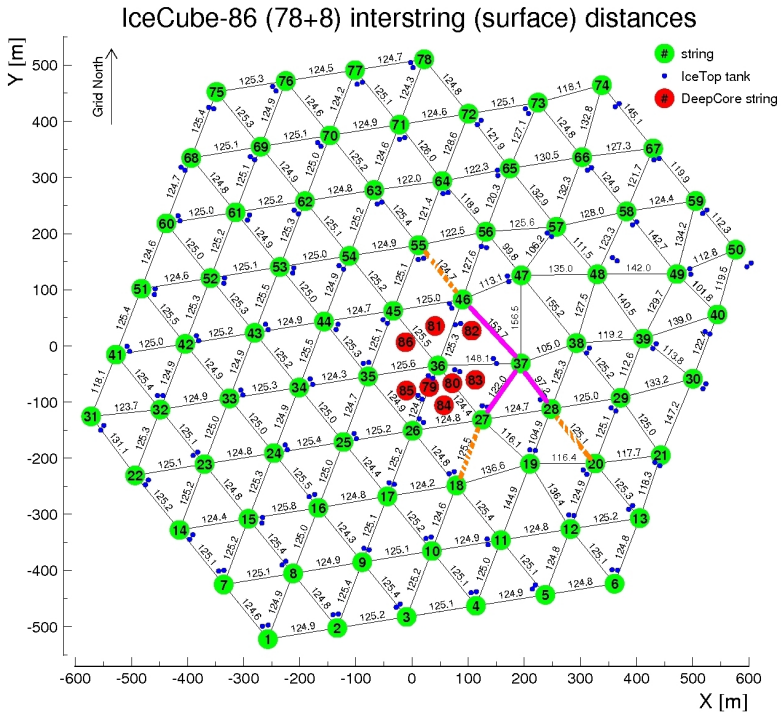

Figure 4.3: Distances between String 37 and surrounding strings. The solid bright pink lines are the first layer of surrounding strings and the stripped orange lines are the second layer of surrounding strings. The number of hits received was studied in relation to the distance from the source.

One can illustrate how the propagation length can be calculated using simulated data. We simulated light emitted from an LED on string 37 because there was a variation in the distance to surrounding strings so we could compare the number of photons received as a function of distance. In this simulation we used an icemodel (Spice 1) which restricts the optical properties to only vary in the vertical direction and not in the $x - y$ plane. Three sample depths with different optical properties were chosen: namely, at the locations of DOM 11, DOM 24 and DOM 44. At each depth six strings surround string 37 were

chosen: three each from the first and second layers out from the light source. See Figure 4.3 for a pictorial representation.

To calculate the propagation length, firstly the reciprocal of the absorption coefficient was found giving the absorption length:

$$(a_c) = \frac{1}{\lambda_a}. \tag{4.9}$$

A similar calculation is done with the effective scattering coefficient but it must first be found by manipulating the geometric scattering coefficient:

$$b_s(1-g) = b_e(\lambda_{be}), \tag{4.10}$$

which gives

$$(\lambda_e) = \frac{1}{\lambda_{be}}. \tag{4.11}$$

The number of photons detected is fitted with the function 4.7 and plotted against depth in Figure 4.4.

Figure 4.4 indicates approximately 800 photons are received 100 m from the source. For the ice model used in these simulations, the absorption length at the depth of DOM 11 is approximately 85 m. If only absorption was important then the ratio of the number of photons received at distance d_2 and d_1 would be given by

$$\frac{N_2}{N_1} = e^{(-(d_2-d_1)/\lambda_a))}, \tag{4.12}$$

and there would be approximately 300 hits. However we can see from Figure 4.4 that actually scattering reduces the number at 180 m to much less than 300. The increased drop off in hit count shows the importance of considering the scattering parameters when calculating the propagation length.

It is also apparent looking at Figure 4.4 the difference in ice properties at different depths in the ice from the difference in slope of the curves. DOM 24 has the greatest slope and the greatest difference between photon count predicted by absorption and that actually detected. DOM 44 differs slightly less than DOM 24 as its scattering coefficient is similarly smaller.

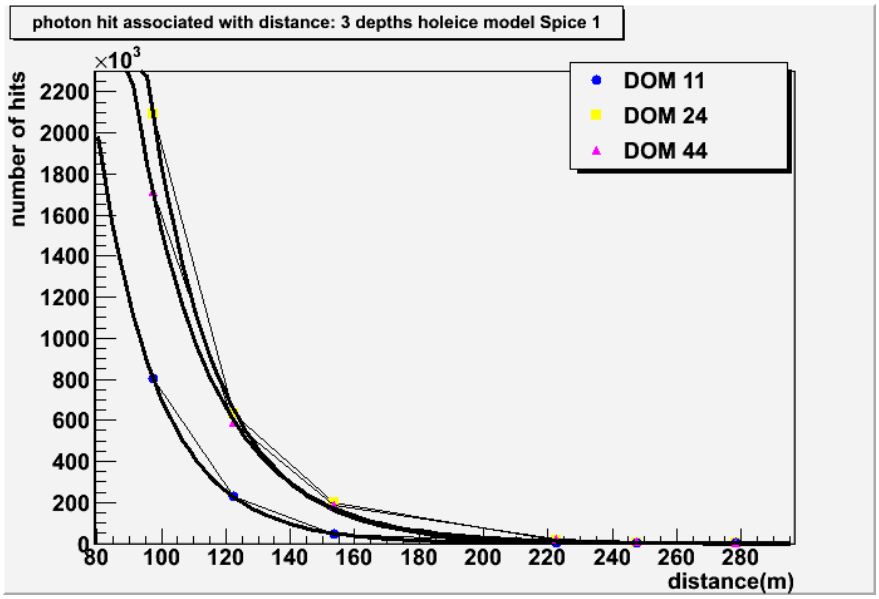

Figure 4.4: Function fitted to distance vs hits at three different depths.

4.5 Ice models

Development of an accurate ice model is an ongoing project within the IceCube collaboration. At the outset of this project, the model used was the Additionally Heterogeneous Absorption model (AHA). Recently, alternative ice models have been developed primarily by IceCube collaboration member Dmitry Chirkin [48]. The new model, South Pole Ice (Spice), has several variations which are labelled with suffixes. The most recent Spice model is Spice Mie. The evolution of ice models is described in the following sections.

4.5.1 AHA

Released in early 2007, the ice model AHA was developed using emitter-receiver pairs at the same depth. Data from in-situ light sources was compared with Monte Carlo simulation results. The simulations were run using absorption and scattering parameters which did not vary with depth [10]. The quantity which was compared between data and simulation was the shape of the photon arrival-time distribution. The model parameters were adjusted until the time distribution matched that of the emitter-receiver pair [10] as determined by a χ^2 statistical test. The parameters which produced a photon arrival distribution which best fitted the data at a given depth were assigned to that depth. The results were tabulated in 10 m intervals.

The scattering function used to simulate the photons was the Henyey-Greenstein function (see Equation 4.4 [10]. The absorption was taken as Equation 4.2 allowing only C_{dust} to vary with depth. It also

considered the 1°K change in temperature with depth [10].

The fact that light which travels between an emitter and a receiver actually passes through ice above and below this depth means that extreme values of absorption and scattering get smeared out. In an attempt to counteract this smearing, a deconvolving procedure was applied which resulted in more extreme values for the scattering and absorption parameters [49].

Another improvement from previous modelling was the ability to model at deeper depths. By extrapolating ice core data, the ice was found to be cleaner than previously thought. A pictorial representation of the absorption and scattering properties is found in Figure 4.5 [10].

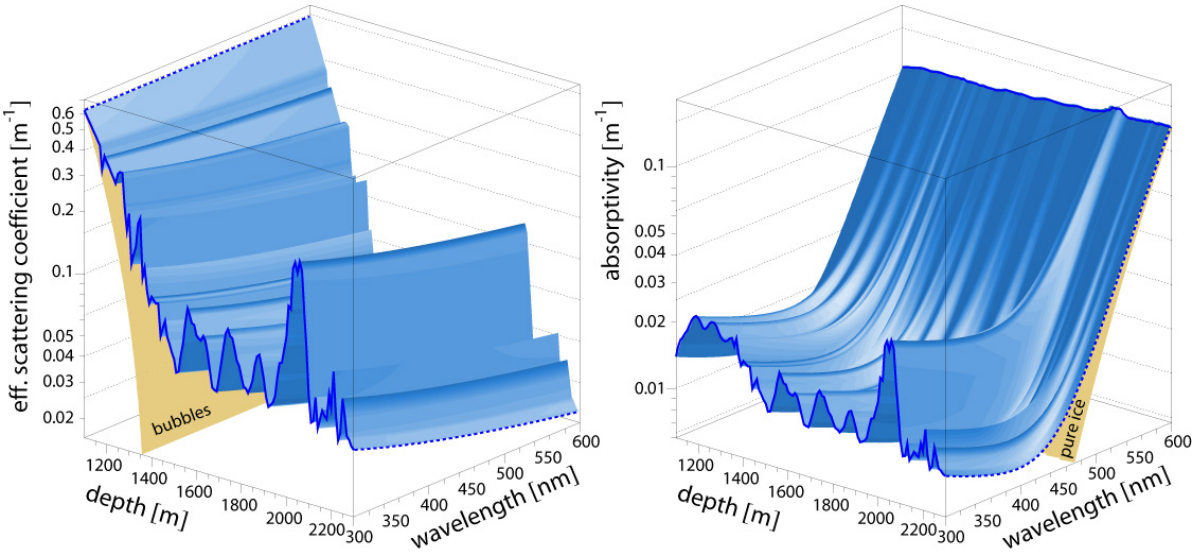

Figure 4.5: Absorption and scattering varying with depth and wavelength.

4.5.2 Spice

The currently accepted standard ice model is the South Pole Ice or Spice created by Dmitry Chirkin in late 2009. The Spice model continues to use the six parameter function first introduced by Ackermann et al. [10]. A main difference from AHA is that the quantity which was compared between simulation and data was the number of photons which arrived, rather than the shape of the light arrival time distribution. Secondly, during simulations the coefficients were allowed to vary for each 10 m increment independently until the best fit was found for the amount of light received at all receivers. An iterative fitting procedure locates the best fit absorption and scattering coefficients at all depths. At a given depth the absorption and scattering coefficients were not coupled. This differs from the development of AHA where the value of the scattering coefficient was coupled to the value of the absorption coefficient.

With more variables to consider, the simulations became computationally expensive. Ice models of the Spice variety would not be possible without the newly developed Photon Propagation Code (PPC)

to simulate the propagation of photons through the ice (see Section 5.2 for complete details). There are several variations of the Spice ice models with varying assuptions or fitting criteria. In this study the original model Spice 1 and the latest model Spice Mie are used.

Spice 1

Spice 1 used the AHA ice model as the first guess in the iterative fitting procedure to find the table of scattering and absorption coefficients. Similar to AHA, Spice 1 uses the Henyey-Greenstein function and tabulated 10 m layer structure [51].

Spice Mie

There are multiple difference between Spice 1 and Spice Mie. The versions after Spice 1 use bulk ice to seed the iterative fitting procedure [52]. In any of the Spice ice models, to shorten simulation time the DOM sizes were scaled up by a factor of five. Scaling the DOMs decreased the photon arrival time by shortening the distance travelled. These effects were not realized and were only fixed in Spice Mie [52].

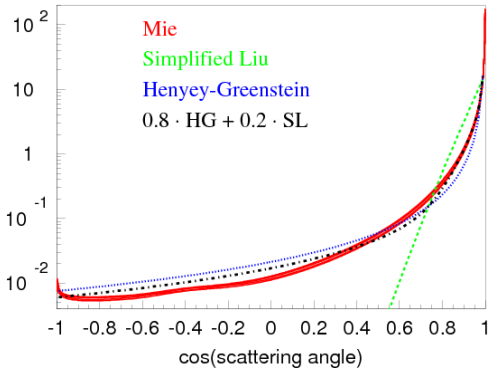

Figure 4.6: Comparisons of scattering angle for different functions.

The main change with Spice Mie is the scattering function; it is now a combination of 55% Henyey-Greenstein and 45% Simplified Liu functions for a total scattering coefficient of $\langle cos\theta \rangle = 0.9$ (see Figure 4.6). This change came about as the value of $\langle cos\theta \rangle$ had been increased. Below values of $\langle cos\theta \rangle = 0.8$ the Mie scattering theory and the Henyey-Greenstein function are generally the same [53]. Above values of $\langle cos\theta \rangle = 0.8$, then the Liu is a better phase function:

$$\text{Liu phase function} = K(1 + \epsilon \cos\langle\theta\rangle)^{n_p}, \tag{4.13}$$

where K is the normalization constant, ϵ is the characteristic factor and n_p is the anisotropic index. Setting $\epsilon = 1$ further simplifies the equation. The Simplified Liu phase function tackles the problem that multiple phase functions can generate the same average $\cos\theta$. This is avoided by including more

variables to consider the peak value as well [53]. It has been shown that at higher values of $\langle \cos\theta \rangle$, the Simplified Liu phase function is the best approximation with Mie theory [53]. However, in the Spice Mie ice model a combination of the Henyey-Greenstein and Simplified Liu equations were used. In this equation a value of 0.9 was assigned to $\langle \cos\theta \rangle$ [48].

Also, Spice Mie uses the data from the dust logger, an in-situ device that measures the scattering properties on a millimetre scale [16]. Beyond the reach of the dust logger, ice core data was used to extrapolate ice properties. By combining the dust logger and ice core data, an accurate map of the ice properties, including a slight horizontal tilt, was produced and implemented in Spice Mie [48].

Chapter 5

Methodology

5.1 Flasher data

One way to test the quality of an ice model is to compare the distributions of photon arrival times with actual flasher data. The flasher data is taken by flashing a combination of the 12 LEDs attached to each DOM. The number of LEDs and their brightness can be varied. Several settings of the flasher data were not altered in the study. For instance, the set of data used in this study flashed all the DOMs on string 63 individually. This is called Single PhotoElectron (SPE) data. By only flashing one LED, the amount of light emitted was kept to a minimum so that DOM saturation was not an issue. All this data was processed from raw form using the script shown in Appendix A.

The data was taken in October 2009 with the string configuration of IC40. The flasher data runs were taken under the settings of which the details are contained in Appendix D.

A total of 15 different depths were studied, spread at regular intervals through the detector. The first was at DOM 3 and thereafter increased at intervals of four DOMs. There were also some difficulties encountered at the large dust layer located around DOM 35 in the detector. This dust layer absorbed and scattered the light such that flasher data was unobtainable. DOM 34 was chosen instead.

Another advantage of using only one LED was the ability to study LEDs at different orientations. Two orientations were studied, one with the LED facing towards the receiving string and the other with the LED pointed away from the receiving string. With the data used in this study, the DOMs on string 63 were flashed and the photons received on string 70's DOMs were recorded (Figure 5.1). The LED angles are available in Tables C.1 and C.2. The information on each flasher run can also be found in Appendix C.

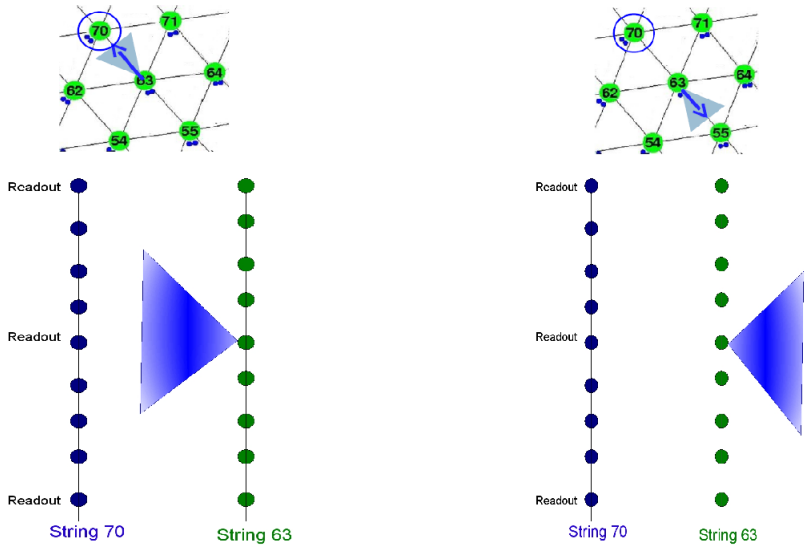

Figure 5.1: Visual representation of the two settings studied: string 63 flashing towards string 70 (left) and string 63 flashing away from string 70 (right).

5.2 Photon propagation code

The recently developed Photon Propagation Code (PPC) was used to simulate the photon transport through ice to obtain the time distributions at the relevant DOMs. PPC is computationally expensive so a Graphics Processing Unit (GPU) was used. A 'real time' simulation of the light propagation is performed till the photons are absorbed or they hit a DOM [54]. The absorption rate is determined by the calculated lifetime of the photons.

Prior to the development of PPC, a photon propagation package called Photonics was used. Photonics is a Monte Carlo simulation software package which creates a series of look up tables [44, 55] which are referred to by the detector simulation packages. PPC, on the other hand, incorporates the detector simulation with individually tracking of the photons. This eliminates some of the known issues associated with the tables such as binning and the resulting parametrization needed.

While PPC is useful in studies such as that undertaken here, it has been only used to a limited extent with simulation of the full IceCube detector. This is due to the length of time associated with tracking all photons individually.

5.3 PPC simulation settings

Simulations were carried out using PPC version 48 with the same settings for each ice model. In PPC there are two descriptions of angular acceptance, 'nominal' and 'holeice'. The holeice setting increases the angular acceptance for the DOMs. This is a way to account for the effect of the increased scattering

that is expected to occur in the refrozen ice in the holes without actually changing the ice properties themselves.

This setting was chosen as it is likely to provide a better representation of the ice surrounding the optical modules. Another setting used was the DOM oversize factor of five. This increases the surface area which in turn decreased the number of received photons needed for enough statistics [51]. The specifics of PPC and details of these settings can be found in Appendix B.2 to Appendix B.4.

Another property to consider is the so-called tilt of the ice. The tilting parameters account for the fact that the dust layers are not horizontal and show some tilt across the detector [48]. The tilting parameters were disabled for both AHA and Spice 1 simulations and enabled for Spice Mie simulations (see Appendix B.6).

The number of photons simulated was kept constant at 1×10^{10} photons. However, after plotting the time distributions, it was found that the number of hits received differed dramatically. The significance of this is discussed in Section Appendix A alongside the data tables.

While it is interesting to note the variation in the number of hits received from the simulations as a function of depth or ice model, it cause a large variation in error bar size. The size of the error bars is dependent on the number of hits received and thus the χ^2 statistic is affected. To ideally compare the χ^2 values at different depths it is desirable to have a similar number of photons received at all depths. The number of photons received follows a linear relationship with the number of photons emitted. The number of photons emitted was changed so the number of photons received would be within a factor of 3 with the emitter facing the receiver and within a factor of 77 when the emitter is pointed away from the receiver. This means that the error bars would be similar.

5.4 Histogram settings

The most appropriate time interval to focus on depends on the position of the receiving source with respect to the emitter. For example, when looking at the receiver which was four DOMs above or below the source the range was between 500 and $2,000$ nanoseconds. This range was a compromise for most ice model plots. In regions of clean ice the majority of photons would arrive before $2,000$ ns. Conversly, in other regions of dirty ice, the time distribution was cut short by the $2,000$ ns limit due to higher scattering properties. While this issue was realized, for the purpose of this study, uniform limits were imposed through all depths. When the receiving source was directly across from the flashing LED, the time limit was restricted at $1,200$ ns as the photons arrived earlier at all depths due to the shorter distances traveled.

All of the plots were normalized to the flasher data and 50 bins were used as it appeared to allow

for an appropriate level of statistics. Finer binning was tried but showed too much statistical variation, whereas a lower binning did not show enough of the shape of the distribution. For the time range between 500 ns and 2,000 ns, the 1,500 ns range with 50 bins, resulting in a bin size of 30 ns. This was adjusted for the limit of 1,200 ns and the bin size was altered to 14 ns so the number of bins could remain at 50.

5.5 Quantitative analysis

The time distributions for the flasher data and simulations were compared quantitatively. A statistical analyses was performed using a Pearson's χ^2 test for the two unweighted histograms:

$$\chi^2 = \sum_{i=1}^{r} \frac{(n_i - N\hat{p}_i)^2}{N\hat{p}_i} + \sum_{i=1}^{r} \frac{(m_i - M\hat{p}_i)^2}{N\hat{p}_i} = \frac{1}{MN} \sum_{i=1}^{r} \frac{(Mn_i - Nm_i)^2}{n_i + m_i}, \tag{5.1}$$

where r is the number of bins. p_i is the probability that a value will be in the ith bin for both distributions. M and N are the summation of the total number of hits per bin over the number of bins for each distribution respectively:

$$N = \sum_{i=1}^{r} n_i \qquad \text{and} \qquad M = \sum_{i=1}^{r} m_i. \tag{5.2}$$

It was also useful to compare the shape characteristics of the time distributions through the skewness and kurtosis values. These were calculated by ROOT when plotting the histograms. If the skewness and kurtosis measurements are both zero, the distribution is a perfect gaussian. The skewness of a histogram is the measure of the asymmetry of the distribution; a perfectly centered plot has a skewness value of zero. If the skewness is negative than more of the data entries are to the right of the mean, if it is positive than more of the data entries are to the left of the mean. The kurtosis is a measure of how the data is distributed about the mean. If the distribution is plateau-like with a broad distribution about the mean it will have a low kurtosis value. Alternatively, if the distribution is peaked around the mean have a high kurtosis value. See Figure 5.2 for further visualization.

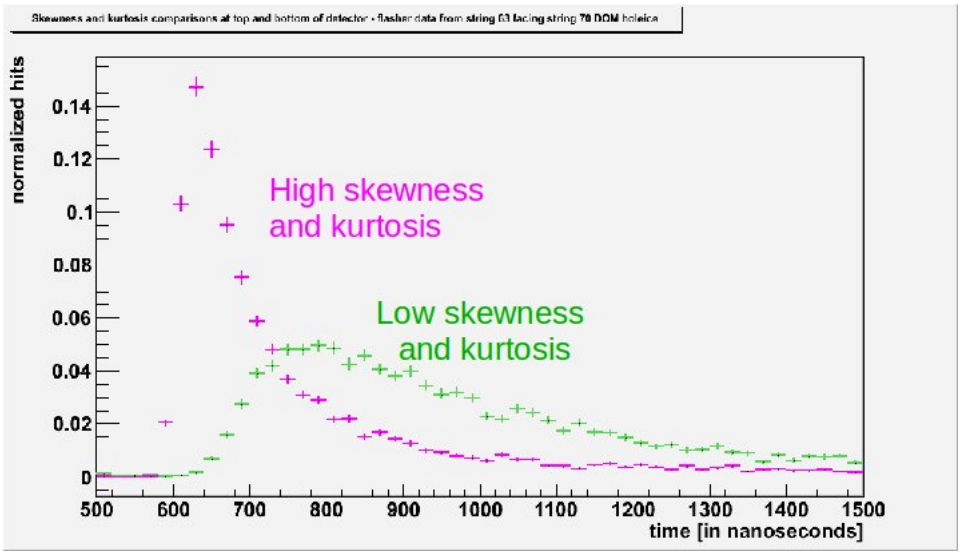

Figure 5.2: Examples of two time distributions with varying levels of skewness and kurtosis.

Chapter 6

Results

This chapter presents the main results comparing the shape of photon arrival time distributions of flasher data and Monte Carlo simulations. The focus for this study was on the emitter-receiver pair directly across from each other. The DOMs above and below the source on the receiving string further supplement the study, by investigating effects when the emitter-receiver pairs were not at the same depth. The particular choice of four above and below was chosen somewhat arbitrarily. Consideration was given to a choice which would give a distance between emitter and receiver which was significantly different from the straight across configuaration and also give a reasonable proportion of photons arriving at the receiving DOM. The results for the LEDs flashing towards the receiver and flashing away from the receiver are presented below. Througout this chapter, and the remaining chapters in this thesis, the names of the ice models used in the simulations, AHA, Spice1 and Spice Mie, will be used to refer to the simulated data produced by the simulations in which they were used.

6.1 Results for emitters facing receivers

A χ^2 statistical analysis was performed on the time distributions to judge quantitatively which simulation fitted best with that of the flasher data. It was noticed that the shape of Spice Mie's timing distribution seemed to match best under visual inspection. However the χ^2 statistic in many cases had a larger value than for the other time distributions produced using the other two ice models. Other statistical quantities such as the skewness, kurtosis and mean confirmed that the shape of Spice Mie's time distribution matched the flasher data best. It was also observed that Spice 1 and AHA were closely coupled in their results. The results are all displayed in Table 6.1 to Table 6.6 with the depth, χ^2 values, skewness, kurtosis and mean values. The skewness, kurtosis and mean values for the ice models are presented as percentages of the flasher data. The percentages are calculated by dividing the ice model by the flasher

data value and multiply by 100. The negative sign indicates that the values were of opposite sign than the flasher data.

It was suspected that the reason for the unfavorable χ^2, in some cases, was due to the the distributions being misaligned in their start times. The timing information was read out directly from the flasher-board. Possible sources of error include the expression used to assign the zero-point for the simulated timed distributions or something in the simulation process.

The time distributions were shifted with a time-offset to find out how well they might match if their starting time were allowed to vary. The lowest χ^2 value was recorded in each case. Some of the offsets necessary were up to 100 ns. The uncertainty associated with the IceCube clocks is 3 ns. Sometimes the χ^2 values did not change very much from a 40 ns shift to a 100 ns shift. The shift found in this way will be dependent on the bin sizes used in the histograms to some extent. At the time of writing this thesis the explanation for the offset is not understood. It will be an important issue to understand the origin of these time offsets in the future. An example of a shifted and non-shifted time distribution is given in Figure 6.1. The shifted χ^2 values are presented in Table 6.1 to Table 6.6 and will be discussed throughout this chapter.

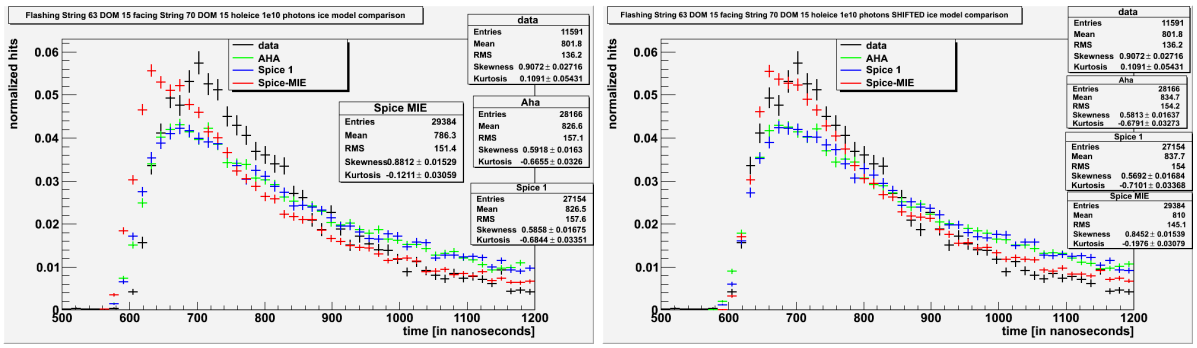

(a) Non-shifted

(b) Shifted

Figure 6.1: (Left) Non-shifted time distribution with timing information read in directly from the flasher board. (Right) Each ice model was shifted individually to produce the lowest χ^2 results. Shifts for each ice model were: AHA = 11 ns, Sp1 = 15 ns, Mie = 29 ns.

Table 6.1: The statistical results for a receiver directly across from the emitter are displayed below: the χ^2, shifted χ^2, as well as skewness, kurtosis and mean values for a non-shifted time distribution. The results for the flasher data are displayed in numerical format as the actual values whereas the icemodels are represented as a percentage of the flasher data. The negative percentage sign for the ice models indicates an opposite sign from the flasher data.

DOM directly across - part 1							
DOM	ice model	χ^2	shifted χ^2	shift	skewness	kurtosis	mean
3	Data				0.68	-0.45	838
	AHA	16	13	-18	40 %	212 %	106 %
	Spice 1	12	11	-10	47 %	205 %	105 %
	Spice Mie	5	2	15	82 %	141 %	100 %
7	Data				0.16	-0.91	927
	AHA	6	6	-5	-36 %	107 %	102 %
	Spice 1	12	6	-48	-221 %	85 %	108 %
	Spice Mie	4	3	-22	-64 %	105 %	104 %
11	Data				0.35	-0.75	887
	AHA	15	4	-20	15 %	133 %	104 %
	Spice 1	25	4	-26	-15 %	131 %	107 %
	Spice Mie	7	2	2	65 %	125 %	101 %
15	Data				0.91	0.11	802
	AHA	12	10	11	65 %	-610 %	103 %
	Spice 1	12	10	15	65 %	-627 %	103 %
	Spice Mie	17	3	29	97 %	-111 %	98 %
19	Data				0.54	-0.53	855
	AHA	16	8	-66	-5 %	191 %	110 %
	Spice 1	12	7	-41	24 %	187 %	107 %
	Spice Mie	3	3	8	87 %	144 %	101 %
23	Data				0.92	0.03	803
	AHA	22	21	-7	52 %	-2968 %	106 %
	Spice 1	23	23	-7	48 %	-3192 %	106 %
	Spice Mie	21	3	24	89 %	-958 %	99 %
27	Data				0.72	-0.50	824
	AHA	17	11	-34	46 %	182 %	107 %
	Spice 1	6	6	5	68 %	154 %	102 %
	Spice Mie	12	2	24	108 %	64 %	97 %
31	Data				0.43	-0.78	872
	AHA	7	6	-8	47 %	126 %	103 %
	Spice 1	19	10	-52	-11 %	128 %	109 %
	Spice Mie	4	3	-14	57 %	120 %	103 %

Table 6.2: The statistical results for a receiver directly across from the emitter are displayed below: the χ^2, shifted χ^2, as well as skewness, kurtosis and mean values for a non-shifted time distribution. The results for the flasher data are displayed in numerical format as the actual values whereas the icemodels are represented as a percentage of the flasher data. The negative percentage sign for the ice models indicates an opposite sign from the flasher data.

DOM directly across - part 2							
DOM	ice model	χ^2	shifted χ^2	shift	skewness	kurtosis	mean
34	Data				0.31	-0.78	905
	AHA	27	13	-95	-117 %	98 %	111 %
	Spice 1	4	2	-97	-202 %	61 %	115 %
	Spice Mie	3	2	-64	-82 %	119 %	111 %
39	Data				1.22	0.84	766
	AHA	22	22	5	52 %	-71 %	107 %
	Spice 1	31	26	-21	39 %	-97 %	110 %
	Spice Mie	23	1	28	95 %	74 %	98 %
43	Data				0.76	-0.3	822
	AHA	13	11	-14	45 %	305 %	106 %
	Spice 1	12	11	-9	45 %	303 %	106 %
	Spice Mie	7	2	19	90 %	149 %	99 %
47	Data				1.37	1.36	749
	AHA	43	39	-11	49 %	-40 %	109 %
	Spice 1	19	17	7	70 %	3 %	104 %
	Spice Mie	28	3	20	93 %	72 %	99 %
51	Data				1.64	2.33	723
	AHA	33	30	-13	45 %	-17 %	111 %
	Spice 1	23	6	18	84 %	50 %	101 %
	Spice Mie	39	2	24	102 %	101 %	97 %
55	Data				1.0	0.29	785
	AHA	10	3	16	89 %	-45 %	100 %
	Spice 1	14	10	-14	58 %	-230 %	106 %
	Spice Mie	3	2	4	87 %	-30 %	101 %
59	Data				1.69	2.54	719
	AHA	54	40	-32	41 %	-20 %	114 %
	Spice 1	24	6	16	83 %	50 %	101 %
	Spice Mie	40	2	21	100 %	96 %	97 %

Table 6.3: The statistical results for a receiver above from the emitter are displayed below: the χ^2, shifted χ^2, as well as skewness, kurtosis and mean values for a non-shifted time distribution. The results for the flasher data are displayed in numerical format as the actual values where as the icemodels are represented as a percentage of the flasher data. The negative percentage sign for the ice models indicates an opposite sign from the flasher data.

4 DOMs above - part 1							
DOM	ice model	χ^2	shifted χ^2	shift	skewness	kurtosis	mean
3			Not applicable				
7	Data				1.06	.66	1108
	AHA	29	28	-5	65 %	-54 %	107 %
	Spice 1	31	21	-35	62 %	-50 %	110 %
	Spice Mie	4	2	-13	91 %	56 %	100 %
11	Data				.77	.29	1151
	AHA	13	6	-99	62 %	-216 %	112 %
	Spice 1	9	3	-116	55 %	-226 %	113 %
	Spice Mie	4	2	-39	112 %	77 %	101 %
15	Data				1.14	.65	1089
	AHA	4	3	-34	73 %	-3 %	106 %
	Spice 1	3	3	-17	73 %	-4 %	104 %
	Spice Mie	4	2	24	108 %	183 %	96 %
19	Data				.85	.11	1141
	AHA	4	3	-36	71 %	-491 %	108 %
	Spice 1	7	4	-39	67 %	-529 %	110 %
	Spice Mie	2	2	15	104 %	157 %	99 %
23	Data				1.28	1.17	1058
	AHA	15	9	-34	61 %	-13 %	112 %
	Spice 1	10	9	-18	65 %	-5 %	108 %
	Spice Mie	4	1	22	95 %	87 %	98 %
27	Data				.66	-.50	1179
	AHA	4	3	-32	103 %	77 %	102 %
	Spice 1	5	4	-26	98 %	88 %	103 %
	Spice Mie	7	6	23	149 %	-57 %	94 %
31	Data				1.24	1.12	1054
	AHA	13	11	-16	65 %	-11 %	108 %
	Spice 1	9	9	-1	69 %	-6 %	107 %
	Spice Mie	8	1	23	97 %	87 %	99 %

Table 6.4: The statistical results for a receiver above the emitter are displayed below: the χ^2, shifted χ^2, as well as skewness, kurtosis and mean values for a non-shifted time distribution. The results for the flasher data are displayed in numerical format as the actual values whereas the icemodels are represented as a percentage of the flasher data. The negative percentage sign for the ice models indicates an opposite sign from the flasher data.

4 DOMs above - part 2							
DOM	ice model	χ^2	shifted χ^2	shift	skewness	kurtosis	mean
34			dust layer				
39			dust layer				
43	Data				1.42	1.67	1009
	AHA	18	15	-31	61 %	-2 %	111 %
	Spice 1	12	11	-12	69 %	15 %	109 %
	Spice Mie	5	2	19	95 %	86 %	99 %
47	Data				1.30	1.09	1034
	AHA	13	7	-58	64 %	-1 %	112 %
	Spice 1	10	5	-45	71 %	8 %	109 %
	Spice Mie	3	3	-1	102 %	122 %	100 %
51	Data				1.87	3.33	933
	AHA	17	16	-13	64 %	24 %	112 %
	Spice 1	8	7	7	77 %	46 %	105 %
	Spice Mie	8	2	18	96 %	93 %	99 %
55	Data				1.33	1.24	1027
	AHA	9	8	-37	70 %	6 %	110 %
	Spice 1	6	6	-17	73 %	14 %	108 %
	Spice Mie	2	2	14	94 %	80 %	100 %
59	Data				1.70	2.66	963
	AHA	6	5	-6	72 %	31 %	107 %
	Spice 1	4	4	-10	78 %	43 %	105 %
	Spice Mie	7	2	12	99 %	100 %	98 %

Table 6.5: The statistical results for a receiver below from the emitter are displayed below: the χ^2, shifted χ^2, as well as skewness, kurtosis and mean values for a non-shifted time distribution. The results for the flasher data are displayed in numerical format as the actual values whereas the icemodels are represented as a percentage of the flasher data. The negative percentage sign for the ice models indicates an opposite sign from the flasher data.

4 DOMs below - part 1							
DOM	ice model	χ^2	shifted χ^2	shift	skewness	kurtosis	mean
3	Data				0.89	0.22	1122
	AHA	5	4	-43	79 %	-132 %	105 %
	Spice 1	5	2	-52	75 %	-145 %	107 %
	Spice Mie	3	3	1	118 %	298 %	97 %
7	Data				0.85	0.21	1162
	AHA	31	16	-102	41 %	-363 %	113 %
	Spice 1	23	10	-109	38 %	-347 %	115 %
	Spice Mie	2	2	-11	89 %	-20 %	102 %
11	Data				1.01	0.42	1100
	AHA	9	6	-42	60 %	-110 %	110 %
	Spice 1	6	4	-32	70 %	-89 %	107 %
	Spice Mie	3	2	8	98 %	80 %	99 %
15	Data				0.48	-0.45	1187
	AHA	6	4	-74	123 %	97 %	103 %
	Spice 1	7	3	-79	105 %	137 %	106 %
	Spice Mie	5	5	-25	165 %	18 %	97 %
19	Data				1.05	0.53	1081
	AHA	13	7	-75	59 %	-74 %	112 %
	Spice 1	7	5	-34	68 %	-59 %	108 %
	Spice Mie	2	1	16	98 %	94 %	99 %
23	Data				0.79	-0.07	1134
	AHA	8	3	-62	78 %	712 %	107 %
	Spice 1	9	4	-61	66 %	974 %	109 %
	Spice Mie	4	3	-27	102 %	178 %	102 %
27	Data				1.02	0.53	1079
	AHA	4	3	-31	77 %	-32 %	106 %
	Spice 1	2	2	-9	90 %	38 %	103 %
	Spice Mie	4	3	9	113 %	179 %	96 %
31	dust layer						

Table 6.6: The statistical results for a receiver directly across from the emitter are displayed below: the χ^2, shifted χ^2, as well as skewness, kurtosis and mean values for a non-shifted time distribution. The results for the flasher data are displayed in numerical as the actual values format whereas the icemodels are represented as a percentage of the flasher data. The negative percentage sign for the ice models indicates an opposite sign from the flasher data.

4 DOMs below - part 2							
DOM	ice model	χ^2	shifted χ^2	shift	skewness	kurtosis	mean
34			dust layer				
39	Data				1.21	0.97	1035
	AHA	6	5	-27	66 %	-19 %	110 %
	Spice 1	4	3	-18	75 %	12 %	107 %
	Spice Mie	2	2	8	99 %	96 %	99 %
43	Data				1.09	0.30	1098
	AHA	8	4	-53	61 %	-163 %	109 %
	Spice 1	6	4	-47	65 %	-158 %	108 %
	Spice Mie	3	2	13	100 %	101 %	99 %
47	Data				1.32	1.07	992.6
	AHA	17	9	-37	72 %	11 %	110 %
	Spice 1	6	6	-3	77 %	19 %	106 %
	Spice Mie	3	2	12	94 %	77 %	100 %
51	Data				1.01	0.09	1073
	AHA	8	5	-48	68 %	-439 %	110 %
	Spice 1	5	4	-48	91 %	116 %	104 %
	Spice Mie	4	4	6	117 %	918 %	97 %
55	Data				1.31	0.99	1005
	AHA	11	10	-9	76 %	20 %	106 %
	Spice 1	10	9.87305	-4	72 %	2 %	107 %
	Spice Mie	5	3	14	92 %	71 %	100 %
59		not	applicable				

6.2 Results for emitters pointed away from receivers

The same analysis for an emitter pointed away from a receiver was performed. The DOMs receiving were again directly across, four DOMs above and four DOMs below the source. The results are presented in Tables 6.7 to Table 6.12. In a similar fashion to the emitters facing the receivers, the tables have the depth, ice model, χ^2 values, shifted χ^2 values, skewness, kurtosis and mean values. The shifted χ^2 values were found in the same manner with the emitter facing the receiver. The skewness, kurtosis and mean values for the ice models are taken as percentages of the flasher data. The percentages were calculated by dividing the ice model by the flasher data value and multiplying by 100. The negative sign indicates that the values were of opposite sign than the flasher data.

Table 6.7: The statistical results of an emitter pointed away from a receiver directly across: the χ^2, shifted χ^2, as well as skewness, kurtosis and mean values for a non-shifted time distribution. The results for the flasher data are displayed in numerical format as the actual values whereas the icemodels are represented as a percentage of the flasher data. The negative percentage sign for the ice models indicates an opposite sign from the flasher data.

away from DOM across - part 1							
DOM	ice model	χ^2	shifted χ^2	shift	skewness	kurtosis	mean
3	Data				0.68	-0.19	1154
	AHA	27	16	-58	47%	419%	111%
	Sp1	17	10	-54	60%	354%	108%
	Mie	6	2	-33	84%	211%	104%
7	Data				0.53	-0.39	1238
	AHA	11	9	-33	50%	201%	106%
	Sp1	12	4	-99	22%	217%	113%
	Mie	3	1	-61	74%	143%	105%
11	Data				0.54	-0.43	1226
	AHA	15	11	-42	46%	199%	107%
	Sp1	22	11	-79	34%	197%	110%
	Mie	5	3	-44	76%	158%	105%
15	Data				0.58	-0.42	1182
	AHA	11	10	-10	64%	181%	104%
	Sp1	12	11	-10	60%	187%	105%
	Mie	6	5	-14	74%	157%	104%
19	Data				0.56	-0.45	1201
	AHA	18	6	-94	42%	182%	110%
	Sp1	17	8	-73	45%	183%	109%
	Mie	7	2	-46	75%	147%	105%
23	Data				0.56	-0.51	1169
	AHA	11	7	-37	67%	145%	106%
	Sp1	13	9	-40	64%	155%	106%
	Mie	5	3	-22	86%	121%	103%
27	Data				0.52	-0.52	1208
	AHA	10	5	-36	61%	154%	106%
	Sp1	5	5	-10	69%	147%	103%
	Mie	3	2	-14	83%	125%	102%
31	Data				0.52	-0.51	1231
	AHA	10	9	-18	54%	164%	105%
	Sp1	15	6	-58	50%	159%	107%
	Mie	4	1	-35	82%	125%	103%

Table 6.8: The statistical results of an emitter pointed away from a receiver directly across: the χ^2, shifted χ^2, as well as skewness, kurtosis and mean values for a non-shifted time distribution. The results for the flasher data are displayed in numerical format as the actual values whereas the icemodels are represented as a percentage of the flasher data. The negative percentage sign for the ice models indicates an opposite sign from the flasher data.

away from DOM across - part 2							
DOM	ice model	χ^2	shifted χ^2	shift	skewness	kurtosis	mean
34	Data				0.82	0.26	1148
	AHA	19	13	-60	11%	-324%	123%
	Sp1	4	3	-42	-20%	-322%	125%
	Mie	1	1	-26	-15%	-361%	116%
39	Data				0.52	-0.53	1177
	AHA	11	9	-26	54%	157%	107%
	Sp1	11	6	-49	66%	142%	106%
	Mie	5	3	-25	77%	125%	104%
43	Data				0.65	-0.39	1166
	AHA	18	12	-51	52%	209%	108%
	Sp1	20	13	-51	49%	216%	108%
	Mie	12	6	-43	68%	174%	106%
47	Data				0.41	-0.75	1209
	AHA	9	5	-53	74%	114%	104%
	Sp1	5	5	-6	78%	119%	103%
	Mie	7	5	-37	77%	116%	104%
51	Data				0.41	-0.8	1198
	AHA	6	2	-45	74%	106%	104%
	Sp1	2	2	7	89%	107%	101%
	Mie	2	2	-12	83%	106%	102%
55	Data				0.49	-0.63	1205
	AHA	6	6	4	68%	133%	103%
	Sp1	5	5	-16	72%	135%	104%
	Mie	6	3	-28	80%	122%	104%
59	Data				0.44	-0.8	1185
	AHA	19	6	-56	72%	109%	105%
	Sp1	5	5	-10	82%	108%	102%
	Mie	10	6	-31	67%	112%	105%

Table 6.9: The statistical results of an emitter pointed away from a receiver four DOMs above the source: the χ^2, shifted χ^2, as well as skewness, kurtosis and mean values for a non-shifted time distribution. The results for the flasher data are displayed in numerical format as the actual values whereas the icemodels are represented as a percentage of the flasher data. The negative percentage sign for the ice models indicates an opposite sign from the flasher data.

away from 4 DOMs above - part 1							
DOM	ice model	χ^2	shifted χ^2	shift	skewness	kurtosis	mean
3		not	applicable				
7	Data				0.76	-0.03	1219
	AHA	42	41	-15	41%	2466%	108 %
	Sp1	23	20	-26	44%	2282%	108 %
	Mie	2	2	2	82%	1231%	102%
11	Data				0.28	-0.55	1309
	AHA	6	3	-98	5%	161%	110%
	Sp1	3	2	-86	3%	159%	110%
	Mie	2	1	-96	89%	145%	107%
15	Data				0.24	-0.69	1327
	AHA	5	3	-52	48%	131%	105%
	Sp1	4	3	-22	62%	131%	103%
	Mie	2	2	-13	115%	113%	101%
19	Data				0.35	-0.66	1321
	AHA	5	3	-36	48%	134%	105%
	Sp1	10	5	-93	9%	140%	108%
	Mie	4	2	-34	75%	123%	103%
23	Data				0.4	-0.69	1291
	AHA	9	4	-54	39%	134%	107%
	Sp1	5	3	-33	54%	126%	104%
	Mie	2	1	-24	90%	104%	102%
27	Data				0.14	-0.76	1368
	AHA	2	2	-11	129%	117%	101%
	Sp1	4	3	-31	22%	121%	104%
	Mie	2	2	-26	115%	118%	102%
31	Data				0.67	-0.25	1228
	AHA	35	32	-24	44%	337%	107%
	Sp1	17	14	17	70%	268%	102%
	Mie	3	2	9	94%	153%	100%

Table 6.10: The statistical results of an emitter pointed away from a receiver four DOMs above from the source: the χ^2, shifted χ^2, as well as skewness, kurtosis and mean values for a non-shifted time distribution. The results for the flasher data are displayed in numerical format as the actual values whereas the icemodels are represented as a percentage of the flasher data. The negative percentage sign for the ice models indicates an opposite sign from the flasher data.

away from 4 DOMs above - part 2							
DOM	ice model	χ^2	shifted χ^2	shift	skewness	kurtosis	mean
34			dust layer				
39			dust layer				
43	Data				0.57	-0.47	1241
	AHA	12	11	-23	53%	182%	106%
	Sp1	8.	8	-4	62%	170%	104%
	Mie	3	3	-18	83%	130%	102%
47	Data				0.18	-0.79	1334
	AHA	6	3	-75	46%	122%	105%
	Sp1	4	2	-75	23%	121%	106%
	Mie	5	3	-66	83%	112%	104%
51	Data				0.31	-0.84	1283
	AHA	3	2	-18	98%	103%	102%
	Sp1	4	3	-3	74%	109%	102%
	Mie	4	3	-26	78%	106%	103%
55	Data				0.36	-0.77	1300
	AHA	12	6	-60	16%	124%	108%
	Sp1	3	3	1	74%	116%	102%
	Mie	3	3	-10	118%	97%	100%
59	Data				0.3	-0.9	1291
	AHA	5	5	10	112%	95%	99%
	Sp1	6	5	-17	56%	107%	103%
	Mie	7	4	-44	60%	106%	104%

Table 6.11: The statistical results of an emitter pointed away from a receiver four DOMs below the source: the χ^2, shifted χ^2, as well as skewness, kurtosis and mean values for a non-shifted time distribution. The results for the flasher data are displayed in numerical format as the actual values whereas the icemodels are represented as a percentage of the flasher data. The negative percentage sign for the ice models indicates an opposite sign from the flasher data.

away from 4 DOMs below - part 1							
DOM	ice model	χ^2	shifted χ^2	shift	skewness	kurtosis	mean
3	Data				0.28	-0.49	1297
	AHA	4	3	-49	68%	179%	105%
	Sp1	4	2	-98	45%	173%	107%
	Mie	2	2	-68	111%	146%	103%
7	Data				0.45	-0.5	1304
	AHA	12	6	-91	8%	180%	110%
	Sp1	6	4	-84	16%	182%	110%
	Mie	1	1	-2	95%	160%	102%
11	Data				0.6	-0.39	1249
	AHA	2	22	-53	34%	221%	108%
	Sp1	17	16	-13	55%	204%	105%
	Mie	2	2	1	92%	127%	101%
15	Data				-0.09	-0.6	1379
	AHA	3	2	-109	-9%	150%	105%
	Sp1	3	2	-120	134%	144%	107%
	Mie	3	1	-72	6%	151%	105%
19	Data				0.47	-0.58	1272
	AHA	11	6	-49	50%	141%	106%
	Sp1	8	7	-29	53%	144%	105%
	Mie	2	2	-8	97%	115%	101%
23	Data				0.09	-0.72	1375
	AHA	3	2	-43	26%	126%	104%
	Sp1	4	3	-61	-10%	131%	105%
	Mie	3	2	-30	149%	129%	102%
27	Data				0.26	-0.77	1329
	AHA	2	2	-3	83%	113%	101%
	Sp1	2	2	9	95%	111%	100%
	Mie	1	1	-1	126%	98%	99%
31			dust layer				

Table 6.12: The statistical results of an emitter pointed away from a receiver four DOMs below the source: the χ^2, shifted χ^2, as well as skewness, kurtosis and mean values for a non-shifted time distribution. The results for the flasher data are displayed in numerical format as the actual values whereas the icemodels are represented as a percentage of the flasher data. The negative percentage sign for the ice models indicates an opposite sign from the flasher data.

away from 4 DOMs below - part 2							
DOM	ice model	χ^2	shifted χ^2	shift	skewness	kurtosis	mean
34			dust layer				
39	Data				0.28	-0.76	1320
	AHA	4	3	-38	47%	121%	104%
	Sp1	3	2	14	91%	114%	100%
	Mie	2	1	-17	99%	102%	101%
43	Data				0.43	-0.66	1296
	AHA	11	9	-52	33%	141%	106%
	Sp1	11	8	-44	36%	140%	106%
	Mie	4	3	-29	73%	125%	103%
47	Data				0.23	-0.85	1324
	AHA	2	1	9	114%	104%	99%
	Sp1	2	1	20	95%	107%	99%
	Mie	2	2	4	126%	97%	99%
51	Data				-0.04	-0.83	1394
	AHA	4	3	-33	-132%	117%	101%
	Sp1	3	2	-48	122%	116%	102%
	Mie	3	2	-45	118%	114%	103%
55	Data				0.41	-0.75	1273
	AHA	10	9	-22	45%	125%	105%
	Sp1	6	6	-5	64%	118%	103%
	Mie	4	3	-22	86%	104%	102%
59		not	applicable				

Chapter 7

Analysis

This chapter presents the numerical results tabulated in Chapter 6 in graph form. The three different receiving settings are discussed. The χ^2 results are the main focus of the analysis followed by a comparison using the skewness, kurtosis and mean values. The results for the emitter facing the receiver and the emitter pointed away from the receiver are presented respectively.

7.1 Emitters facing the receivers

7.1.1 Chi squared

Emitters facing receivers directly across from the source

Figure 7.1 shows the χ^2 comparisons between models as a function of depth in the detector and the effect that allowing the time offset, discussed in section 6.1, has to the χ^2. The values of the time offset are plotted in Figures 7.2 and 7.4. Over all the depths in the detector, Spice Mie shows the greatest change in χ^2 values created by shifting the time distribution. Spice 1 and AHA are only minimally affected by the shift and still retain higher χ^2 values as compared to Spice Mie. Figure 7.1b shows clearly that once shifted, Spice Mie provides a routinely good fit to the ice properties as probed by the flasher data time distributions.

In other words the χ^2 results, with the shifted time distributions, show clearly that the shape of the time distribution, obtained from the Spice Mie simulation, matches best with the flasher data. However the unshifted χ^2 results do not provide compelling evidence supporting any of the ice models.

At the time of writing this thesis the origin or cause of the time off-set is not understood. Broadly speaking there are two possibilities. The first is that there is in fact a problem between the way the data and simulation zero times are set. The second possibility is that the fault lies in the ice model values. If

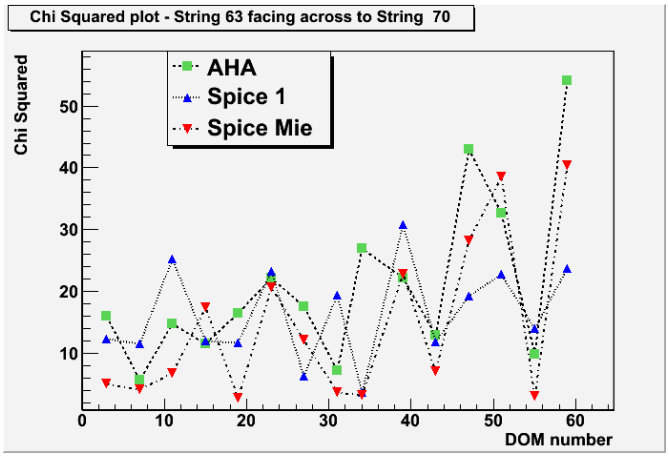

(a) Chi squared across

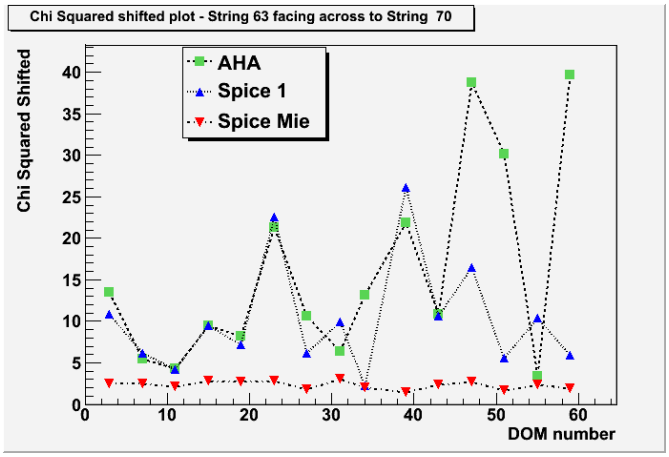

(b) Shifted Chi squared across

Figure 7.1: Chi squared plots as a function of depth for the three different ice models being compared. These plots focus on string 63 flashing facing string 70 receiving on the DOM directly across from the source. Plot a) shows the χ^2 results and plot b) shows the χ^2 results with the time shift.

the first possibility was the solution then we would expect a constant time offset with depth.

Although Figure 7.2 shows the time offset found was not constant with depth for Spice Mie, it must be recalled that this offset was the one which gave the lowest χ^2 rather than the offset which aligned the starting point of the timing distributions. In some cases there was not much variation in χ^2 as the offset was varied. In particular although the offsets found for DOMs $7, 31$ and 34 were negative, the unshifted distributions for these DOMs actually had quite acceptable χ^2 values of $3 - 4$. On the other hand the skewness for the Spice Mie simulated distributions on DOMs 7 and 34 had the opposite sign compared with the data indicating that the shape does not match so well at the depths in any case. It is currently under investigation over whether a constant time off-set would also produce uniformly good χ^2 values for the Spice-Mie simulation-data comparison.

We would also expect that if the first possibility was the solution then the time distributions found

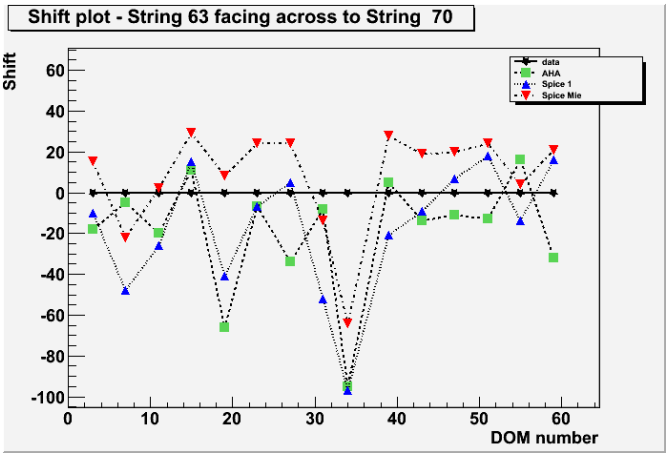

(a) Shift across

Figure 7.2: Time distribution shift values as a function of depth for the three different ice models being compared. These plots focus on string 63 flashing facing string 70 receiving on the DOM directly across from the source.

with simulations using the other two ice models would also show that same offset in the arrival time of the first photons. This is not seen from the time off-sets which gave the best χ^2 values. But it has not been checked whether it would be true if instead the time offset was chosen so as to align the arrival time of the first photons. It is not surprising that different time offsets are required to give the best χ^2 values given that the shape of the time distributions from the simulations using the Spice 1 and AHA ice models are quite different from the data. This mismatch in the shape of the time distributions, is reflected in the mismatch of the skewness and kurtosis values and also in the fact that regardless of whether a time off-set is allowed a good χ^2 value could not be obtained at the majority of depths.

If the second possibility is the case, and the early arrival of photons is due to the value of the coefficients, it is surprising that the shape of the distributions matches so well. The shape of the distribution arises due to the combination of the scattering and absorption. Spice Mie is the model which allows the ratio of the scattering coefficients to the absorption coefficients to vary the most. This can be seen in Figures 4.2 and 4.1 where as a general trend, over all depths, Spice Mie has the smallest scattering coefficient (or longest scattering length) and the largest absorption coefficient (or smallest absorption length). If the scattering length used in the simulations was longer than actually occurs in the ice then this could cause photons to arrive "too early". However if the first photons to arrive had not scattered at all then the arrival time would only depend on the local speed of light.

Emitters facing receivers above and below from the source

The results here look at the time distributions from the DOMs four above and below from the source. The motivation is to look at the light distributed over not only a longer distance but also through different depths of ice with the ice properties varying vertically.

Firstly the results for the receiving DOM located four DOMs above the emitting DOM are considered. The time distribution derived from the Spice Mie ice model has the best χ^2 fit at the majority of depths studied as seen in Figure 7.5. As before, the χ^2 values are plotted over the 15 different depths studied. However, due to the positioning of some DOMs, not all depths were available. Of the 12 depths able to be plotted, there are four exceptions where Spice Mie does not provide the best fit. Spice 1 has the best fit at three depths and there was one depth where AHA's time distribution has the best fit with the flasher data.

Spice Mie improves its fit the most after shifting each ice model individually. Spice Mie's fit has the lowest χ^2 out of the three ice models excluding DOM 27. Even considering the shift, AHA still produces the best fit at DOM 27. The statistical results match what is visually found in the timing distribution plots (see Figure 7.3): Spice Mie's time distribution seems to have reached a higher peak than the flasher data causing AHA to match best at this depth.

At the depth of DOM 27, the flasher data displays a premature peak around 550 ns. This is caused by the light of flashers, located nearby in the detector, also reaching the DOM. The flasher data is obtained by flashing sequentially DOMs. The flashing is supposed to be done with sufficient separation in time that there is no overlap in the light distributions received. That is, all of the light from the previous flash should have arrived before the first photons from the next flash arrive. However, due to time offsets in the DOMs' clocks this is sometimes not the case and the premature peak which can be displayed in Figure 7.3 is the result. The peak can cause the plot to have a distribution with a small tail and large variations as is the case at DOM 27 looking above to DOM 23.

Returning to the time-shift amount (see Figure 7.4), the least change in χ^2 values is seen for all ice models. The trend line remains very similar and only marginally lowered. When receiving on DOMs four above the source, Spice 1's fit is always shifted negatively and AHA's fit is shifted negatively all but once at DOM 51. Spice Mie's fit is nearly always positively shifted.

Thus receiving on four DOMs above further supports the main results with the receiver being directly across from the emitter. That is, Spice Mie's fit matches best at most depths according to the χ^2 test and the results are further supported when the time shift are included. The exception is DOM 27, where the fit of model AHA matches best even with the shifted χ^2 but this may be due to the double flasher event affecting the flasher data.

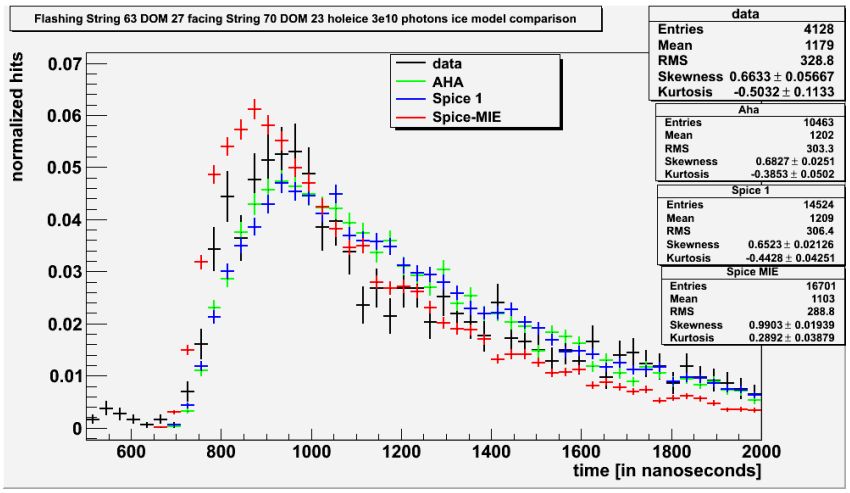

Figure 7.3: Flashing string 63 DOM 27 facing string 70 receiving on DOM 23 comparison between flasher data and the AHA, Spice 1 and Spice Mie ice models simulating 3×10^{10} photons - χ^2 : AHA = 4.0, Sp1 = 4.8, Mie = 7.4. Note the premature peak at approximately 550 ns.

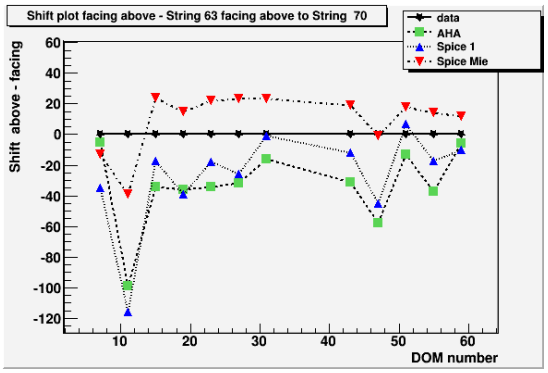

(a) Shift above

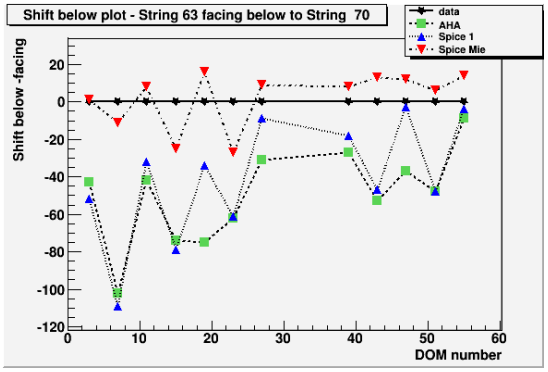

(b) Shift below

Figure 7.4: Time distribution shift values as a function of depth for the three different ice models being compared. These plots focus on string 63 flashing facing string 70 receiving on the DOM directly across from the source.

When receiving on string 70 four DOMs below the source, the χ^2 values indicated that Spice Mie has the lowest results except at DOM 27.

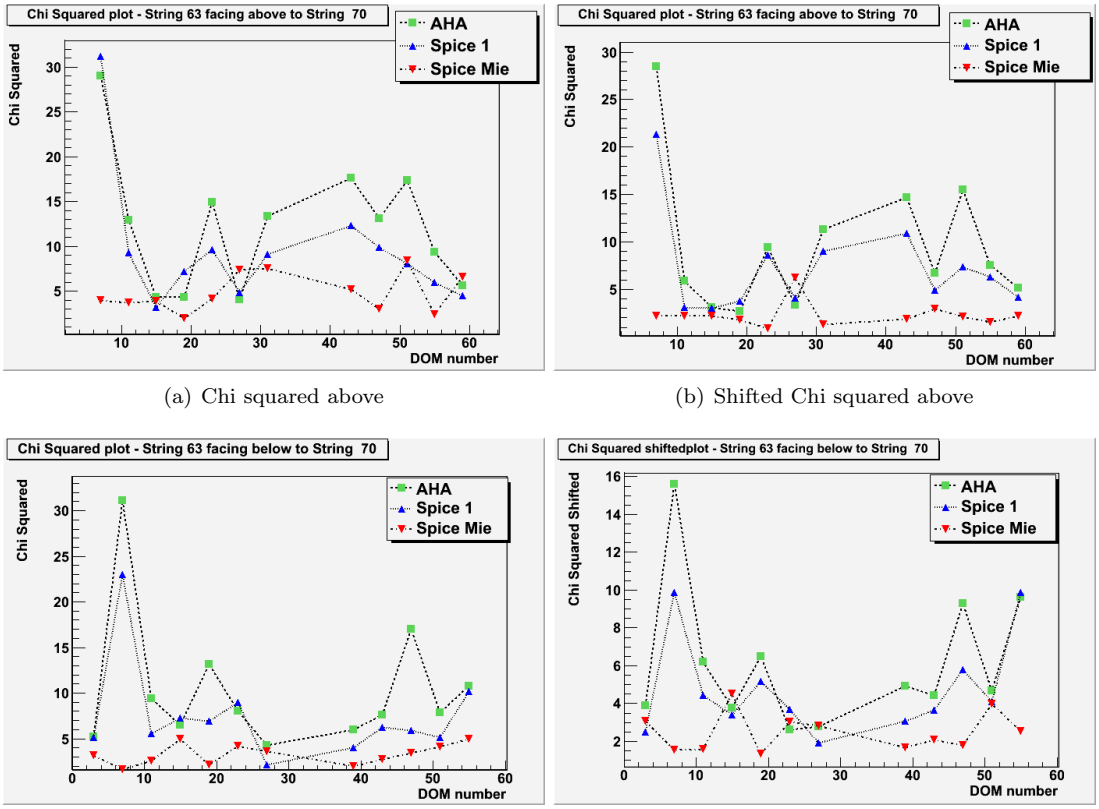

(a) Chi squared above

(b) Shifted Chi squared above

(c) Chi squared below

(d) Shifted Chi squared below

Figure 7.5: Chi squared plots as a function of depth for the three different ice models being compared. These plots focus on string 63 flashing facing string 70 receiving on the DOMs four above(a and b), and four DOMs below(c and d) from the source. Plots a and c show the χ^2 results and plot b and d show the time shifted χ^2 results.

The shifted χ^2 results increase the number of depths where Spice 1's fit matches the flasher data best. AHA also provides the best fit according to the χ^2 results with the time shift included. At that same depth, Spice Mie and Spice 1's fit follows closely behind by only a χ^2 value of one.

Figure 7.4b shows the values of the shifts when receiving below from the emitter. Except for the depth at DOM 55, the largest shift was always attributed to Spice 1 or AHA, all of which were in the negative direction. Spice Mie alternated between a negative and a positive shift but towards the bottom of the detector was steadily shifting in the positive direction. When the receiver is below the emitter (see Figure 7.5 c and d), the decrease in χ^2 was most noticeable for Spice 1 and AHA whose values decreased on average by 50%. Spice Mie continued to decrease in χ^2 values as well. Even though Spice 1 and AHA improved the most with the receiver below the emitter, Spice Mie χ^2 values still remained lower. The relationship between Spice 1 and AHA was maintained particularly well at greater depths in the detector.

7.1.2 Summary of data-simulation comparisons

The remaining sections of this chapter discuss the trends in statistical analysis as a function of depth and ice model. All of the information contained in Tables 6.1 to Table 6.6 can be summarized in graphical form which highlight the trends with depth and similarity of models.

Skewness

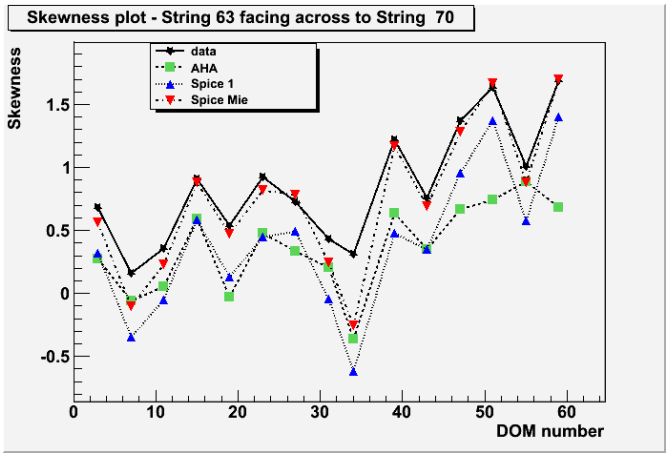

(a) skewness across

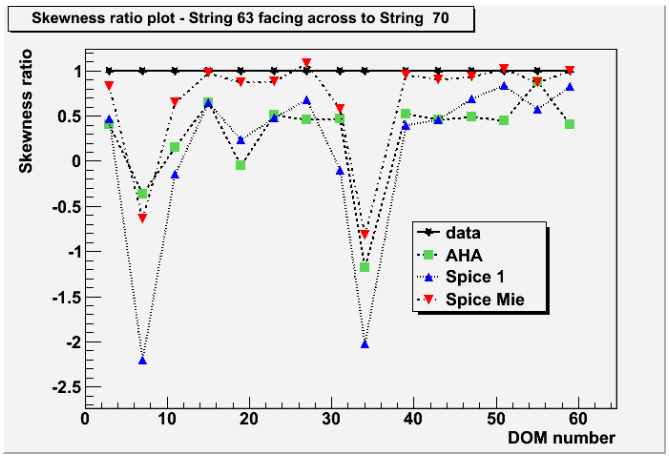

(b) skewness across ratio

Figure 7.6: Skewness plots for string 63 flashing facing string 70 receiving on the DOM directly across from the source. Plot a shows the skewness as a function of depth with an upward trends as depth increases. Plot b shows the same results but as a ratio of the flasher data. A strong coupling between Spice 1 with AHA and Spice Mie with the flasher data are noticable. DOM 34 lies in a region known to be heavily laden with dust particulates causing the sharp rise in skewness.

The skewness results display a general upward trend when looking at the DOM directly across, four above and four below from the source and are plotted in Figure 7.6 to Figure 7.7. Skewness measures the distribution of values about the mean, so if it is increasing, this means the distribution is shifting

further away from a perfect Gaussian distribution. The greatest increase in skewness values with depth is for the DOM receiving four above from the source.

There is a dip in this rise around DOM 34 for directly across. It is also noticeable at this depth that the simulations and data do not match well in the skewness values. In this region, the DOMs receiving above or below the light source receive an insignificant number of photons if any at all. Thus it can be understood why the value of the skewness should drop - the high absorption is cutting off the time distribution. The fact that the simulated time distributions do not match well here with data suggests that the absorption and scattering coefficients are still not modelled well in this region.

The skewness plots show clearly the relationship between Spice 1's time distribution and AHA's time distribution and the relationship between Spice Mie time distribution and the flasher data time distribution. The similarity between the time distributions from Spice 1 and AHA is weaker for DOM 51 and DOM 59 receiving directly across from the source. Here Spice 1's skewness values become closer

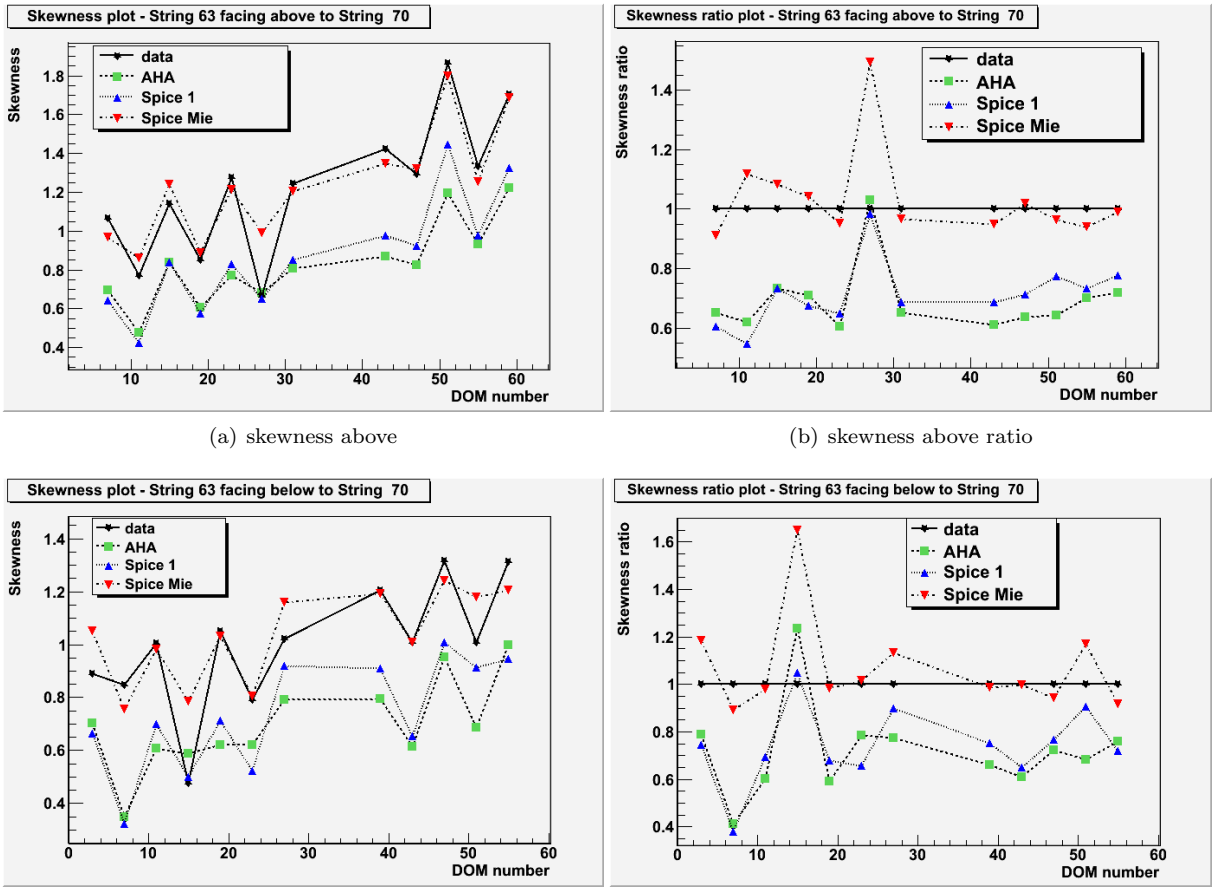

(a) skewness above

(b) skewness above ratio

(c) skewness below

(d) skewness below ratio

Figure 7.7: Skewness plots for string 63 flashing facing string 70 receiving on DOMs four above(a and b) and four below (c and d) the source. Plots a and c show the skewness as a function of depth with an upward trends as depth increases. Plots b and d show the same results but as a ratio of the flasher data.

to the values of the Spice Mie distributions. When the receiver is a distance of four DOMs from the source, the divide between AHA's and Spice 1's distribution shape with that from Spice Mie's and the flasher data is really brought out.

If we look at Figures 4.1 and 4.2 which show the scattering and absorption coefficients for all three models we see for depths less than 2,000 m, the scattering coefficients of AHA and Spice 1 are rather similar. At depths larger than 2,000 m Spice 1 and Spice Mie are more similar. For the absorption coefficients, on the other hand, it is harder to make any such general comments. The regions where the skewness values match between various models seems to correspond to where these model have similar scattering coefficients indicating that the scattering has the most effect on the skewness. It would certainly be expected that the greater the scattering the more pronounced the tail of the distribution would become.

While the general trend of the skewness values with depth are similar, the values for the Spice 1 and AHA derived distributions are significantly lower than values for the distributions derived from Spice Mie. At DOM 27 receiving below and DOM 15 receiving above the skewness values from the Spice 1 and AHA derived distributions match the best with data. These are, however, only isolated cases in the main trend that Spice Mie has the skewness values which are closest to those of the data distributions.

Kurtosis

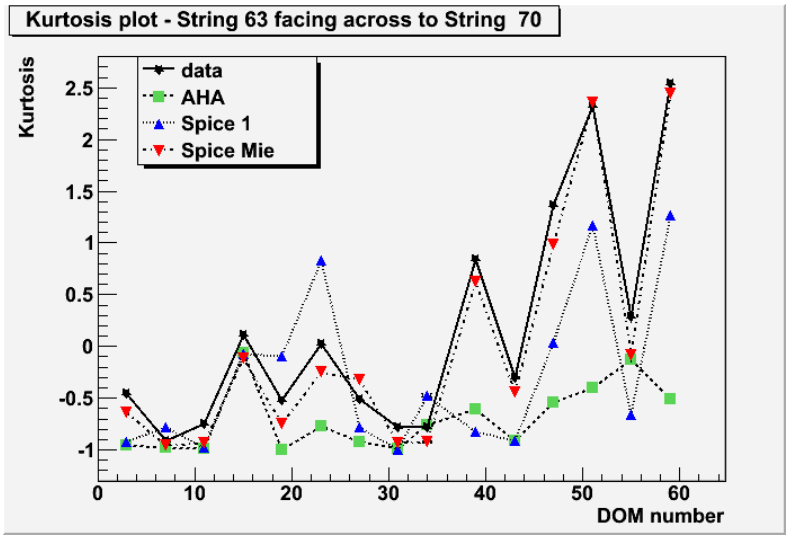

(a) kurtosis across

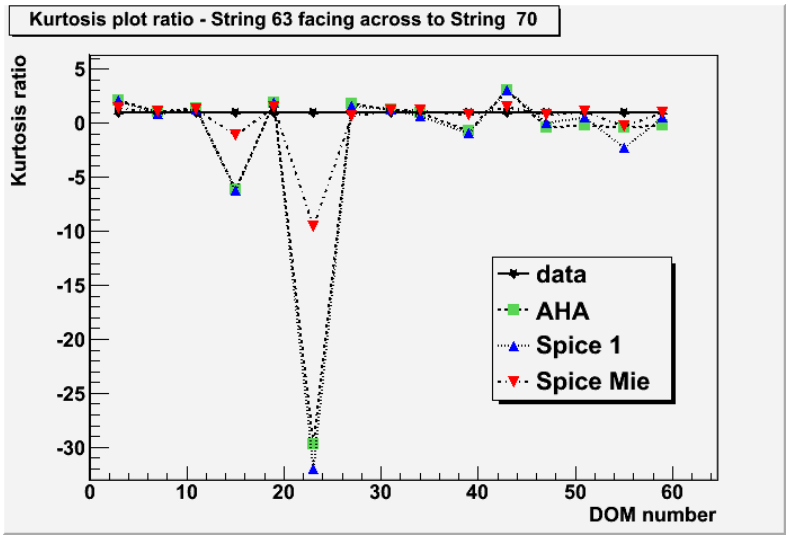

(b) kurtosis across ratio

Figure 7.8: Kurtosis plots for string 63 flashing facing string 70 receiving on the DOM directly across from the source. Plot a shows kurtosis as a function of depth with an upward trends as depth increases. Plot b shows the same results but as a ratio of the flasher data.

The kurtosis values are plotted in Figures 7.8 and 7.9. In a similar way as the skewness did, the kurtosis values have an upward trend. This shows that with increasing depth the arrival of the photons has a narrower distribution about the mean. The ice has less scattering as the depth increases resulting in the sharper peak in the arrival times. The downward spike that was seen, in the skewness values, around DOM 34, is not present in the kurtosis values. Instead a spike around DOM 23 is seen. This is most noticeable with the receiver directly across from the emitter. Here the ratio between the simulation

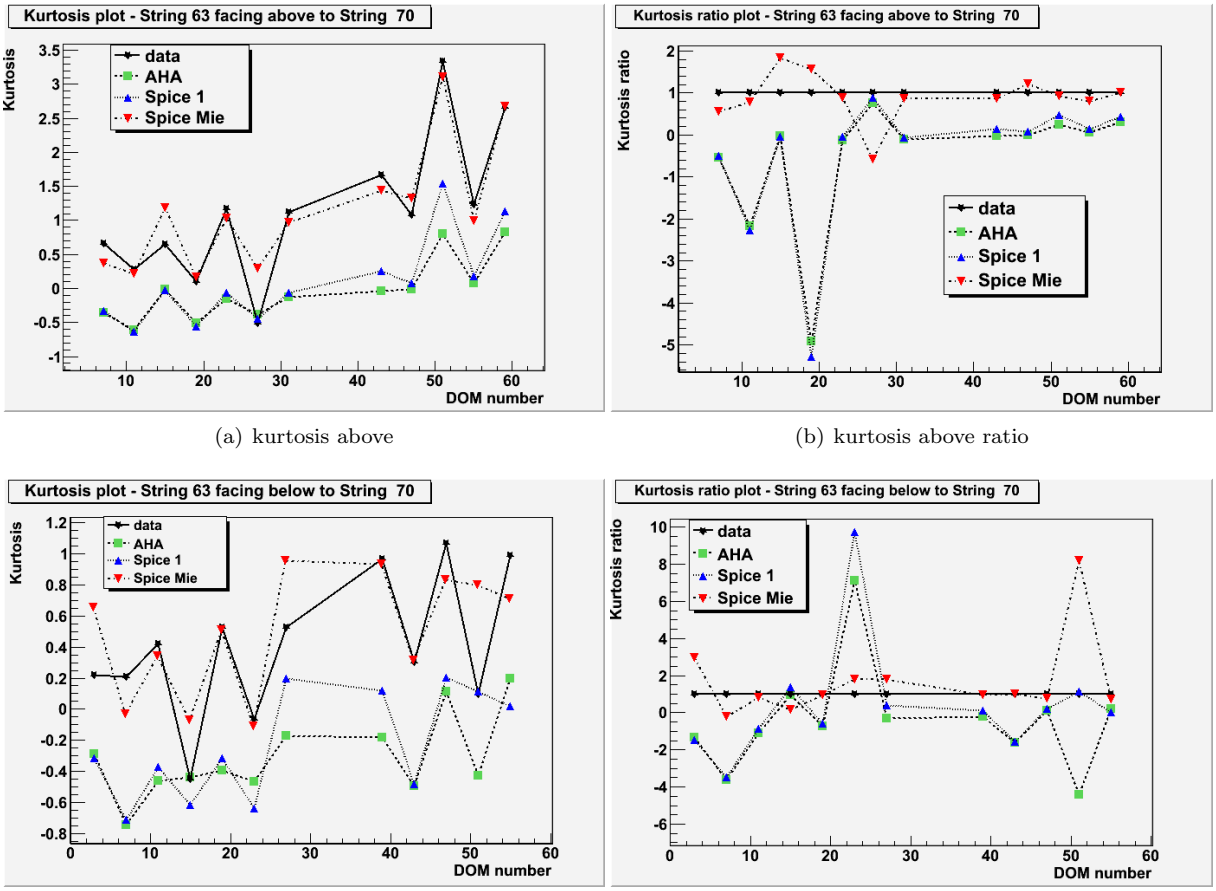

(a) kurtosis above

(b) kurtosis above ratio

(c) kurtosis below

(d) kurtosis below ratio

Figure 7.9: Kurtosis plots for string 63 flashing facing string 70 receiving on DOMs four above(a and b) and four below (c and d) the source. Plots a and c show the kurtosis as a function of depth with an upward trends as depth increases. Plots b and d show the same results but as a ratio of the flasher data.

and data kurtosis values is over thirty. This is largely due to the fact that the data kurtosis value is close to zero. This also occurs when looking at the photon distributions above and below the emitting DOM. In particular when emitting at DOM 19 and receiving on DOM 23 and when emitting from DOM 23 receiving on DOM19 large values of the ratio occur. The close correlation between the shape of the AHA and Spice arrival time distributions is again displayed in the kurtosis values.

Mean

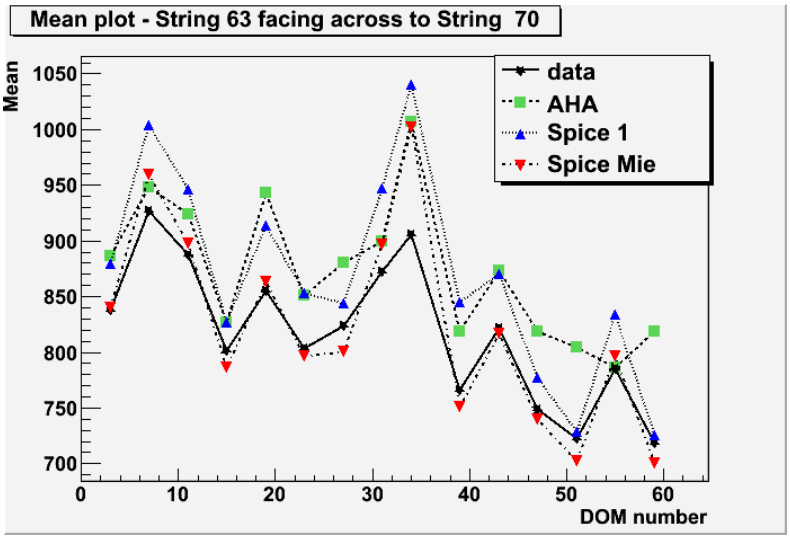

(a) mean across

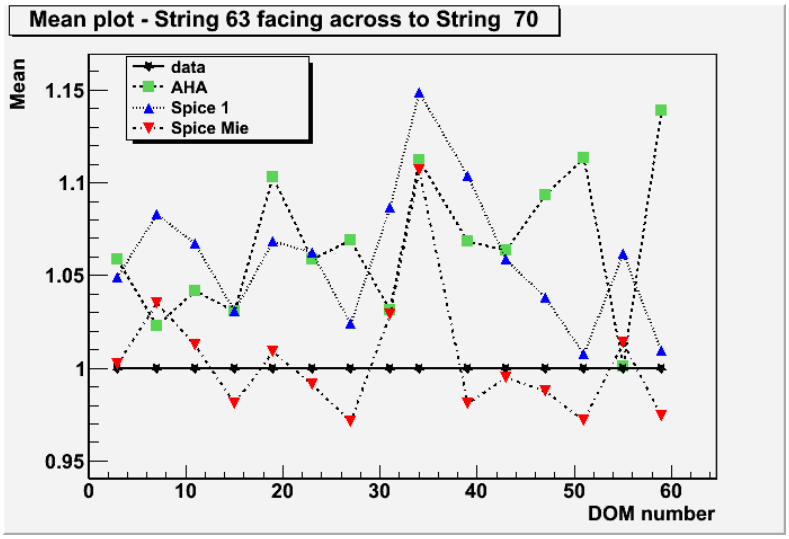

(b) mean across ratio

Figure 7.10: Mean values plotted for string 63 flashing facing string 70 receiving on the DOM directly across from the source. Plot a shows the mean as a function of depth with a downward trend as depth increases. Plot b shows the same results but as a ratio of the flasher data.

The mean values of the time distributions show a decreasing trend as the depth in the detector increases. That is the photons are arriving earlier, on average, lower down in the detector given that the distance between strings is constant with depth. This is consistent with the fact that there is less scattering and absorption in the deep ice. There is again a significant spike around DOM 34. This same spike was seen in the skewness plots. As explained earlier this region is known to have a higher concentration of dust. This dust results in more scattering and hence the later average arrival time and

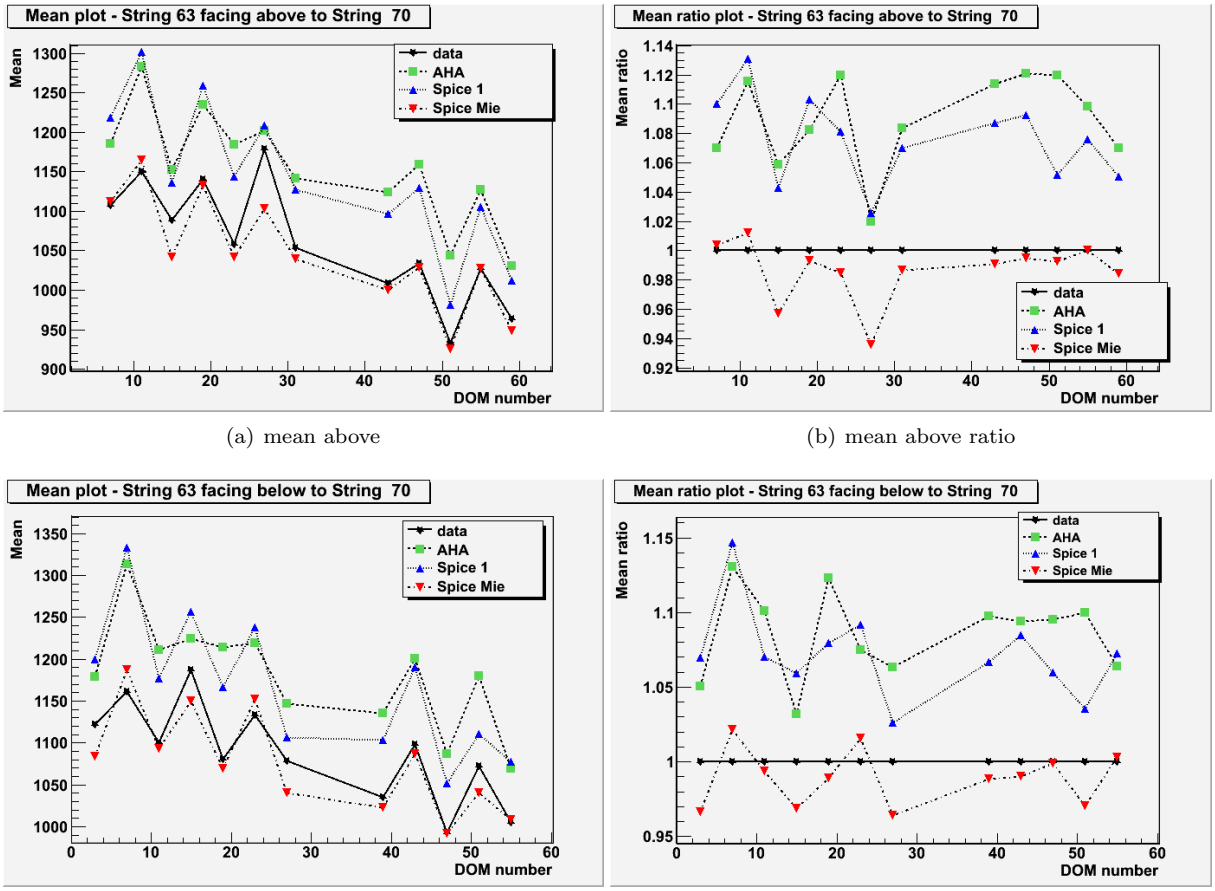

(a) mean above

(b) mean above ratio

(c) mean below

(d) mean below ratio

Figure 7.11: Mean values plotted for string 63 flashing facing string 70 receiving on DOMs four above(a and b) and four below (c and d) the source. Plots a and c show the mean values as a function of depth with an downward trends as depth increases. Plots b and d show the same results but as a ratio of the flasher data.

also more absorption which extinguishes the photons which would have otherwise arrived later.

Again the trend that Spice 1 and AHA are closely related and Spice Mie and the data distributions are related in shape is evident here. When the emitter is facing directly across from the receiver, at greater depths such as DOM 51 and DOM 59 in particular, Spice 1 moves away from AHA and is closer to Spice Mie. The ratio plots again confirm that while the shape of Spice 1 and AHA mimic the flasher data, they are off by an average factor of 0.09, the smallest ratio offset so far from the skewness, kurtosis and mean values.

Overall as far as the shape of the time distribution is the judging criteria, it seems that Spice Mie is providing a good model of the iceproperties save for perhaps a couple of depths. AHA has the lowest χ^2 when viewing above at DOM 27. When viewing below the source, DOM 3, DOM 15, DOM 23 and DOM 27 are not well represented by Spice Mie.

7.2 Emitters pointed away from receivers

As discussed in the previous chapter when the emitting LED is orientated away from the receiving DOM, there is necessarily more scattering required for the light to reach the receiver. This means that for this geometry of emitter and receiver there is less distinction between the distributions received at the same height, and below or above the emitter, than those seen when looking at these same distributions for the emitter-facing-the-receiver geometry.

The χ^2 results for all orientations indicate that Spice Mie provides the best description of the ice. This is true with or without the inclusion of a time shift. Including the time shift has a minimal effect when the emitter is pointed away from the receiver.

There continue to be a few depths were Spice 1 or AHA provide the best description. Some of these depths are different than the depths for the emitter facing the receiver (see Figures 7.12 and 7.14). The depths where Spice Mie does not provide the best fit are all below the depth of DOM 47.

When the emitter is pointed away from the receiver, the skewness, kurtosis and mean values also yield similar results to those when the emitter is facing the receiver. Spice Mie's distribution is matched closest with the flasher data and Spice 1 and AHA have similar values, but the correlations are not as strong. One difference is that when the emitter is pointed away from the receiver there is less of a detectable trend over the depths of the detector. Kurtosis displays only a very small downward trend.

Chi Squared for the emitters pointed away from receivers directly across from the source

With the the emitter pointed away from the receiver directly across on string 70, there is little deviation from Spice Mie providing the best fit from the flasher data at most depths. Above the dust layer, Spice Mie's fit produces the lowest χ^2, as displayed in Table 6.7 to Table 6.8 and Figure 7.12. Below the dust layer there is some variation between ice models in terms of statistical tests. If the time distribution is shifted, Spice Mie's fit matches best except at DOM 51 and DOM 55 where Spice 1 has the best fit. Figure 7.13 shows visually, for the most part, all models are within the error bars of the flasher data making it difficult to tell which model matches best.

Given that the time shift did not make very much difference between which ice model matched best there is not a noticeable overall trend of the χ^2 values. The models all seem to hold their respective orientation but are slightly different downscaled. This decrease is most significant when receiving directly across from the emitter. Another feature noticed was that AHA and Spice 1 are still strongly coupled even at the greater depths where Spice 1 pulled away from AHA when the emitter was facing the receiver.

All the shifts are negative for all ice models except for Spice 1's fit at DOM 51 and AHA at DOM 55. For the most part, Spice 1's fit and AHA's fit have the largest shift. The negative shift would

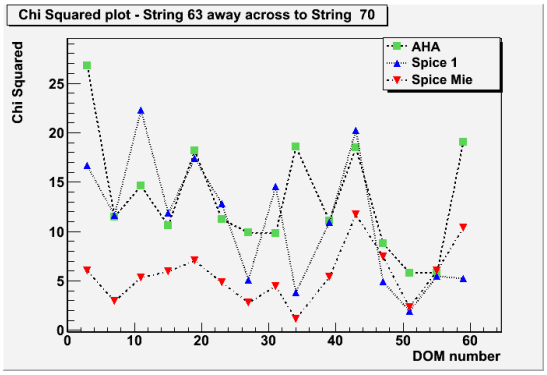

(a) Chi squared across

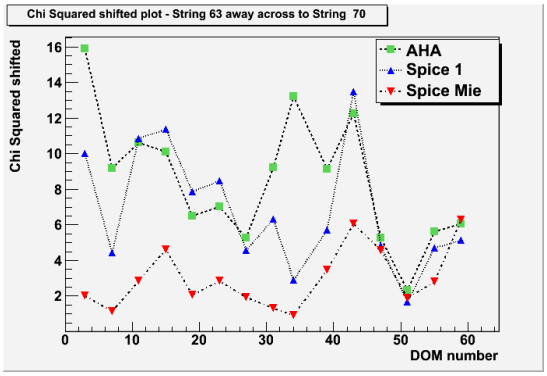

(b) Shifted Chi squared across

Figure 7.12: Chi squared plots as a function of depth for the three different ice models being compared. These plots focus on string 63 flashing away from string 70 receiving on the DOM directly across from the source. Plot a shows the χ^2 results and plot b shows the χ^2 results with the time shift.

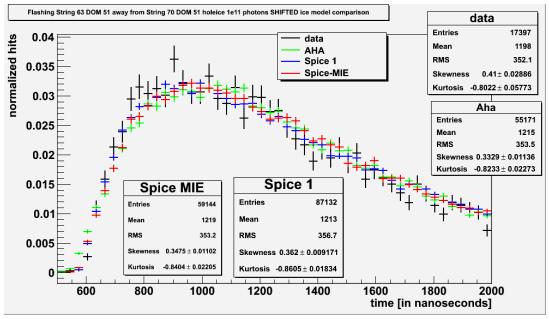

(a) DOM 51

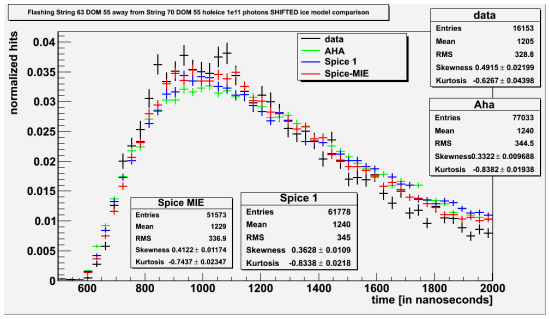

(b) DOM 55

Figure 7.13: String 63 flashing away from string 70 receiving on the DOM directly across from the source at the depth of DOM 51 and DOM 55. Spice 1's fit provides the lowest χ^2.

infer that the ice models are detecting the first photons too late when compared with the flasher data. The variations in χ^2 values seem random, with no correlation to absorption and scattering properties or detectable trend.

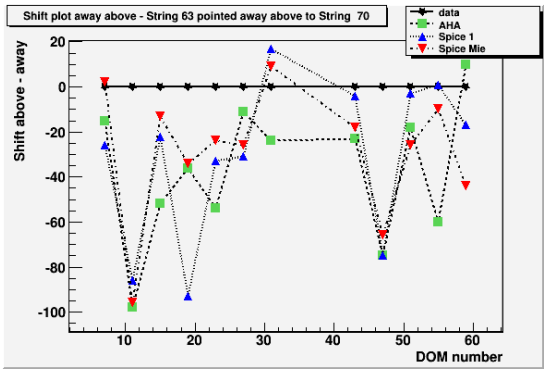

(a) Shift across

Figure 7.14: Time distribution shift values as a function of depth for the three different ice models being compared. These plots focus on string 63 flashing pointed away from string 70 receiving on the DOMs directly across from the source.

Chi Squared for the emitters pointed away from receivers four DOMs from the source

When the receiver is a distance of four DOMs above the receiver, Spice Mie has the best fit across all statistical measurements until DOM 47 (see Tables 6.9 and 6.10). Afterwards, Spice 1 provides the best fit for DOM 47 and AHA provides the best fit for DOM 51, both regardless of the time shift or not. At DOM 59, Spice Mie provides the best fit for the time shifted χ^2; however, all other statistical results indicate AHA's fit matches best with the flasher data. It is unclear at the depth of DOM 59 which model is actually most accurate.

Table 6.11 to Table 6.12 display the results receiving below the source, where Spice Mie's fit is uncontroversially the best except at the depth of DOM 47 where Spice 1 gives the best fit after the time shift is incorporated. This depth is unusual in that all the ice models had a positive shift; elsewhere, the shift was negative. AHA and Spice 1 usually had the highest shift, yet rarely the lowest χ^2.

There were a few depths in all settings where Spice Mie's fit did not have the lowest χ^2. This was not caused by low statistics or by a premature peak as this never occurred when the emitter was pointed away from the receiver. If AHA or Spice 1 did provide the best fit, it was always at the greater depths of the detector. Receiving below from the source showed the most consistency with Spice Mie's fit matching the flasher data best.

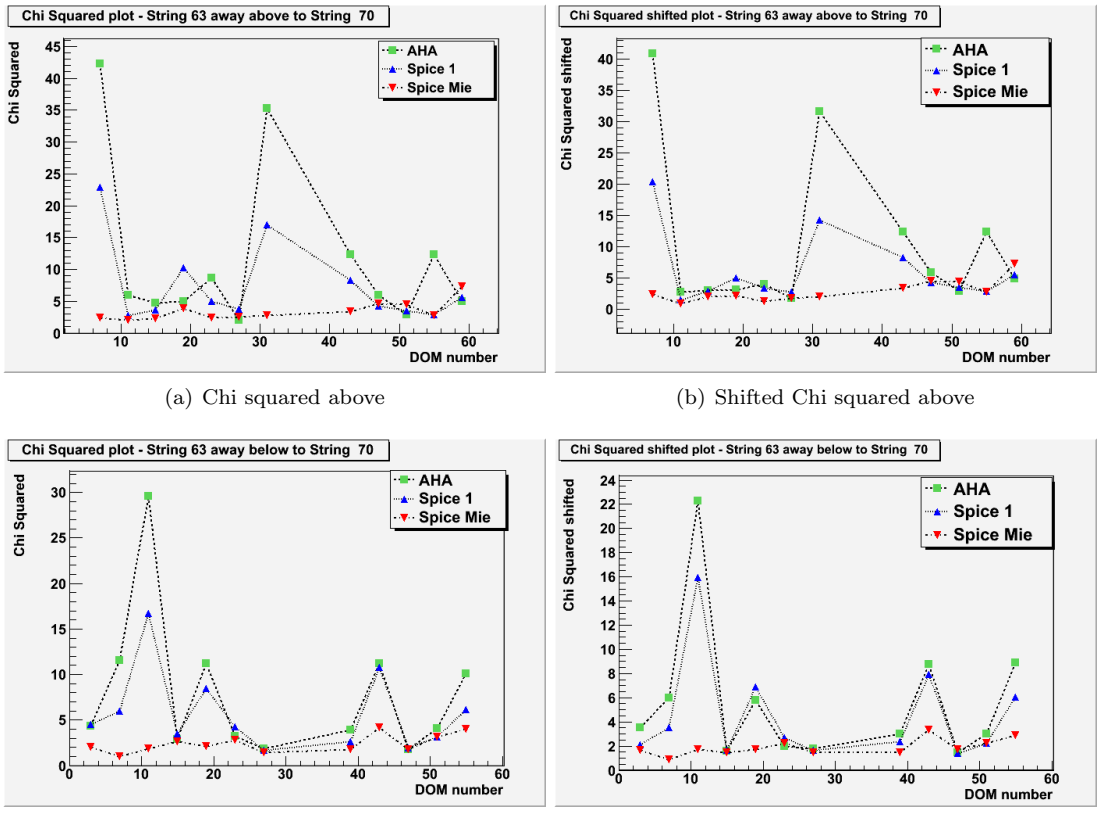

(a) Chi squared above

(b) Shifted Chi squared above

(c) Chi squared below

(d) Shifted Chi squared below

Figure 7.15: Chi squared plots as a function of depth for the three different ice models being compared. These plots focus on string 63 flashing away from string 70 receiving on the DOMs four above(a and b), and four DOMs below(c and d) from the source. Plots a and c show the χ^2 results and plot b and d show the time shifted χ^2 results.

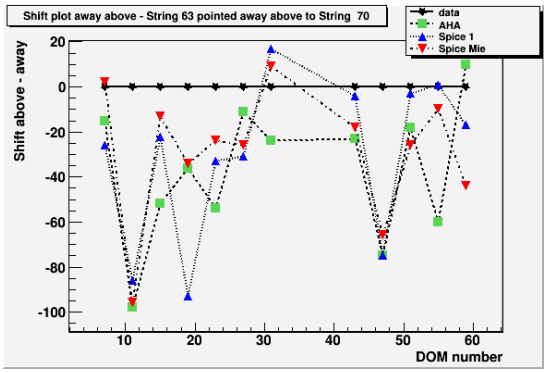

(a) Shift above

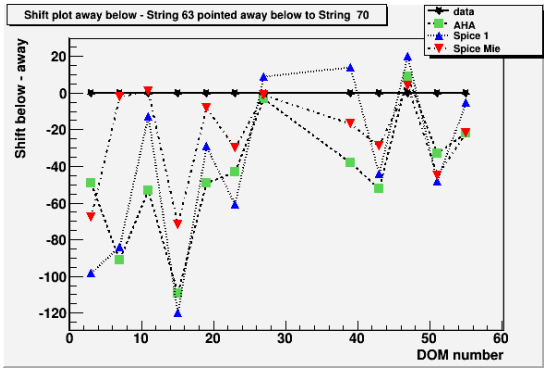

(b) Shift below

Figure 7.16: Time distribution shift values as a function of depth for the three different ice models being compared. These plots focus on string 63 flashing pointed away from string 70 receiving on the DOMs four above and four below from the source.

7.2.1 Statistical trends for emitter pointed away from receivers

The patterns that were seen when the emitter was facing the receiver were not apparent when pointed away from the receiver. The skewness, kurtosis and mean values all remained relatively stable as the depths changed. There was also no correlation with the shift values or direction with the absorption and scattering properties.

Skewness

The skewness values show little variation and no detectable trend as seen in Figure 7.17. The big peak is from the dust layer. Spice 1 and AHA are still strongly coupled. Figure 7.18 shows that the variation becomes much more erratic when receiving on a DOM above or below the source. Especially receiving above the source, the offset between AHA and Spice 1 with Spice Mie and the flasher data is apparent. Skewness results are usually positive except at two depths.

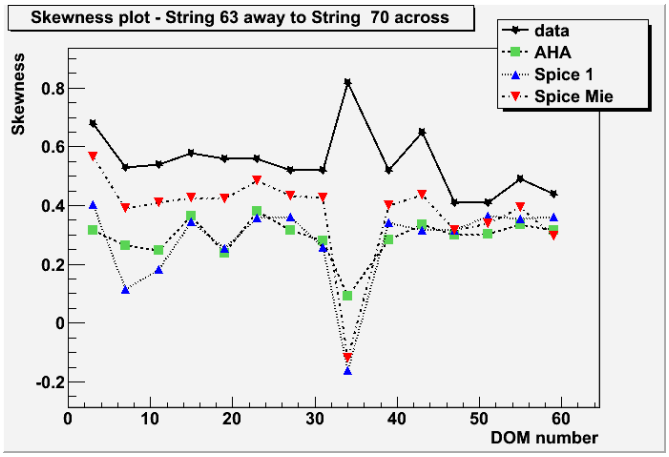

(a) skewness across

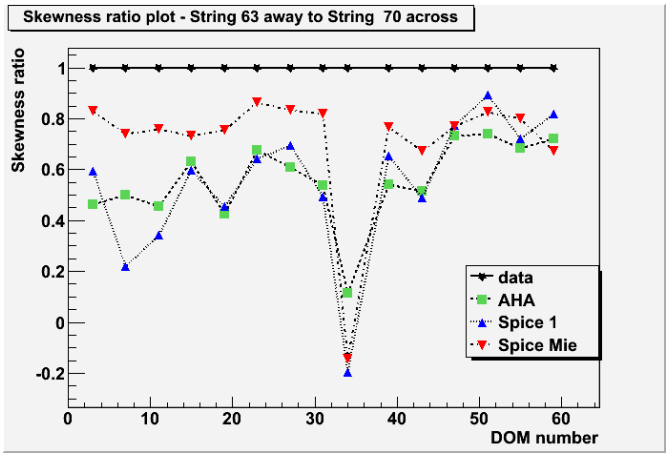

(b) skewness across ratio

Figure 7.17: Skewness plots for string 63 flashing away from string 70 receiving on the DOM directly across from the source. Plot a shows the skewness as a function of depth. Plot b shows the same results but as a ratio of the flasher data.

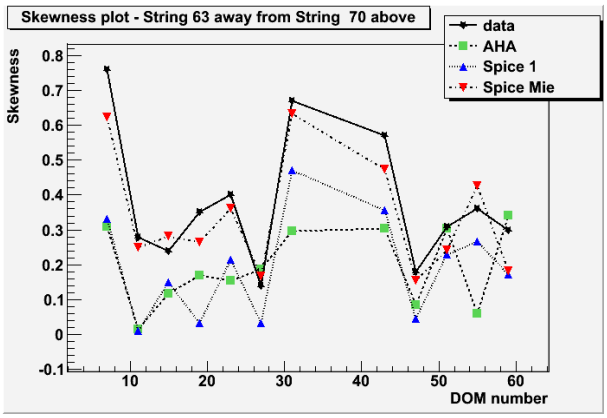

(a) skewness above

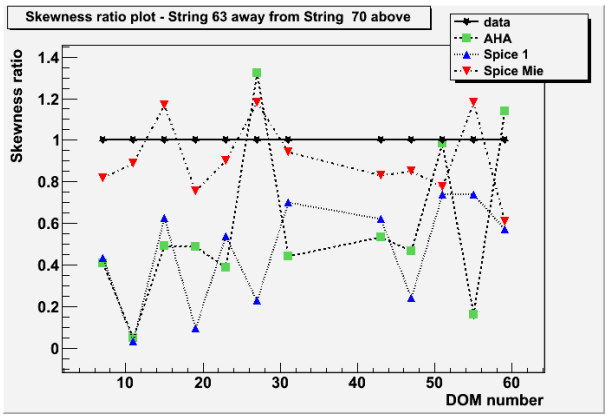

(b) skewness above ratio

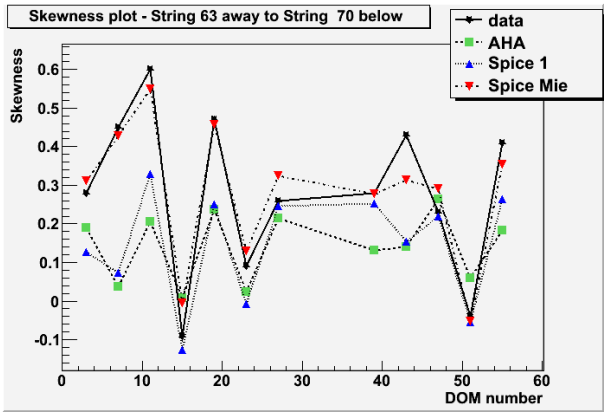

(c) skewness below

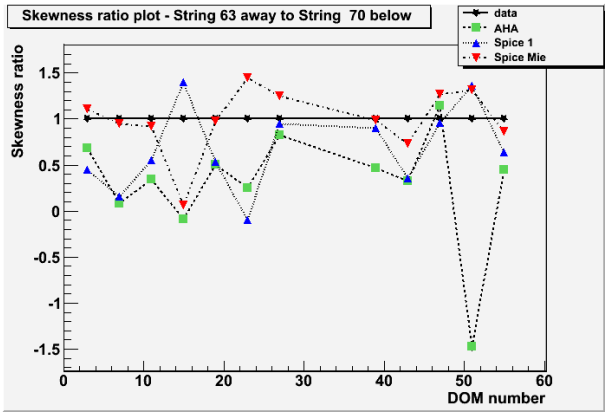

(d) skewness below ratio

Figure 7.18: Skewness plots for string 63 flashing away from string 70 receiving on DOMs four above(a and b) and four below (c and d) the source. Plots a and c show the skewness as a function of depth. Plots b and d show the same results but as a ratio of the flasher data.

Kurtosis

Figure 7.19 portrays the kurtosis values and shows very little variation with only one deviation at the dust layer. Spice 1 and AHA are extremely similar when the emitter is directly across from the receiver. This pattern carries on when the emitter is above or below the receiver in Figure 7.20. The kurtosis values are all negative and relatively stable except at DOM 3 where there is a very low kurtosis. In turn, the ratio between flasher data and Monte Carlo is high at this depth. Still, Spice Mie provides the best fit. The range of kurtosis values is greater when receiving above. When receiving below, the kurtosis values fluctuate marginally less than when receiving four DOMs above and are always negative.

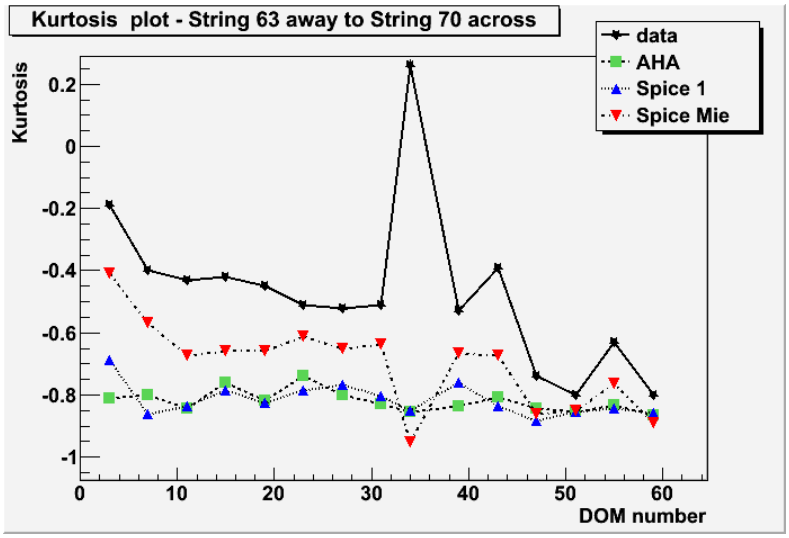

(a) kurtosis across

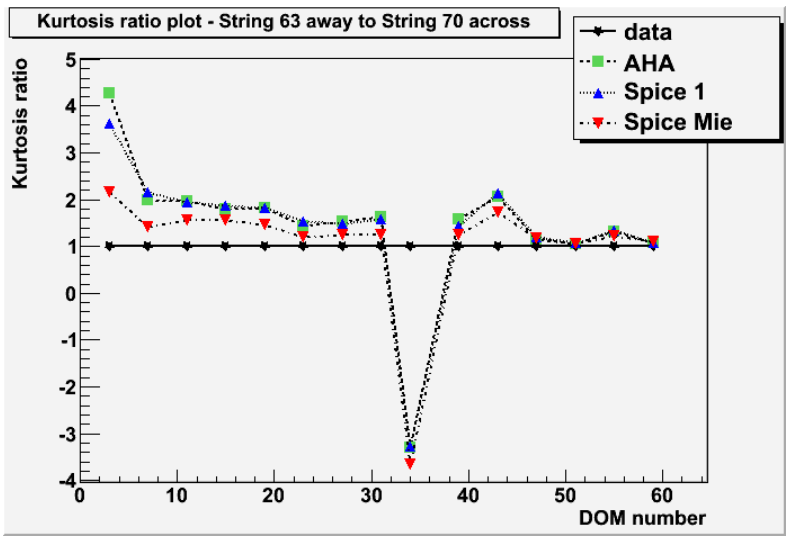

(b) kurtosis across ratio

Figure 7.19: Kurtosis plots for string 63 flashing away from string 70 receiving on the DOM directly across from the source. Plot a shows the kurtosis as a function of depth. Plot b shows the same results but as a ratio of the flasher data.

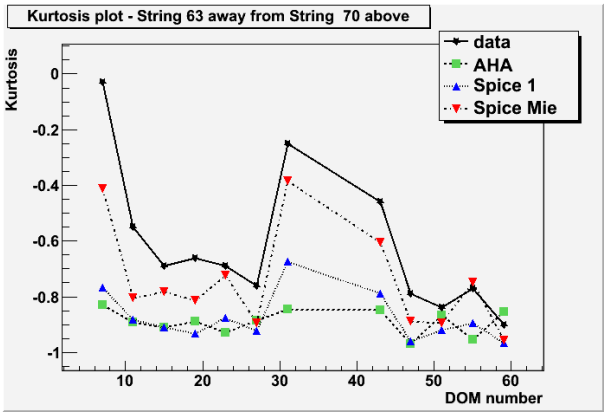

(a) kurtosis above

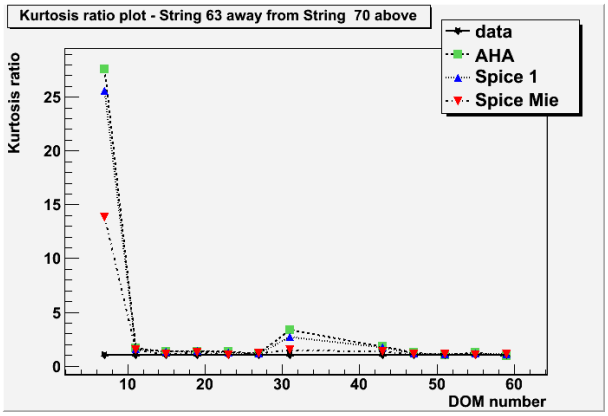

(b) kurtosis above ratio

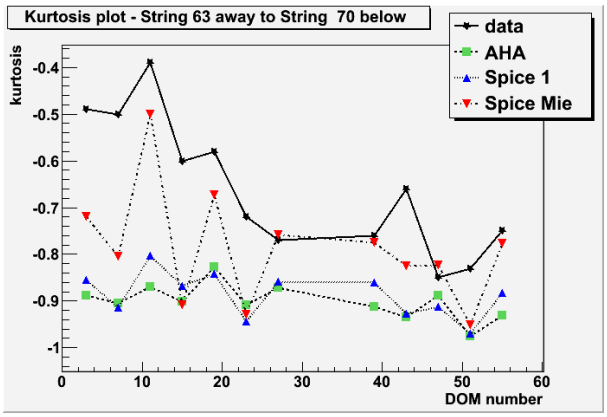

(c) kurtosis below

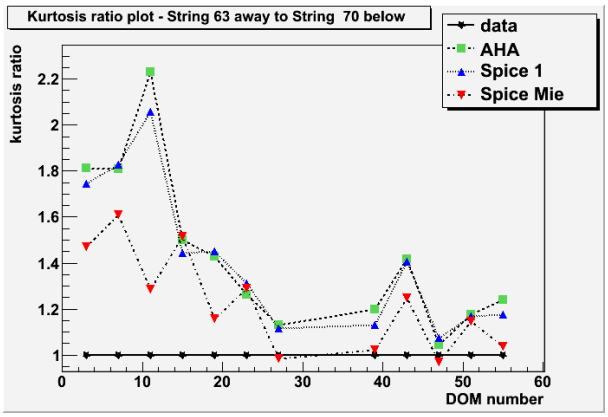

(d) kurtosis below ratio

Figure 7.20: Kurtosis plots for string 63 flashing away from string 70 receiving on DOMs four above(a and b) and four below (c and d) the source. Plots a and c show the kurtosis as a function of depth. Plots b and d show the same results but as a ratio of the flasher data.

Mean

The mean values shown in Figure 7.21 display a decoupling between Spice Mie and the flasher data, yet the trend still follows closely. When receiving above or below, in Figure 7.22, the range of values is similar to those when receiving directly across. The pattern is still eratic and shows no distinguishable correlation.

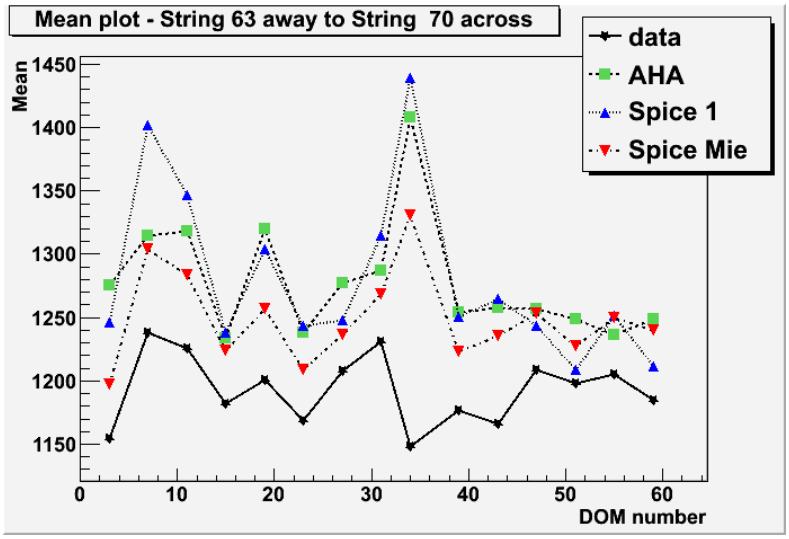

(a) mean across

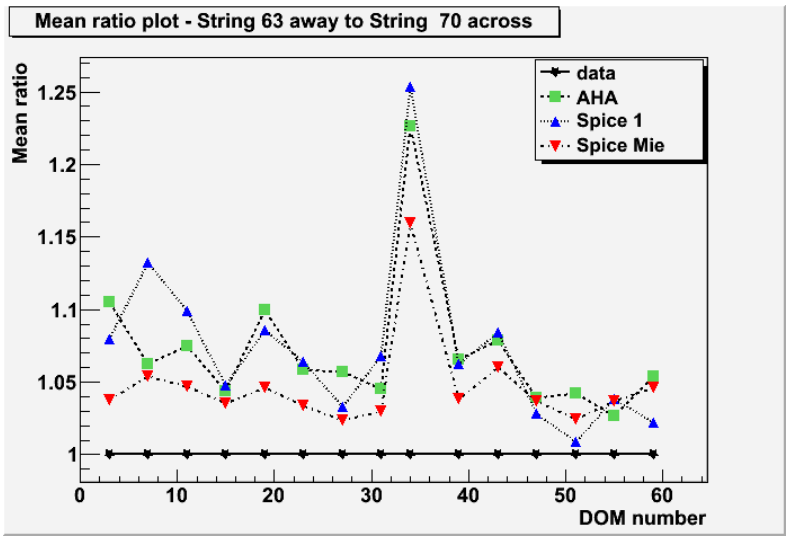

(b) mean across ratio

Figure 7.21: Mean values plotted for string 63 flashing away from string 70 receiving on the DOM directly across from the source. Plot a shows the mean as a function of depth with a downward trend as depth increases. Plot b shows the same results but as a ratio of the flasher data.

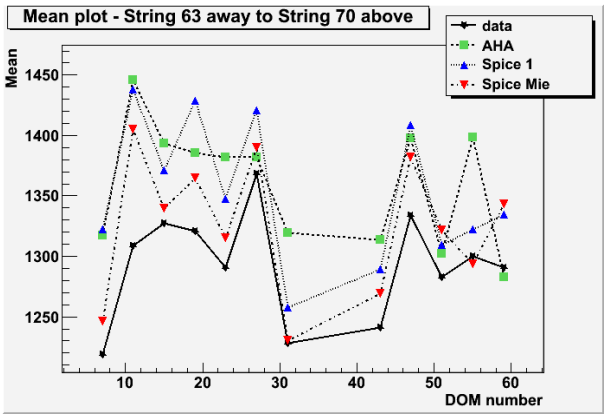

(a) mean above

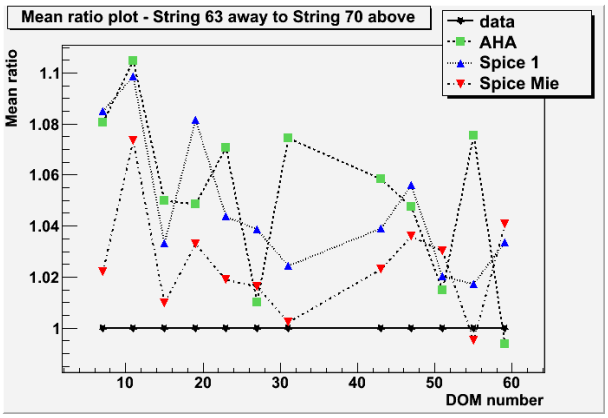

(b) mean above ratio

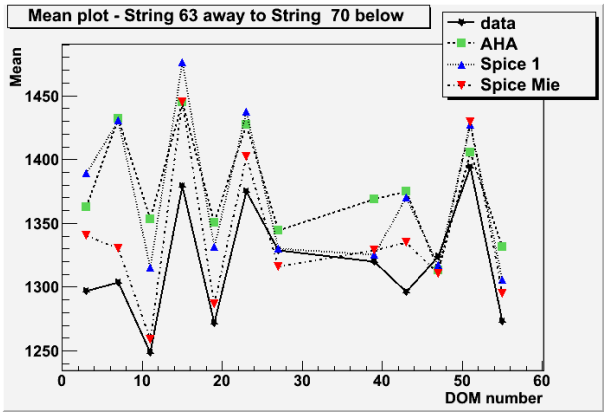

(c) mean below

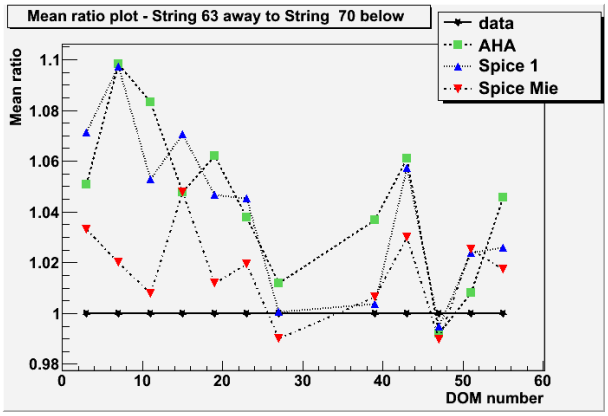

(d) mean below ratio

Figure 7.22: The mean values plotted for string 63 flashing away from string 70 receiving on DOMs four above(a and b) and four below (c and d) the source. Plots a and c show the mean as a function of depth. Plots b and d show the same results but as a ratio of the flasher data.

Chapter 8

Tilting the LED angle

In the studies described in the previous chapter, the LED flashers are assumed to be at points of well known zenith and azimuth angles. However, there are uncertainties associated with these angles. Simulations were conducted altering the angle of the flashing LED to investigate these effects. The simulated data was compared with the Single Photon Electron (SPE) flasher data as described in section 5. Two different depths were studied to consider vertical effects, DOM 23 at a depth of $1,840$ m and DOM 55 at a depth of $2,385$ m.

In the horizontal plane the uncertainties associated with the LED angle are around 10-15 degrees with an angular variation greater than 30 degrees being extremely unlikely [56]. While the zenith angle uncertainties are around 10 degrees. In this study the effect of variations ± 30 degrees in the azimuth and ± 20 degrees in the zenith angle were studied. To change the horizontal tilt of the LEDs, the angle implemented in PPC was adjusted accordingly. The angle of the LED most directly orientated towards the receiving string was found in the table provided by C. Wendt [56, 57]. To alter the vertical tilt of an LED, the pro.cu code was altered, please see Appendix B.6 for further details.

The tilting effects were analysed by comparing the normalized shape of the time distribution as done in the previous study. This mode of comparison is necessary as directly comparing the number of hits is inappropriate since a precise brightness of the LEDs is unknown. However, the number of hits received is useful when comparing relative percentages. The percentage of the change in hit count was calculated using the ice model which showed the greatest absolute change in hit count and dividing this difference by the largest hit count from the respective ice model.

To further the quantitative comparison χ^2 tests and other statistical values such as the skewness, kurtosis and mean were calculated. The values were calculated for the tilted and non-tilted versions to see which one matched closest with that of the flasher data. The full set of results are displayed in Tables

8.2, 8.3, 8.5, 8.6.

8.1 Tilting at DOM 23

Figure 8.1 shows the horizontal tilting effects for a relatively high location in the IceCube detector at DOM 23. The positive tilt causes all the peaks to decrease with more hits received at a later time widening the tail of the time distribution. For the negative tilt the distributions remain fairly similar with only minor fluctuations in the peak which is equally reflected in the tail for the DOM four below on the receiving string. The Spice 1 distributions changes less than the Spice Mie distributions.

Table 8.1: Difference in percentage between non-tilted and titled simulations for DOM 23. Using the ice model which showed the greatest change in hit count, the percentage was calculated by dividing the this difference by the greatest hit count be it tilted or non-tilted.

DOM 23				
position	$+30°$	$-30°$	$+20°$	$-20°$
four DOMs above	-30%	$+5\%$	$+14\%$	-25%
directly across	-32%	$+2\%$	$+13\%$	-24%
four DOMs below	-27%	$+3\%$	-19%	$+10\%$

Table 8.1 displays the percentage change in hit count. While the shape showed a minimal change in the peak for a negative horizontal tilt, the number of hits showed an increase. However, this percentage is much smaller than the change recorded for a positive tilt. The positive tilt averages a change of 30% where the negative tilt changes by 3% on average. Visibly Spice Mie has a greater change in timing distribution; however, when consulting the number of hits, the Spice 1 results changes by a greater amount than those from Spice Mie at DOM 19 with a negative horizontal tilt.

Figure 8.2 shows the plots for vertically tilting DOM 23 by 20 degrees. The changes in shape are marginal but seem to be responding to the tilting angles appropriately. The peak increases in the DOM four above when the LED is tilted upward as it decreases below, the opposite occurs for a negative tilt. The changes in shape for the DOMs directly across is hardly noticeable. There are no changes in the tail of the time distribution.

The differences in the ice models follow suit as before with the Spice 1 distributions changing less than those from Spice Mie. Again in the DOM four below with a negative tilt, the peak for Spice Mie increases whereas the peak for Spice 1 decreases. This difference is further supported when consulting the change in the number of hits as described in the paragraph below.

Despite the changes in shape, none allow for a better fit between the simulation and the flasher data. The only improvement is seen in the DOM four below when the LED source is negatively tilted.

The general lack of clear change in the shape distribution indicates the tilting does not seem to greatly improve the fit between the ice model and flasher data, or this study was not comprehensive enough to notice any changes.

The number of hits received from flashing DOM 23 with vertically tilted LEDs follows the logical pattern also shown by the shape of the timing distribution. The number of hits received by a DOM increases when the LED is pointed towards the receiver, also showing the greatest change in percentage of hits. The largest change in hit count comes from the DOM four above regardless of the tilting direction. See Table 8.1 for the full results. For the most part Spice Mie had a greater response to the tilt changes than Spice 1. There was an inconsistency for the DOM four below with downward vertical tilt when the shape of the timing distribution for Spice 1 changed in the opposite direction as Spice Mie. The change in the number of hits shows that Spice 1 did see a greater change in hits than Spice Mie. This also occurred for the DOM four below with an upward tilt however, the Spice 1 time distribution changes shape in the same direction as Spice Mie. All together, the change in the number of hits does not provide insight into any improvements due to tilting.

Combining all the results from the χ^2 statistical test, skewness, kurtosis and mean values, there are only a few settings where the tilting seems to have improved the Monte Carlo fits (Tables 8.2 and 8.3). These possible examples for DOM 23 with a positive vertical tilt when receiving above, a negative vertical tilt when viewing below, a positive horizontal tilt when receiving below and a negative horizontal tilt when receiving directly across. In most cases the improvements in the χ^2 values were minimal.

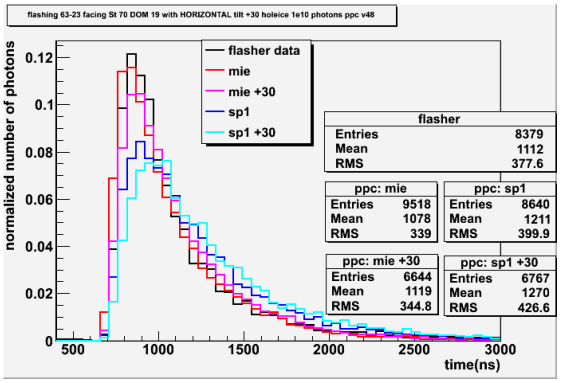

(a) String 63 DOM 23 flashing towards String 70 DOM 19 with a horizontal tilt of +30

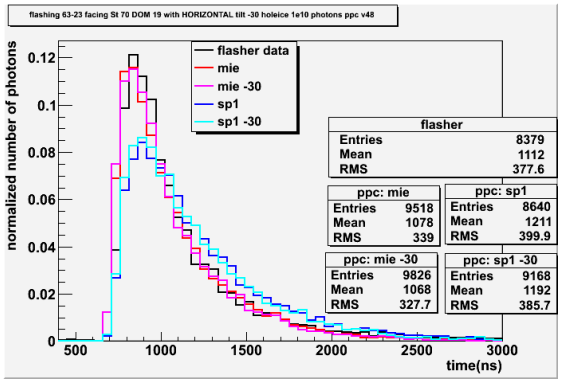

(b) String 63 DOM 23 flashing towards String 70 DOM 19 with a horizontal tilt of -30

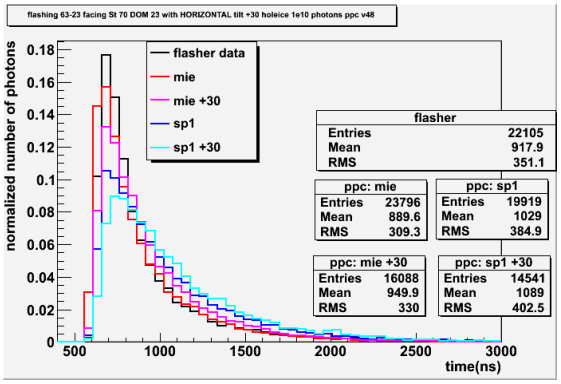

(c) String 63 DOM 23 flashing towards String 70 DOM 23 with a horizontal tilt of +30

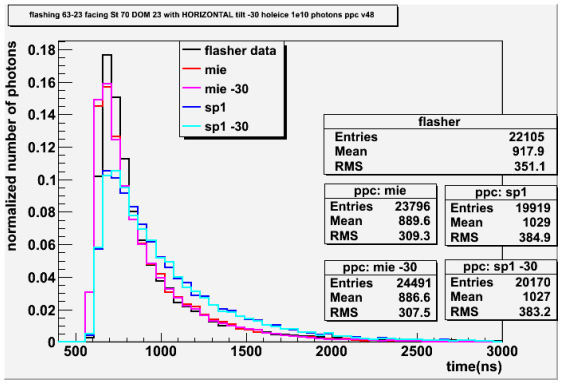

(d) String 63 DOM 23 flashing towards String 70 DOM 23 with a horizontal tilt of -30

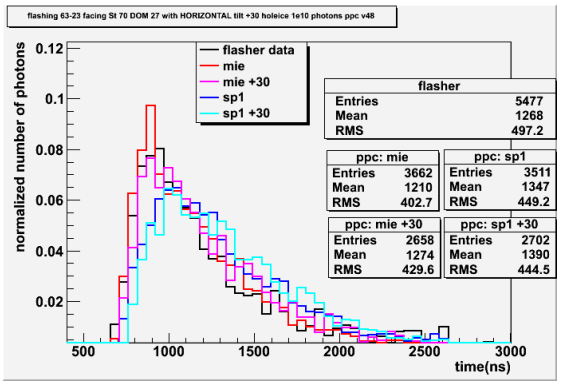

(e) String 63 DOM 23 flashing towards String 70 DOM 27 with a horizontal tilt of +30

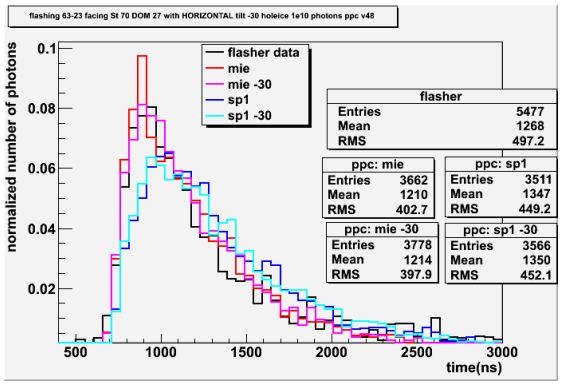

(f) String 63 DOM 23 flashing towards String 70 DOM 27 with a horizontal tilt of -30

Figure 8.1: String 63 DOM 23 flashing towards String 70 DOM 23 with a horizontal tilt of 30 degrees.

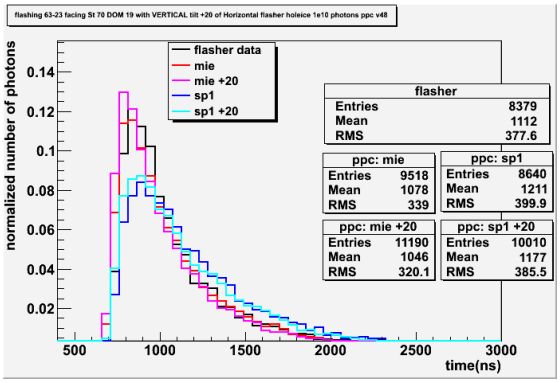

(a) String 63 DOM 23 flashing towards String 70 DOM 19 with a vertical tilt of +20. χ^2: Spice Mie = 4.6089, Spice Mie VT = 9.38499, Spice 1 = 9.17863, Spice 1 VT = 6.47676.

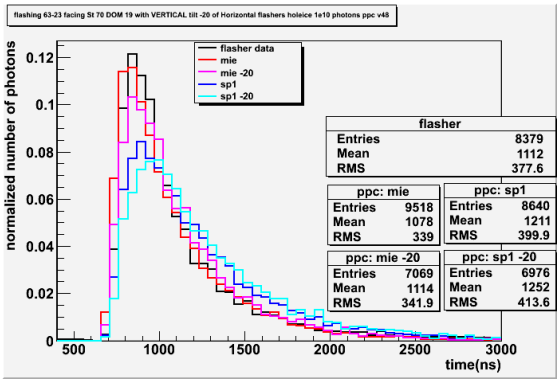

(b) String 63 DOM 23 flashing towards String 70 DOM 19 with a vertical tilt of -20. χ^2 = Spice Mie = 4.6089, Spice Mie VT = 9.38499, Spice 1 = 3.02157, Spice 1 VT = 14.7064.

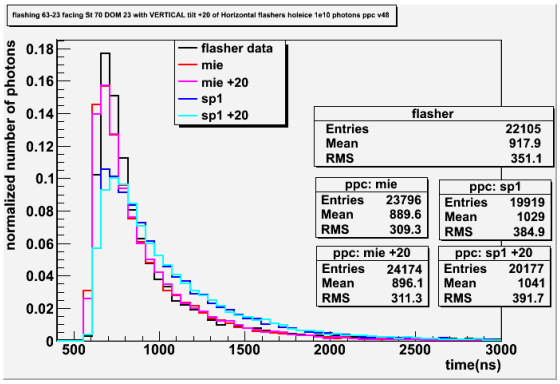

(c) String 63 DOM 23 flashing towards String 70 DOM 23 with a vertical tilt of +20.χ^2: Spice Mie = 17.8697, Spice Mie VT = 34.4984, Spice 1 = 10.8, Spice 1 VT = 40.6584.

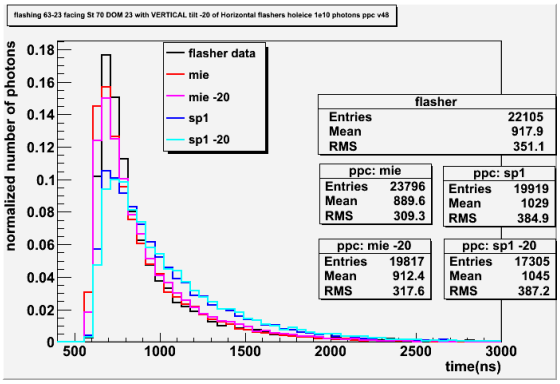

(d) String 63 DOM 23 flashing towards String 70 DOM 23 with a vertical tilt of -20. χ^2: Spice Mie = 17.8697, Spice Mie VT = 34.4984, Spice 1 = 15.3795, Spice 1 VT = 39.5714

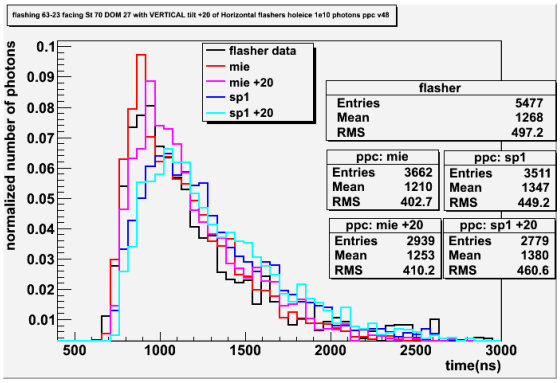

(e) String 63 DOM 23 flashing towards String 70 DOM 27 with a vertical tilt of +20. χ^2: Spice Mie = 3.75246, Spice Mie VT = 6.02605, Spice 1 = 3.69217, Spice 1 VT = 6.44858

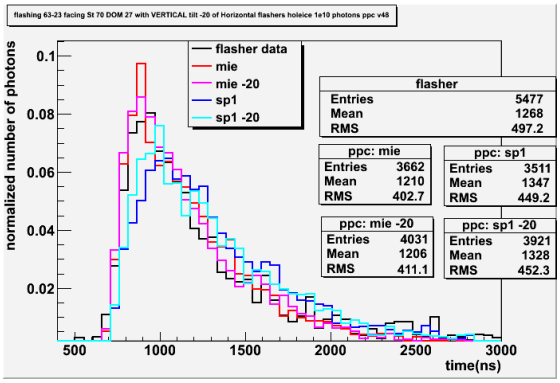

(f) String 63 DOM 23 flashing towards String 70 DOM 27 with a vertical tilt of -20. χ^2: Spice Mie = 3.75246, Spice Mie VT = 6.02605, Spice 1 = 3.4372, Spice 1 VT = 5.23839.

Figure 8.2: String 63 DOM 23 flashing towards String 70 DOM 23 with a vertical tilt of 20 degrees.

Table 8.2: DOM 23 horizontal tilt

	Positive tilt				Negative tilt			
ice model	χ^2	skewness	kurtosis	mean	χ^2	skewness	kurtosis	mean
Four DOMs above								
Data	–	2.01	4.68	1112	–	2.01	4.68	1112
Mie	4.61	1.81	4.11	1078	4.61	1.81	4.11	1078
Mie Tilt	2.46	1.72	3.65	1119	5.26	1.8	4.03	1068
Sp1	9.38	1.44	2.14	1211	9.38	1.44	2.14	1211
Sp1 Tilt	16.68	1.37	1.75	1270	7.87	1.46	2.4	1192
Directly across								
Data	–	2.51	7.63	918	–	2.51	7.63	918
Mie	17.87	2.19	6.31	890	17.87	2.19	6.31	890
Mie Tilt	11.35	1.2	5.19	950	18.14	2.17	6.14	887
Sp1	34.5	1.72	3.47	1029	34.49	1.72	3.47	1029
Sp1 Tilt	61.49	1.56	2.66	1089	34.12	1.74	3.57	1027
Four DOMs below								
Data	–	1.39	1.45	1268	–	1.39	1.45	1268
Mie	3.75	1.44	2.24	1210	3.75	1.44	2.24	1210
Mie Tilt	3.49	1.27	1.39	1274	3.79	1.41	2.17	1214
Sp1	6.03	1.15	1.02	1347	6.03	1.15	1.02	1347
Sp1 Tilt	8.34	1.06	0.84	1390	6.16	1.1	0.84	1350

Table 8.3: DOM 23 Vertical tilt

	Positive tilt				Negative tilt			
ice model	χ^2	skewness	kurtosis	mean	χ^2	skewness	kurtosis	mean
Four DOMs above								
Data	–	2.0	4.68	1112	–	2.01	4.68	1112
Mie	4.61	1.81	4.11	1078	4.61	1.81	4.11	1078
Mie Tilt	9.18	1.84	4.21	1046	3.02	1.7	3.6	1114
Sp1	9.38	1.44	2.14	1211	9.38	1.44	2.14	1211
Sp1 Tilt	6.48	1.46	2.34	1177	14.71	1.37	1.84	1252
Directly across								
Data		2.51	7.63	918		2.51	7.63	918
Mie	17.87	2.19	6.31	890	17.87	2.19	6.31	890
Mie Tilt	15.38	2.13	5.94	896	10.8	2.06	5.42	912
Sp1	34.49	1.72	3.47	1029	34.49	1.72	3.47	1029
Sp1 Tilt	39.57	1.69	3.26	1041	40.66	1.63	3.02	1045
Four DOMs below								
Data		1.39	1.45	1268		1.39	1.45	1268
Mie	3.75	1.44	2.24	1210	3.75	1.44	2.24	1210
Mie Tilt	3.69	1.36	1.79	1253	3.43	1.48	2.3	1206
Sp1	6.03	1.15	1.02	1347	6.03	1.15	1.02	1347
Sp1 Tilt	6.45	1.13	0.91	1380	5.24	1.18	1.12	1328

8.2 Tilting at DOM 55

The plots in Figure 8.3 show the changes from a horizontal tilt of 30 degrees for DOM 55. The flasher data is compared with two different ice models, Spice 1 and Spice Mie for both original and tilted simulations. The differences in time distribution shape shows the amount of variability in ice models that can be attributed to horizontal tilting of the emitting LED.

In all cases of horizontal tilt, a decrease in the peak is seen for both ice models with Spice Mie decreasing more than Spice 1. A greater decrease in the peak is seen for a positive tilt of 30 degrees. Because the plot is normalized a decrease in the peak causes the tail to increase.

Table 8.4: Difference in percentage between non-tilted and titled simulations for DOM 55. Using the ice model which showed the greatest change in hit count, the percentage was calculated by dividing the this difference by the greatest hit count be it tilted or non-tilted.

DOM 55				
position	$+30°$	$-30°$	$+20°$	$-20°$
four DOMs above	-14%	-8%	$+12\%$	-18%
directly across	-21%	-9%	-24%	$+15\%$
four DOMs below	-14%	-6%	-32%	$+25\%$

The changes in shape as a reflection of the number of hits are presented in Table 8.4 which presents the Monte Carlo hit count as a percentage of the flasher data. The decrease in hit count is greater for a positive horizontal tilt of 30 degrees than in the negative direction. The Spice 1 results have a smaller change in the number of hits than Spice Mie. The largest change was 21% for a positive tilt of 30 degrees looking directly across. An increase in hit count points out one of the differences between DOM 55 and DOM 23: there was no positive increase in the percentage hit count for DOM 55. This change could be indicative of varying ice properties surrounding the DOMs. For instance, DOM 55 lies in a trough of clean ice; above is cleaner ice and below is dirtier ice. The opposite is seen for DOM 23 at a peak of clean ice. The ice surrounding DOM 23 is dirtier above and cleaner below. Taking this into consideration, a pattern arises in that the largest change in hit number is seen in the dirtier ice regardless of the tilt direction. In the cleaner ice, the light is able to propagate further stabilizing the hit count even if the source is not directly orientated toward the receiver. In the dirtier ice, the orientation of the light source has a larger impact on the number of hits received as the higher absorption and scattering properties dampen out the light propagation.

The vertical tilt plots in Figure 8.4 show interesting results as well. The shape of the distribution responds to the direction of the tilt as expected; when the LED is angled upward, the time distribution increases in its peak while below there is a decrease in the peak. A similar phenomena occurs for a

negative tilt but with reverse effects; when the LED is pointed downward there is an increase below and a decrease above. Whether above or below, the ice model fit to the flasher data improves when the LED is pointed towards the receiving DOM increasing the peak of the early time distributions. For the DOMs directly across the change is much smaller, the negative vertical tilt showing the least change. This would confirm that when the light source is angled towards a receiver more hits are received at an earlier time. As for the difference in ice models, the results are similar to the horizontal tilt, Spice 1 is a weaker shadow of the stronger reactions to the tilting as seen in Spice Mie.

Similarly to the shape of the peak, the number of hits received logically follows the direction of the tilt: more hits are received in the DOM four above when the LED is tilted upward. Conversely, more hits are received on the DOM four below when the LED is tilted downward. The DOMs below the source show the greatest change in the number of hits regardless of the direction of the tilt. This may be an effect under the influence of the PMTs being on the bottom of the DOMs. The photons have to undergo more scattering to reach the PMT which amplifies the effects when the LED is pointed towards or away from the receiving DOM. The largest change in percentage of hits is approximately 34%, this is larger than for the horizontal tilting.

For the most part the change in hit percentage follows the changes in the shape except for the DOMs directly across. The DOMs directly across from the source show a greater change in the number of hits but relatively no change in the shape of the time distribution. Under these conditions, it is hard to tell if vertically tilting the LEDs has actually improved the fit of the ice model. See Table 8.4 for a full set of results.

The change in shape can also be seen in the skewness, kurtosis and mean values which are displayed in Figures 8.5 and 8.6 for DOM 55. These tables also contain the χ^2 values of the Monte Carlo as compared with the flasher data. When consulting these values for both the horizontal and vertical tilt it is difficult to see any pattern which would indicate that tilting the LEDs consistently improved the agreement between flasher data and Monte Carlo simulations. The only possible improvement occurred on DOM 55 with the negative tilt when receiving directly across from the source. Here improvement is seen in the χ^2, skewness, kurtosis, and mean values for both ice models.

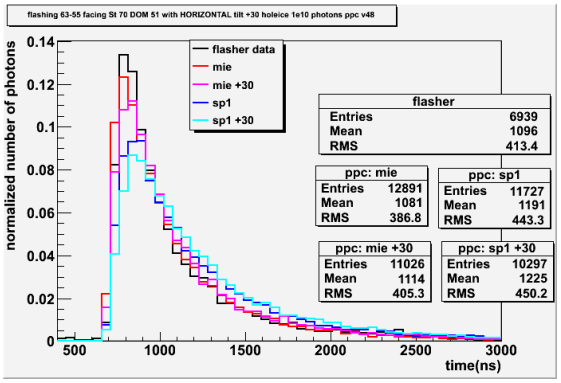

(a) String 63 DOM 55 flashing towards String 70 DOM 51 with a horizontal tilt of +30

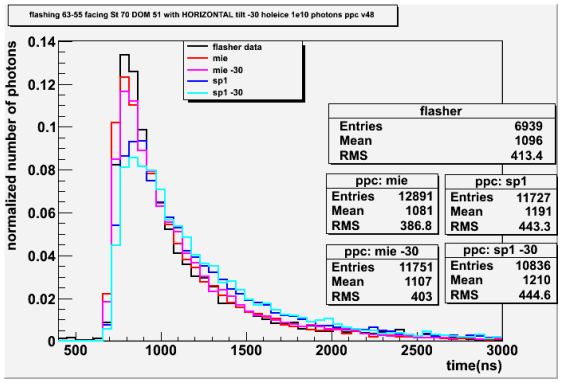

(b) String 63 DOM 55 flashing towards String 70 DOM 51 with a horizontal tilt of -30

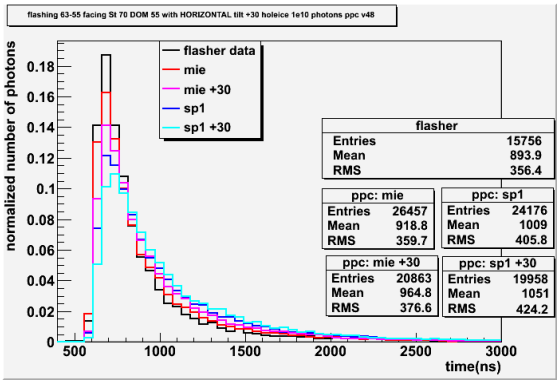

(c) String 63 DOM 55 flashing towards String 70 DOM 55 with a horizontal tilt of +30

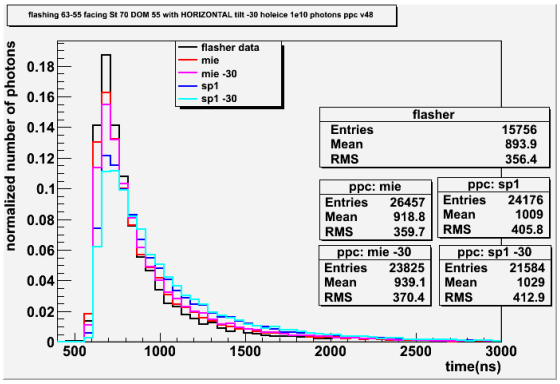

(d) String 63 DOM 55 flashing towards String 70 DOM 55 with a horizontal tilt of -30

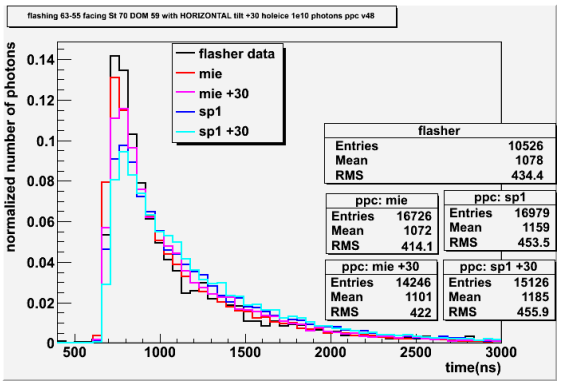

(e) String 63 DOM 55 flashing towards String 70 DOM 59 with a horizontal tilt of +30

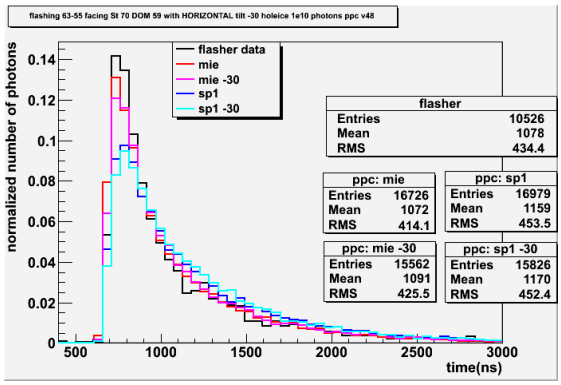

(f) String 63 DOM 55 flashing towards String 70 DOM 59 with a horizontal tilt of -30

Figure 8.3: String 63 DOM 55 flashing towards String 70 DOM 55 with a horizontal tilt of 30 degrees.

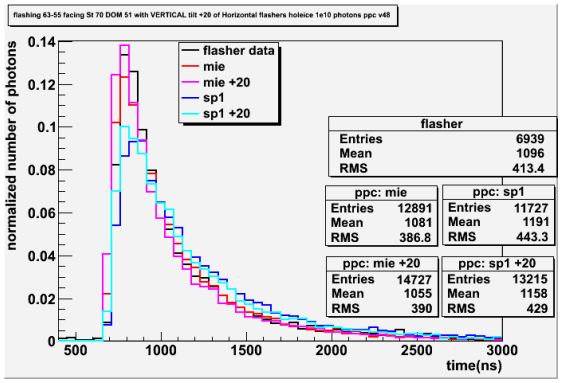

(a) String 63 DOM 55 flashing towards String 70 DOM 51 with a vertical tilt of +20

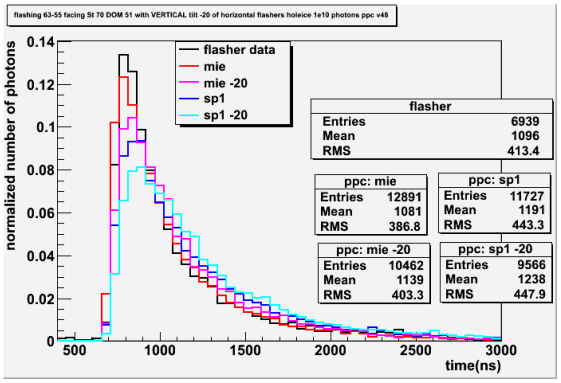

(b) String 63 DOM 55 flashing towards String 70 DOM 51 with a vertical tilt of -20

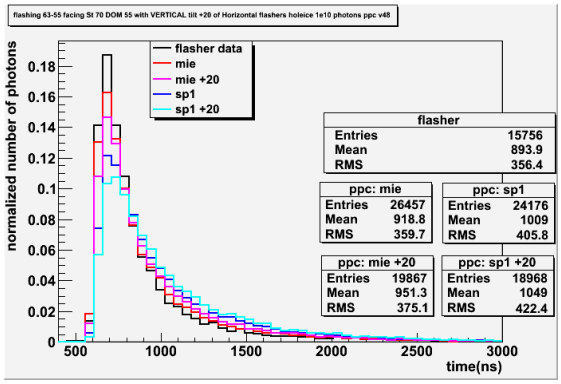

(c) String 63 DOM 55 flashing towards String 70 DOM 55 with a vertical tilt of +20

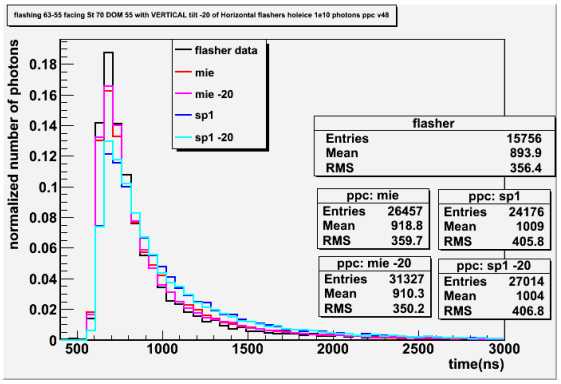

(d) String 63 DOM 55 flashing towards String 70 DOM 55 with a vertical tilt of -20

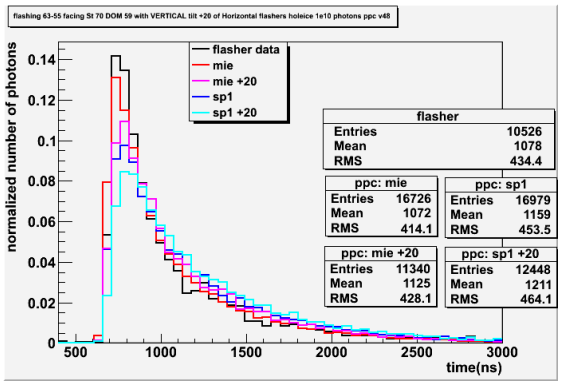

(e) String 63 DOM 55 flashing towards String 70 DOM 59 with a vertical tilt of +20

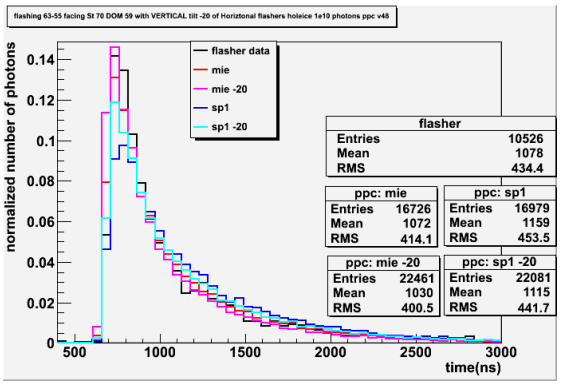

(f) String 63 DOM 55 flashing towards String 70 DOM 59 with a vertical tilt of -20

Figure 8.4: String 63 DOM 55 flashing towards String 70 DOM 55 with a vertical tilt of 20 degrees.

Table 8.5: DOM 55 horizontal tilt

	Positive tilt				Negative tilt			
ice model	χ^2	skewness	kurtosis	mean	χ^2	skewness	kurtosis	mean
Four DOMs above								
Data	–	1.91	3.7	1096	–	1.91	3.7	1096
Mie	3.9	1.92	4.12	1081	3.9	1.92	4.12	1081
Mie Tilt	3.15	1.83	3.52	1114	3.29	1.85	3.69	1107
Sp1	7.84	1.59	2.42	1191	7.84	1.59	2.42	1191
Sp1 Tilt	12.42	1.46	1.88	1225	10.64	1.51	2.16	1210
Directly across								
Data	–	2.68	8.38	894	–	2.68	8.38	894
Mie	4.94	2.34	6.55	919	4.94	2.34	6.55	919
Mie Tilt	15.11	2.1	5.13	965	7.36	2.24	5.87	939
Sp1	30.67	1.9	3.94	1009	30.67	1.9	3.94	1009
Sp1 Tilt	50.0	1.81	3.5	1051	40.74	1.85	3.67	1029
Four DOMs below								
Data	–	1.84	3.36	1078	–	1.84	3.36	1078
Mie	4.67	1.75	3.16	1072	4.67	1.75	3.16	1072
Mie Tilt	4.61	1.69	2.91	1101	3.64	1.73	2.95	1091
Sp1	9.73	1.48	1.94	1159	9.73	1.48	1.94	1159
Sp1 Tilt	14.72	1.43	1.84	1185	12.18	1.49	2.04	1170

Table 8.6: DOM 55 Vertical tilt

	Positive tilt				Negative tilt			
ice model	χ^2	skewness	kurtosis	mean	χ^2	skewness	kurtosis	mean
Four DOMs above								
Data	–	1.91	3.7	1096	–	1.91	3.7	1096
Mie	3.9	1.92	4.12	1081	3.9	1.92	4.12	1081
Mie Tilt	6.68	1.99	4.39	1055	4.76	1.73	3.19	1139
Sp1	7.84	1.59	2.42	1191	7.84	1.59	2.42	1191
Sp1 Tilt	5.74	1.62	2.61	1158	15.96	1.47	1.98	1238
Directly across								
Data	–	2.68	8.38	894	–	2.68	8.38	894
Mie	4.94	2.34	6.55	919	4.94	2.34	6.55	919
Mie Tilt	9.63	2.15	5.38	951	4.21	2.35	6.57	910
Sp1	30.67	1.9	3.94	1009	30.67	1.9	3.94	1009
Sp1 Tilt	45.71	1.76	3.21	1049	29.14	1.94	4.12	1004
Four DOMs below								
Data	–	1.84	3.36	1078	–	1.84	3.36	1078
Mie	4.67	1.75	3.16	1072	4.67	1.75	3.16	1072
Mie Tilt	6.14	1.57	2.35	1125	6.14	1.57	2.35	1125
Sp1	9.73	1.48	1.94	1159	9.73	1.48	1.94	1159
Sp1 Tilt	18.99	1.36	1.51	1211	18.99	1.36	1.51	1211

Consulting all methods of comparisons, there are only a handful of scenarios where the tilt possibly improves the fit. More of these occurred for DOM 23; however, there were not enough data points to draw conclusions. To further investigate the tilting angle of the LEDs a better systematic study is needed. This would involve studying more angles of the LED. Furthermore, it was difficult to evaluate if the correct LED positioning had been overshot or was correctly placed with only the extreme angles being used. More depths could also be included. While no conclusive corrections can be made on the correct angle, an idea of the error of which could be attributed to the incorrect knowledge of the LED angle can be used. The χ^2 results give an idea of how much changing the LED by extreme scenarios can increase or decrease the correlation between Monte Carlo and flasher data.

Chapter 9

Closing remarks

9.1 Further work

While this research has built upon previous studies, there is still room for further analysis. For example the 15 depths studied could be extended to all 60 depths. To study horizontal variation, flasher data on different strings could be simulated. There was recently a new set of flasher data taken in January 2011 with comparable SPE settings [58]. Beyond the single LED SPE data, MPE data could be studied.

Within the simulations, the number of photons could be adjusted so that error bars were more uniform, especially for the orientation with the emitter pointed away from the receiver. A wider range of receivers could be used such as two, four, or six DOMs from the source.

It would be interesting to investigate further the effect of the scattering angle function versus the values of the absorption and scattering coefficients used. This could be performed for example by using the ice properties of Spice 1 with the HG-SL scattering function used by Spice Mie. Or a range of bulk ice models with different scattering functions could be used and the skewness and kurtosis values used to quantify the shape of the reuslting time distributions. The literature could be reviewed further to see if another scattering function all together, may better suit the scattering in the ice.

A glaring outstanding question is the reason behing the time offset in the arrival time of the first photons for the Spice Mie distributions compared with the data. A first step would be to investigate the actual offset between the earliest photons rather than the offset which produced the best χ^2 value. This study should be done with time distributions for all of the models and at all depths. Obviously if the offset is found to be independent of depth and ice model then the origin will not be in the actual scattering parameters chosen. If this is not the case, then further investigation could include adjusting the scattering of Spice Mie to see if it is possible to keep both the shape of the distribution, and arrival times

of the earliest photons, matching well. It would also be useful to repeat these studies using Photonics to see if there are any differences compared with PPC.

9.2 Conclusion

Time distributions for different orientations of emitter-receiver pairs in the IceCube neutrino observatory show that the ice properties of absorption and scattering are best described by ice model Spice Mie. This was further solidified by incorporating the shift of the time distributions to achieve the lowest possible χ^2. Considering this factor greatly improves the χ^2 values for Spice Mie and less so for Spice 1 and AHA. The minimal positive time shift required for Spice Mie's fit infers that the shape of the time distribution is accurate. However there are a few depths where Spice 1 and AHA provide the best fit, with and without the time shift.

Throughout the study, Spice 1 is strongly coupled with AHA across all statistical measurements. While Spice 1 and AHA have different absorption and scattering properties, they both calculate the scattering angle based on the same equation: the Henyey-Greenstein function. The ice properties of Spice Mie and Spice 1 are not vastly different. One possibility for the close relationship between Spice 1 and AHA could be that the scattering functions may be heavily influencing the ice models. For Spice Mie this was a combination of the Henyey-Greenstein function and the Simplified Liu function. The longer scattering length of Spice Mie may also be the cause for the drastic improvement.

The variation in results for emitter-receiver pairs pointed towards each other or away from each other shows the effects of scattering. When the emitter was facing the receiver, differences in the DOMs four above or below the source could be noticed. These features were not distinguishable when the emitter was pointed away from the receiver because there were no direct hit photons.

The complex dynamics of the ice properties are well on their way to being understood. This study investigated the different effects of absorption and scattering properties, orientation of emitter-receiver pairs and angle of LEDs flashed. From these efforts it was concluded that while not perfect, Spice Mie provides the best fit for the time distributions of flasher data and Monte Carlo data.

Chapter 10

Acknowledgements

It has been a whirlwind year writing this thesis and it could not have been done without the help of many, a few to be mentioned here. Firstly, thank you to my supervisor, Dr. Jenni Adams and co-supervisors, Dr. Andreas Gross, Dr. Anthony Brown and Dr. Suruj Seunarine. Everyone has been very patient and explained complicated physics in an easy to understand manner. It was such a pleasure working with the IceCube Collaboration and attending the Collaboration meeting. Thank you to the IceCube collaboration for all the support and help. Seeing science in action makes all the effort seem worthwhile. It has also been nice getting to know collaborators as real people and not super human physics nerds.

Thank you to everyone at Canterbury University especially Rhondda, Rosalie and Xuefung. It is true, physicists can not deal with paper work very well. Thank you to all the cleaning crew who kept the area around my desk clean even if my desk was a construction site. As for my office mates, I can honestly say coming in to uni would have sucked with out you all - James, Giles, Steph, Ashan, Will, Hamish and let's not forget Kahae, Joe and Bart. Through the distractions and late nights, it has been a pleasure. I know the office will not be the same without me - you will actually be able to get some work done now. But alas, who will bring you baking and kill all the plants? Thanks to all the other students in the physics dept who have been good friends. Thanks to Kath and Timmy for visiting in my office and helping me edit this monstrosity.

Thank you more than there are neutrinos passing through your body every second, to my family. It is very easy to think that χ^2 tests and error bars are the soul reason for one's existence but thank God my family was there to drag me out of my warped reality. Saturday mornings at yoga with my Uncle Mark and Grandma drugging her cooking with sleeping powder made for the ultimate nana-naps. Thank you for always being there for me whether its to listen to me complain about my plots or to let me not think about physics (consciously) for a day. Thank you's are also owed to Robin, Bill, Ann,

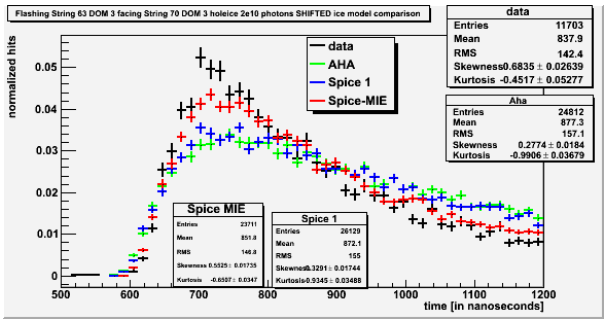

(a) facing across 2e10 photons - χ^2AHA= 13.67, Spice 1 = 11.425, Spice Mie = 2.817

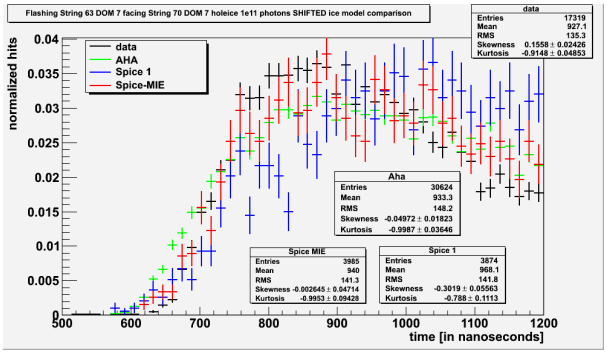

(b) facing across 1e11 photons - χ^2AHA= 8.18, Spice 1 = 5.71, Spice Mie = 1.91

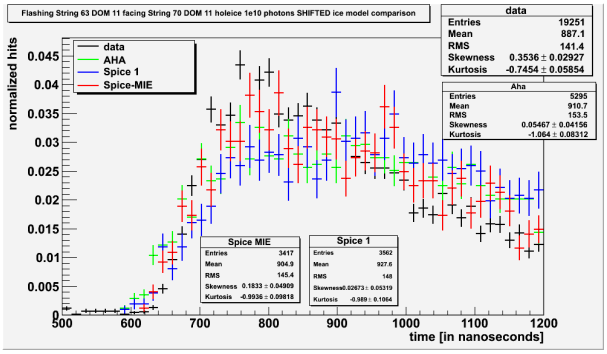

(c) facing across 1e10 photons - χ^2AHA= 5.53, Spice 1 = 4.42, Spice Mie = 2.33

Figure 10.1: Flasher data and icemodel comparison flashing String 63 facing String 70 receiving directly across χ^2

Kevin, Leela, Flynn, Steven, Om, Pat, Scott, Culumn, Cameron, and KerriAnn. Weekends at the farm with home grown veggies after a day playing with the cows will never be forgotten. How good was it to sit by the fire and read about Antarctic explorers or a romance novel after uni exams? A shout out to Auckland for Ngaral, Terry, Kimberly and Lara, Thank you for always letting me stay. I hope I can once day repay you for those early morning airport runs. Thank you family, this thesis has been a really good excuse to spend so much time with you all, I try not to forget my real reasons for being here.

For you mum, I am sorry that I kept you awake all the time while you were trying to write your

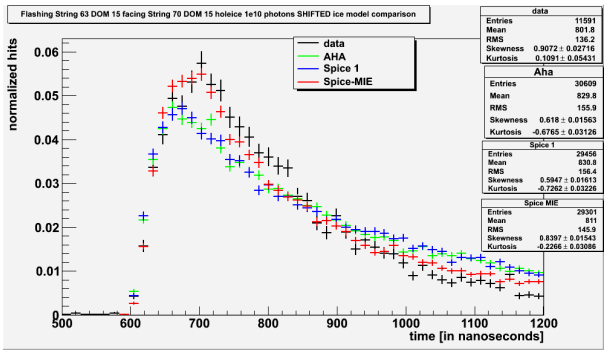

(a) facing across 1e10 photons - χ^2AHA= 8.73, Spice 1 = 9.38, Spice Mie = 3.11

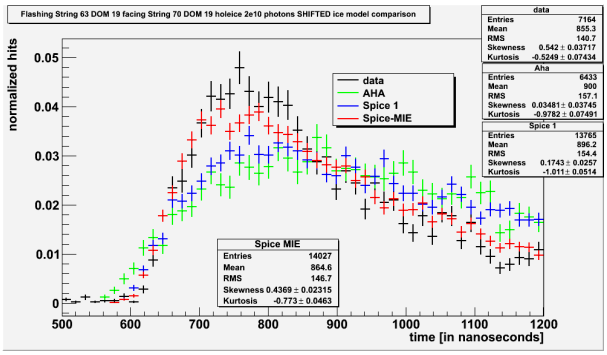

(b) facing across 2e10 photons - χ^2AHA= 8.408, Spice 1 = 7.27, Spice Mie = 2.49

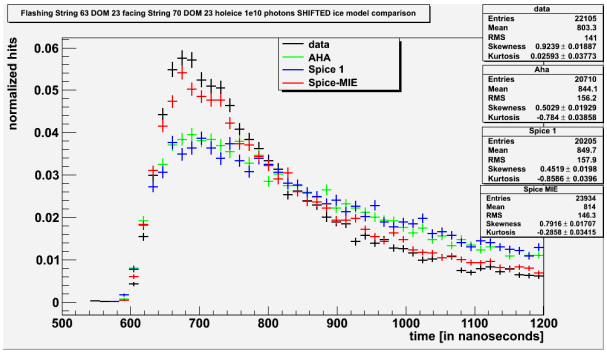

(c) facing across 1e10 photons - χ^2AHA= 17.8, Spice 1 = 21.453, Spice Mie = 2.88

Figure 10.2: Flasher data and icemodel comparison flashing String 63 facing String 70 receiving directly across χ^2

thesis. Now I know how incredible it was that you wrote your thesis using a only a typewriter complete with a screaming baby by your desk. Miles, if I had the writing skills you have in your left pinky finger, this thesis would have come out 10,000 times better. To all my family in America, I am sorry for being away, assuming you are not all rejoicing at the fact that I'm not there to bother you.

Thank you to my friends all over the globe. You have all provided a great support network to which I am deeply in indented to. Thank you to my flatmates who put up with me coming home muttering over

something about physics and consulting the ice cream tub or baking cookies at midnight to de-stress.

Thank you to the tramping club for at least coaxing me out of the physics building on Wednesday nights. It was only through walking till pure exhaustion took over that I was able to spend the rest of the week sitting behind a computer staring out at the mountains.

Kieran if you thought the madness would end when I handed in my thesis you've got another thing coming. Thanks for the perspective and cooking me shakshuka.

Finally to everyone - I do not know if this thesis will make me a better person or if my 'contributions to science' are only a mirage to make it seem like all the sacrifices are worth while. I hope it is not all in vain for I do not think I will feel any different on March 1st, 2011. All the same, thank you for letting me have this opportunity to prove myself and finish my degree. I hope that I will go on and do something useful with my life so that not all will be lost and we can all look back at this paperweight of a thesis and it is something to be proud about.

Appendix A

The number of hits as a function of depth and ice model

The below sections discuss the number of hits received in relation to the depth and the icemodel. The focus is on the same number of number of photons simulated. Firstly, the emitter facing the reciever is reviewed and then the emitter pointed away from the receiver.

A.1 Number of photons detected with the emitter facing receivers

Initially when 1×10^{10} photons were simulated at each depth, the number of photons received increased with depth for all emitter-receiver pairs, as shown in Table A.1 to Table A.3. The left side of the table shows the depths with the same number of photons simulated.

Under constant simulation values, while the number of photons received depended on the ice model, the change in photon count with depth was larger than the variation between each ice model. The results for ice model AHA varied less than Spice Mie or Spice 1. As expected, the lower variation rate can be explained by the method to determine the ice properties. Furthermore, the number of photons received for Spice Mie and Spice 1 vary by similar amounts because they were created by similar methods. As discussed in Section 4.5 for a discussion on the ice model creation processes. See Figures 4.2 and 4.1 for the plots of absorption and scattering properties implimented in AHA showing how they are less extreme than the Spice models.

The photon count varied between the DOMs receiving above, across and below from the emitter. Photon count on the four DOMs receiving above and across from the source varied by a factor of

100,000 from smallest to largest. Receiving on four DOMs below, the range was restricted to a factor of 25,000. DOMs receiving below had the most 'stable' range across all ice models at all depths. The design of the DOMs could explain this phenomena. The PMTs are located on the bottom of the DOMs meaning the photons have to scatter to reach the DOM, eliminating any direct hit photons.

For the flasher data the number of photons emitted was adjusted to maintain a brightness of 0.1 occupancy for consistent values on the number of hits received across all depths [57]. Thus in areas of less absorption or scattering, the number of photons emitted from the LEDs was decreased. In dustier regions, the LED brightness was increased. The Monte Carlo simulations were not allowed this degree of freedom for this study, so in dustier regions they have a lower photon count than the flasher data.

Table A.1: Comparison of flasher data and Monte Carlo simulations of thie number of hits received on String 70 directly across from the source with the LED pointed towards the receiving string. The left of the table presents the same number of number of photons simulated to show the changes in the number of hits received with depth. The right half of the table displays the results when the number of photons simulated was adjusted so the received hits are within a factor of three.

DOM number	Data (hits)	Simulated photons	AHA (hits)	Spice 1 (hits)	Spice Mie (hits)	Adjusted photons	AHA (hits)	Spice 1 (hits)	Spice Mie (hits)
3	12,000	1×10^{10}	12,000	13,000	12,000	2×10^{10}	24,000	25,000	24,000
7	17,000	1×10^{10}	3,000	0	0	1×10^{11}	32,000	4,000	4,0000
11	19000	1×10^{10}	5,000	4,000	3,000				
15	12,000	1×10^{10}	28,000	27,000	29,000				
19	7,000	1×10^{10}	3,000	7,000	7,000	2×10^{10}	6,000	14,000	14,000
23	22,000	1×10^{10}	20,000	20,000	24,000				
27	14,000	1×10^{10}	12,000	24,000	27,000				
31	18,000	1×10^{10}	11,000	3,000	4,000	22×10^{9}	25,000	7,000	8,000
34	17,000	1×10^{10}	0	0	0	6×10^{11}	6,000	0	0
39	13,000	1×10^{10}	31,000	21,000	42,000	5×10^{9}	15,000	11,000	21,000
43	11,000	1×10^{10}	14,000	15,000	17,000				
47	23,000	1×10^{10}	34,000	48,000	52,000	5×10^{9}	17,000	24,000	26,000
51	13,000	1×10^{10}	33,000	97,000	104,000	25×10^{8}	8,000	24,000	26,000
55	16,000	1×10^{10}	49,000	24,000	27,000	5×10^{9}	24,000	12,000	13,000
59	17,000	1×10^{10}	32,000	102,000	102,000	25×10^{8}	8,000	26,000	25,000

Table A.2: Comparison of flasher data and Monte Carlo simulations by the number of hits received on String 70 four DOMs above the source with the LED pointed towards the receiving string. The left of the table presents the same number of number of photons simulated, 1×10^{10} to show the changes in the number of hits received with depth. The right half of the table displays the results when the number of photons simulated was adjusted so the received hits are within a factor of three.

DOM number	Data (hits)	Simulated photons	AHA (hits)	Spice 1 (hits)	Spice Mie (hits)	Adjusted photons	AHA (hits)	Spice 1 (hits)	Spice Mie (hits)
3	Not	applicable							
7	30,000	4,000	1,000	1,000	11×10^{10}	12,000	4,000	4,000	
11	5,000	1,000	0	0	15×10^{10}	16,000	5,000	5,000	
15	4,000	8,000	9,000	9,000					
19	5,000	2,000	2,000	2,000	2×10^{10}	4,000	4,000	5,000	
23	8,000	5,000	9,000	10,000					
27	4,000	3,000	5,000	6,000	3×10^{10}	10,000	14,000	17,000	
31	26,000	8,000	7,000	7,000					
34	Dust	layer							
39	Dust	layer							
43	10,000	11,000	13,000	16,000					
47	5,000	9,000	11,000	13,000					
51	10,000	25,000	49,000	51,000	0.25×10^{10}	6,000	12,000	13,000	
55	7,000	12,000	12,000	13,000					
59	7,000	26,000	38,000	42,000	0.25×10^{10}	6,000	10,000	10,000	

Table A.3: Comparison of flasher data and Monte Carlo simulations by the number of hits received on String 70 four DOMs below the source with the LED pointed towards the receiving string. The left of the table presents the same number of number of photons simulated to show the changes in the number of hits received with depth. The right half of the table displays the results when the number of photons simulated was adjusted so the received hits are within a factor of three.

DOM number	Data (hits)	Simulated photons	AHA (hits)	Spice 1 (hits)	Spice Mie (hits)	Adjusted photons	AHA (hits)	Spice 1 (hits)	Spice Mie (hits)
3	3,000	1×10^{10}	5,000	2,000	2,000	4×10^{10}	9,000	4,000	4,000
7	11000	1×10^{10}	1,000	0	0	2×10^{11}	15,000	5,000	5,000
11	23,000	1×10^{10}	4,000	5,000	4,000				
15	2,000	1×10^{10}	3,000	3,000	3,000	4×10^{10}	11,000	10,000	11,000
19	7,000	1×10^{10}	3,000	6,000	5,000	2×10^{10}	6,000	12,000	11,000
23	5,000	1×10^{10}	3,000	3,000	4,000	25×10^{9}	8,000	9,000	9,000
27	5,000	1×10^{10}	7,000	9,000	9,000				
31	Dust	layer							
34	Dust	layer							
39	4,000	1×10^{10}	11,000	11,000	13,000	5×10^{9}	6,000	6,000	7,000
43	6,000	1×10^{10}	5,000	5,000	6,000				
47	8,000	1×10^{10}	17,000	24,000	23,000				
51	3,000	1×10^{10}	7,000	13,000	14,000				
55	11,000	1×10^{10}	21,000	17,000	17,000				
59	Not	applicable							

A.2 Number of photons received with the emitter pointer pointed away from the receivers

As Table A.4 to Table A.6 show, at first 1×10^{10} photons were simulated but as this produced photons counts with low statistics, the number of photons simulated was increased to 1×10^{11}. The increase in photon simulation number caused for a greater range of photons received. With out the individualized simulation amount across each depth, the number received varied up to a factor of 77.

With 1×10^{10} photons simulated, the variation between depths was minimal under all receiver settings. It is not till the last three depths studied, when the emitter was across from the receiver, that the range in photon count becomes larger than the range seen at shallower depths. Furthermore, the photon count levels of Spice 1 and Spice Mie were not obviously connected.

When the number of photons simulated was increased by a factor of 10, there was more variation apparent in the number of photons received. Still there was no noticeable relationship between ice models, and the change in photon count range only increased at the last few DOMs when receiving directly across.

Unlike the Monte Carlo results, the flasher data showed a strong correlation by eye with the absorption and scattering parameters of Figure 4.1 and Figure 4.2. Particularly with receivers four DOMs from the source, the variation in photons received was greater, increasing relative to regions of more absorption and scattering. Receivers directly across from the flasher data showed the most consistent results of the different settings, save DOM 34 at the dust layer. The occupancy was again set to 0.1 for all flasher data runs.

Overall, when the emitter is pointed away from the receiver, the relationship between the number of photons received when a constant number of photon are emitted, is not closely related to the absorption and scattering properties. This is especially apparent when receiving directly across from the emitter. The higher levels of scattering required for photons to be deflected around must smear the variations in absorption and scattering properties. A few peaks in the number of photons received can be seen above or below from the source when there are regions of higher absorption. This is logical because with more dust, more photons are deflected and scattered back to be received on the string further away.

Table A.4: Comparison of flasher data and Monte Carlo simulations by the number of hits received on string 70 directly across from the source with the LED pointed away from the receiving string. The left of the table presents the same number of photons simulated to show the changes in the number of hits received with depth. The right half of the table displays the results when the number of photons simulated was adjusted so the received hits are within a factor of three.

DOM number	Data (hits)	Simulated photons	AHA (hits)	Spice 1 (hits)	Spice Mie (hits)	Adjusted photons	AHA (hits)	Spice 1 (hits)	Spice Mie (hits)
3	17,000	1×10^{10}	2,000	2,000	1,000	1×10^{11}	30,000	26,000	20,000
7	20,000	1×10^{10}	1,000	0	0	1×10^{11}	15,000	2,000	2,000
11	19,000	1×10^{10}	1,000	1,000	1,000	1×10^{11}	17,000	14,000	11,000
15	22,000	1×10^{10}	2,000	3,000	2,000	1×10^{11}	43,000	45,000	32,000
19	15,000	1×10^{10}	1,000	1,000	1,000	1×10^{11}	12,000	23,000	17,000
23	18,000	1×10^{10}	2,000	3,000	2,000	1×10^{11}	38,000	45,000	31,000
27	18,000	1×10^{10}	2,000	3,000	2,000	1×10^{11}	30,000	49,000	35,000
31	22,000	1×10^{10}	2,000	1,000	1,000	1×10^{11}	35,000	18,000	14,000
34	4,000	1×10^{10}	0	0	0	1×10^{11}	3,000	0	0
39	15,000	1×10^{10}	3,000	3,000	2,000	1×10^{11}	43,000	41,000	32,000
43	16,000	1×10^{10}	3,000	3,000	2,000	1×10^{11}	45,000	44,000	32,000
47	19,000	1×10^{10}	4,000	5,000	3,000	1×10^{11}	64,000	38,000	53,000
51	17,000	1×10^{10}	3,000	5,000	4,000	1×10^{11}	55,000	87,000	59,000
55	16,000	1×10^{10}	5,000	4,000	3,000	1×10^{11}	77,000	62,000	52,000
59	20,000	1×10^{10}	4,000	6,000	4,000	1×10^{11}	67,000	96,000	65,000

Table A.5: Comparison of flasher data and Monte Carlo simulations by the number of hits received on string 70 four DOMs above the source with the LED pointed away from the receiving string. The left of the table presents the same number of number of photons simulated to show the changes in the number of hits received with depth. The right half of the table displays the results when the number of photons simulated was adjusted so the received hits are within a factor of three.

DOM number	Data (hits)	Simulated photons	AHA (hits)	Spice 1 (hits)	Spice Mie (hits)	Adjusted photons	AHA (hits)	Spice 1 (hits)	Spice Mie (hits)
3	Not	applicable							
7	49,000	1×10^{10}	2,000	1,000	0	1×10^{11}	22,000	9,000	1,000
11	4,000	1×10^{10}	0	0	0	1×10^{11}	4,000	1,000	1,000
15	7,000	1×10^{10}	1,000	1,000	1,000	1×10^{11}	14,000	17,000	12,000
19	11,000	1×10^{10}	1,000	1,000	0	1×10^{11}	10,000	9,000	8,000
23	8,000	1×10^{10}	1,000	1,000	1,000	1×10^{11}	12,000	24,000	16,000
27	7,000	1×10^{10}	1,000	1,000	1,000	1×10^{11}	13,000	13,000	10,000
31	48,000	1×10^{10}	2,000	3,000	2,000	1×10^{11}	30,0000	41,000	33,000
34	Dust	layer							
39	Dust	layer							
43	15,000	1×10^{10}	2,000	3,000	2,000	1×10^{11}	41,000	43,000	35,000
47	5,000	1×10^{10}	1,000	1,000	1,000	1×10^{11}	21,000	10,000	16,000
51	17,000	1×10^{10}	3,000	4,000	3,000	1×10^{11}	55,000	65,000	46,000
55	10,000	1×10^{10}	2,000	3,000	3,000	1×10^{11}	25,000	45,000	41,000
59	10,000	1×10^{10}	4,000	3,000	2,000	1×10^{11}	70,000	49,000	37,000

Table A.6: Comparison of flasher data and Monte Carlo simulations by the number of hits received on string 70 four DOMs below the source with the LED pointed away from the receiving string. The left of the table presents the same number of number of photons simulated to show the changes in the number of hits received with depth. The right half of the table displays the results when the number of photons simulated was adjusted so the received hits are within a factor of three.

DOM number	Data (hits)	Simulated photons	AHA (hits)	Spice 1 (hits)	Spice Mie (hits)	Adjusted photons	AHA (hits)	Spice 1 (hits)	Spice Mie (hits)
3	4,000	1×10^{10}	1,000	0	0	1×10^{11}	30,000	26,000	20,000
7	15,000	1×10^{10}	0	0	0	1×10^{11}	4,000	2,000	1,000
11	35,000	1×10^{10}	1,000	2,000	1,000	1×10^{11}	20,000	25,000	20,000
15	3,000	1×10^{10}	0	0	0	1×10^{11}	5,000	5,000	4,000
19	18,000	1×10^{10}	1,000	2,000	1,000	1×10^{11}	16,000	25,000	19,000
23	7,000	1×10^{10}	1000	1,000	1,000	1×10^{11}	9,000	12,000	9,000
27	6,000	1×10^{10}	1,000	1,000	1,000	1×10^{11}	23,000	21,000	14,000
31	Dust	layer							
34	Dust	layer							
39	9,000	1×10^{10}	2,000	2,000	1,000	1×10^{11}	25,000	30,000	19,000
43	14,000	1×10^{10}	2,000	2,000	1,000	1×10^{11}	25,000	26,000	20,000
47	11,000	1×10^{10}	3,000	4,000	3,000	1×10^{11}	45,000	35,000	51,000
51	6,000	1×10^{10}	2,000	1,000	1,000	1×10^{11}	24,000	20,000	16,000
55	20,000	1×10^{10}	3,000	5,000	4,000	1×10^{11}	47,000	70,000	59,000
59	Not	applicable							

Appendix B

PPC specifics

All of these instructions are specific to Version 48 of PPC. In using a different version, comands may vary.

B.1 Absorption and scattering properties found in PPC

The absorption and scattering properties of each ice model at a depth of (x, y) can be found in PPC via the command WFLA=[λ] ./ppc − [x] [y]. Specifing WFLA will indicate which wavelength desiered. The output gives the depth in IceCube coordinates with respect to the origin, this can be convered to real time depth by subtracting it from 1948.07. The other outputs are the absorption coefficient and geometric scattering coefficient [52].

B.2 How to run PPC and specify and LED direction

The simulated LED angles were specified before the code commenced by inserting the desired angle in the variable command of FLDR=angle number like so :

FLDR=[angle number] ./ppc [String number] [DOM number] [number of photons simulated].

An example simulation for String 63 DOM 7 with 1×10^{10} photons facing the receiving string would be:

FLDR= 137 ./ppc 63 7 $1e10$.

B.3 Changing the angular acceptance

In order to implement the holeice, copy as.holeice into as.dat. All simulations were done with the holeice setting.

B.4 Oversizing of DOMs

To change the DOM oversize factor, edit line two of the file cfg.txt. A DOM oversize of five was maintained as the default settings for all simulations done in this study.

B.5 Tilt of the ice

To change the tilt of the ice, edit line five of the file ini.cxx: #define TILT. The tilting command was disabled for both AHA and Spice 1 simulations and enabled for Spice Mie simulations. The tilting file implements tilt.dat and tilt.par which considers that the ice layers are not completely horizontal and over large periods show some vertical variation CITE.

B.6 Tilting the flashers

To change the horizontal tilt of the LEDs, the angle implemented in ppc was adjusted accordingly. The angle of the LED most directly orientated towards the receiving string was found in the table provided by C. Wendt displayed in Appendix C.

Vertically changing the LED angle involved editing the pro.cu code before running ppc. The code was originally as shown below:

Beginning at line 251 of pro.cu :

switch(e.type)

$case1 : rms = 9.2f; up = 0.0f; hms = 10.1f; break;$

$case2 : rms = 9.7f; up = 48.f; hms = 14.7f; break; //sin(hms/2) = sin(9.8/2)/cos(up)$

$case3 : rms = 0.0f; up = 90.0f - 41.13f; break;$

$case4 : rms = 0.0f; up = 41.13f - 90.0f; break;$

This has to be changed to tilt the horizontal flashers by editing as such for an upward tilt:

switch(e.type)

$case1 : rms = 9.2f; up = 20.0f; hms = 10.1f; break;$

$case2 : rms = 9.7f; up = 48.f; hms = 14.7f; break; //sin(hms/2) = sin(9.8/2)/cos(up)$

$case3 : rms = 0.0f; up = 90.0f - 41.13f; break;$

$case4 : rms = 0.0f; up = 41.13f - 90.0f; break;$

or such for a downward tilt:

switch(e.type)

$case1 : rms = 9.2f; up = -20.0f; hms = 10.1f; break;$

$case2 : rms = 9.7f; up = 48.f; hms = 14.7f; break; //sin(hms/2) = sin(9.8/2)/cos(up)$

$case3 : rms = 0.0f; up = 90.0f - 41.13f; break;$

$case4 : rms = 0.0f; up = 41.13f - 90.0f; break;$

Appendix C

Table of LED angles

Contact Chris Wendt for more information.

Table C.1: LED angles string 63 flashers - part 1

string	dom	LED7	$string_{target}$	LED_{face}	LED_{fangle}	LED_{behind}	LED_{bangle}
63	1	273	70	9	153	12	333
63	2	61	70	12	121	9	301
63	3	177	70	8	117	11	297
63	4	137	70	7	137	10	317
63	5	3	70	11	123	8	303
63	6	62	70	12	122	9	302
63	7	157	70	7	157	10	337
63	8	157	70	7	157	10	337
63	9	77	70	12	137	9	317
63	10	53	70	12	113	9	293
63	11	353	70	11	113	8	293
63	12	208	70	8	148	11	328
63	13	278	70	9	158	12	338
63	14	297	70	10	117	7	297
63	15	190	70	8	130	11	310
63	16	206	70	8	146	11	326
63	17	53	70	12	113	9	293
63	18	48	70	12	108	9	288
63	19	238	70	9	118	12	298
63	20	230	70	9	110	12	290

Table C.2: LED angles string 63 flashers - part 2

string	dom	LED7	$string_{target}$	LED_{face}	LED_{fangle}	LED_{behind}	LED_{bangle}
63	21	127	70	7	127	10	307
63	22	143	70	7	143	10	323
63	23	26	70	11	146	8	326
63	24	43	70	12	103	9	283
63	25	296	70	10	116	7	296
63	26	300	70	10	120	7	300
63	27	309	70	10	129	7	309
63	28	9	70	11	129	8	309
63	29	138	70	7	138	10	318
63	30	249	70	9	129	12	309
63	31	164	70	8	104	11	284
63	32	322	70	10	142	7	322
63	33	184	70	8	124	11	304
63	34	248	70	9	128	12	308
63	37	69	70	12	129	9	309
63	38	107	70	7	107	10	287
63	39	359	70	11	119	8	299
63	40	339	70	11	99	8	279
63	41	169	70	8	109	11	289
63	42	240	70	9	120	12	300
63	43	54	70	12	114	9	294
63	44	82	70	12	142	9	322
63	45	242	70	9	122	12	302
63	46	20	70	11	140	8	320
63	47	254	70	9	134	12	314
63	48	338	70	10	158	7	338
63	49	138	70	7	138	10	318
63	50	201	70	8	141	11	321
63	51	119	70	7	119	10	299
63	52	120	70	7	120	10	300
63	53	90	70	12	150	9	330
63	54	47	70	12	107	9	287
63	55	193	70	8	133	11	313
63	56	306	70	10	126	7	306
63	57	317	70	10	137	7	317
63	58	266	70	9	146	12	326
63	59	321	70	10	141	7	321
63	60	139	70	7	139	10	319

Appendix D

One-LED SPE data

D.1 Run 114661 - Even DOMs

Location: http://warehouse.icecube.wisc.edu/data/exp/IceCube/2009/calibration/SouthPole/1013/

```
run=114661 and subrun=1;
+-------+--------+--------+------------+--------------+------------+--------+-------+------+------+
| id    | run    | subrun | string_hub | dom_position | brightness | window | delay | mask | rate |
+-------+--------+--------+------------+--------------+------------+--------+-------+------+------+
| 29219 | 114661 |      1 |         63 |            2 |         17 |     20 |     0 | 0800 |  300 |
| 29220 | 114661 |      1 |         63 |            8 |         11 |     25 |     0 | 0040 |  300 |
| 29221 | 114661 |      1 |         63 |           14 |          4 |     25 |     0 | 0200 |  300 |
| 29222 | 114661 |      1 |         63 |           20 |         17 |     20 |     0 | 0100 |  300 |
| 29223 | 114661 |      1 |         63 |           26 |         17 |     20 |     0 | 0200 |  300 |
| 29224 | 114661 |      1 |         63 |           32 |         24 |     20 |     0 | 0200 |  300 |
| 29225 | 114661 |      1 |         63 |           38 |         30 |     20 |     0 | 0040 |  300 |
| 29226 | 114661 |      1 |         63 |           44 |         23 |     20 |     0 | 0800 |  300 |
| 29227 | 114661 |      1 |         63 |           50 |          9 |     24 |     0 | 0080 |  300 |
| 29228 | 114661 |      1 |         63 |           56 |         19 |     25 |     0 | 0200 |  300 |
+-------+--------+--------+------------+--------------+------------+--------+-------+------+------+
10 rows in set (0.01 sec)

run=114661 and subrun=2;
+-------+--------+--------+------------+--------------+------------+--------+-------+------+-------+
| id    | run    | subrun | string_hub | dom_position | brightness | window | delay | mask | rate  |
+-------+--------+--------+------------+--------------+------------+--------+-------+------+-------+
| 29229 | 114661 |      2 |      29229 |        29229 |      29229 |  29229 | 29229 | 2922 | 29229 |
+-------+--------+--------+------------+--------------+------------+--------+-------+------+-------+
1 row in set (0.00 sec)

run=114661 and subrun=3;
+-------+--------+--------+------------+--------------+------------+--------+-------+------+------+
```

```
| id    | run    | subrun | string_hub | dom_position | brightness | window | delay | mask | rate |
+-------+--------+--------+------------+--------------+------------+--------+-------+------+------+
| 29230 | 114661 |      3 |         63 |            2 |         20 |     25 |     0 | 0100 |  300 |
| 29231 | 114661 |      3 |         63 |            8 |         43 |     25 |     0 | 0200 |  300 |
| 29232 | 114661 |      3 |         63 |           14 |         11 |     25 |     0 | 0040 |  300 |
| 29233 | 114661 |      3 |         63 |           20 |         15 |     25 |     0 | 0800 |  300 |
| 29234 | 114661 |      3 |         63 |           26 |         13 |     25 |     0 | 0040 |  300 |
| 29235 | 114661 |      3 |         63 |           32 |         35 |     25 |     0 | 0040 |  300 |
| 29236 | 114661 |      3 |         63 |           38 |         31 |     20 |     0 | 0200 |  300 |
| 29237 | 114661 |      3 |         63 |           44 |         13 |     25 |     0 | 0100 |  300 |
| 29238 | 114661 |      3 |         63 |           50 |         23 |     20 |     0 | 0400 |  300 |
| 29239 | 114661 |      3 |         63 |           56 |         17 |     25 |     0 | 0040 |  300 |
+-------+--------+--------+------------+--------------+------------+--------+-------+------+------+
10 rows in set (0.00 sec)

run=114661 and subrun=4;
+-------+--------+--------+------------+--------------+------------+--------+-------+------+-------+
| id    | run    | subrun | string_hub | dom_position | brightness | window | delay | mask | rate  |
+-------+--------+--------+------------+--------------+------------+--------+-------+------+-------+
| 29240 | 114661 |      4 |      29240 |        29240 |      29240 |  29240 | 29240 | 2924 | 29240 |
+-------+--------+--------+------------+--------------+------------+--------+-------+------+-------+
1 row in set (0.00 sec)

run=114661 and subrun=5;
+-------+--------+--------+------------+--------------+------------+--------+-------+------+------+
| id    | run    | subrun | string_hub | dom_position | brightness | window | delay | mask | rate |
+-------+--------+--------+------------+--------------+------------+--------+-------+------+------+
| 29241 | 114661 |      5 |         63 |            4 |         17 |     20 |     0 | 0040 |  300 |
| 29242 | 114661 |      5 |         63 |           10 |         21 |     20 |     0 | 0800 |  300 |
| 29243 | 114661 |      5 |         63 |           16 |         22 |     20 |     0 | 0080 |  300 |
| 29244 | 114661 |      5 |         63 |           22 |          9 |     25 |     0 | 0040 |  300 |
| 29245 | 114661 |      5 |         63 |           28 |         17 |     20 |     0 | 0400 |  300 |
| 29246 | 114661 |      5 |         63 |           34 |        103 |     20 |     0 | 0100 |  300 |
| 29247 | 114661 |      5 |         63 |           40 |         23 |     20 |     0 | 0400 |  300 |
| 29248 | 114661 |      5 |         63 |           46 |         11 |     25 |     0 | 0400 |  300 |
| 29249 | 114661 |      5 |         63 |           52 |         20 |     21 |     0 | 0040 |  300 |
| 29250 | 114661 |      5 |         63 |           58 |         11 |     25 |     0 | 0100 |  300 |
+-------+--------+--------+------------+--------------+------------+--------+-------+------+------+
10 rows in set (0.00 sec)

run=114661 and subrun=6;
+-------+--------+--------+------------+--------------+------------+--------+-------+------+-------+
| id    | run    | subrun | string_hub | dom_position | brightness | window | delay | mask | rate  |
+-------+--------+--------+------------+--------------+------------+--------+-------+------+-------+
| 29251 | 114661 |      6 |      29251 |        29251 |      29251 |  29251 | 29251 | 2925 | 29251 |
+-------+--------+--------+------------+--------------+------------+--------+-------+------+-------+
1 row in set (0.00 sec)

run=114661 and subrun=7;
+-------+--------+--------+------------+--------------+------------+--------+-------+------+------+
```

```
| id    | run    | subrun | string_hub | dom_position | brightness | window | delay | mask | rate |
+-------+--------+--------+------------+--------------+------------+--------+-------+------+------+
| 29252 | 114661 |      7 |         63 |            4 |         18 |     20 |     0 | 0200 |  300 |
| 29253 | 114661 |      7 |         63 |           10 |         34 |     20 |     0 | 0100 |  300 |
| 29254 | 114661 |      7 |         63 |           16 |         15 |     25 |     0 | 0400 |  300 |
| 29255 | 114661 |      7 |         63 |           22 |         22 |     20 |     0 | 0200 |  300 |
| 29256 | 114661 |      7 |         63 |           28 |         11 |     25 |     0 | 0080 |  300 |
| 29257 | 114661 |      7 |         63 |           34 |        127 |     20 |     0 | 0800 |  300 |
| 29258 | 114661 |      7 |         63 |           40 |         15 |     25 |     0 | 0080 |  300 |
| 29259 | 114661 |      7 |         63 |           46 |         14 |     25 |     0 | 0080 |  300 |
| 29260 | 114661 |      7 |         63 |           52 |         12 |     25 |     0 | 0200 |  300 |
| 29261 | 114661 |      7 |         63 |           58 |         25 |     20 |     0 | 0800 |  300 |
+-------+--------+--------+------------+--------------+------------+--------+-------+------+------+
10 rows in set (0.00 sec)

run=114661 and subrun=8;
+-------+--------+--------+------------+--------------+------------+--------+-------+------+-------+
| id    | run    | subrun | string_hub | dom_position | brightness | window | delay | mask | rate  |
+-------+--------+--------+------------+--------------+------------+--------+-------+------+-------+
| 29262 | 114661 |      8 |      29262 |        29262 |      29262 |  29262 | 29262 | 2926 | 29262 |
+-------+--------+--------+------------+--------------+------------+--------+-------+------+-------+
1 row in set (0.00 sec)

run=114661 and subrun=9;
+-------+--------+--------+------------+--------------+------------+--------+-------+------+------+
| id    | run    | subrun | string_hub | dom_position | brightness | window | delay | mask | rate |
+-------+--------+--------+------------+--------------+------------+--------+-------+------+------+
| 29263 | 114661 |      9 |         63 |            6 |         28 |     20 |     0 | 0800 |  300 |
| 29264 | 114661 |      9 |         63 |           12 |         20 |     20 |     0 | 0080 |  300 |
| 29265 | 114661 |      9 |         63 |           18 |         12 |     25 |     0 | 0800 |  300 |
| 29266 | 114661 |      9 |         63 |           24 |         18 |     20 |     0 | 0800 |  300 |
| 29267 | 114661 |      9 |         63 |           30 |         19 |     20 |     0 | 0100 |  300 |
| 29268 | 114661 |      9 |         63 |           42 |         14 |     24 |     0 | 0100 |  300 |
| 29269 | 114661 |      9 |         63 |           48 |         18 |     24 |     0 | 0200 |  300 |
| 29270 | 114661 |      9 |         63 |           54 |         14 |     25 |     0 | 0800 |  300 |
| 29271 | 114661 |      9 |         63 |           60 |         25 |     20 |     0 | 0040 |  300 |
+-------+--------+--------+------------+--------------+------------+--------+-------+------+------+
9 rows in set (0.00 sec)

run=114661 and subrun=10;
+-------+--------+--------+------------+--------------+------------+--------+-------+------+-------+
| id    | run    | subrun | string_hub | dom_position | brightness | window | delay | mask | rate  |
+-------+--------+--------+------------+--------------+------------+--------+-------+------+-------+
| 29272 | 114661 |     10 |      29272 |        29272 |      29272 |  29272 | 29272 | 2927 | 29272 |
+-------+--------+--------+------------+--------------+------------+--------+-------+------+-------+
1 row in set (0.00 sec)

run=114661 and subrun=11;
+-------+--------+--------+------------+--------------+------------+--------+-------+------+------+
| id    | run    | subrun | string_hub | dom_position | brightness | window | delay | mask | rate |
```

```
+-------+--------+--------+------------+--------------+------------+--------+-------+------+------+
| 29273 | 114661 |     11 |         63 |            6 |         33 |     20 |     0 | 0100 |  300 |
| 29274 | 114661 |     11 |         63 |           12 |         15 |     25 |     0 | 0400 |  300 |
| 29275 | 114661 |     11 |         63 |           18 |         19 |     25 |     0 | 0100 |  300 |
| 29276 | 114661 |     11 |         63 |           24 |         12 |     25 |     0 | 0100 |  300 |
| 29277 | 114661 |     11 |         63 |           30 |         16 |     25 |     0 | 0800 |  300 |
| 29278 | 114661 |     11 |         63 |           42 |         23 |     20 |     0 | 0800 |  300 |
| 29279 | 114661 |     11 |         63 |           48 |         29 |     20 |     0 | 0040 |  300 |
| 29280 | 114661 |     11 |         63 |           54 |         17 |     25 |     0 | 0100 |  300 |
| 29281 | 114661 |     11 |         63 |           60 |         15 |     25 |     0 | 0200 |  300 |
+-------+--------+--------+------------+--------------+------------+--------+-------+------+------+
9 rows in set (0.00 sec)
```

D.2 Run 114666 - Odd DOMs

Location: http://warehouse.icecube.wisc.edu/data/exp/IceCube/2009/calibration/SouthPole/1014/

```
run=114666 and subrun=1
+-------+--------+--------+------------+--------------+------------+--------+-------+------+------+
| id    | run    | subrun | string_hub | dom_position | brightness | window | delay | mask | rate |
+-------+--------+--------+------------+--------------+------------+--------+-------+------+------+
| 29283 | 114666 |      1 |         63 |            1 |         20 |     20 |     0 | 0100 |  300 |
| 29284 | 114666 |      1 |         63 |            7 |         19 |     25 |     0 | 0040 |  300 |
| 29285 | 114666 |      1 |         63 |           13 |         15 |     20 |     0 | 0100 |  300 |
| 29286 | 114666 |      1 |         63 |           19 |         20 |     20 |     0 | 0100 |  300 |
| 29287 | 114666 |      1 |         63 |           25 |         21 |     20 |     0 | 0200 |  300 |
| 29288 | 114666 |      1 |         63 |           31 |         22 |     20 |     0 | 0080 |  300 |
| 29289 | 114666 |      1 |         63 |           37 |         75 |     20 |     0 | 0800 |  300 |
| 29290 | 114666 |      1 |         63 |           43 |         26 |     20 |     0 | 0800 |  300 |
| 29291 | 114666 |      1 |         63 |           49 |         23 |     20 |     0 | 0040 |  300 |
| 29292 | 114666 |      1 |         63 |           55 |         12 |     24 |     0 | 0080 |  300 |
+-------+--------+--------+------------+--------------+------------+--------+-------+------+------+
10 rows in set (0.00 sec)

run=114666 and subrun=2;
+-------+--------+--------+------------+--------------+------------+--------+-------+------+-------+
| id    | run    | subrun | string_hub | dom_position | brightness | window | delay | mask | rate  |
+-------+--------+--------+------------+--------------+------------+--------+-------+------+-------+
| 29293 | 114666 |      2 |      29293 |        29293 |      29293 |  29293 | 29293 | 2929 | 29293 |
+-------+--------+--------+------------+--------------+------------+--------+-------+------+-------+
1 row in set (0.01 sec)

run=114666 and subrun=3;
+-------+--------+--------+------------+--------------+------------+--------+-------+------+------+
| id    | run    | subrun | string_hub | dom_position | brightness | window | delay | mask | rate |
+-------+--------+--------+------------+--------------+------------+--------+-------+------+------+
| 29294 | 114666 |      3 |         63 |            1 |         53 |     20 |     0 | 0800 |  300 |
```

```
| 29295 | 114666 |      3 |         63 |            7 |         57 |     20 |     0 | 0200 |  300 |
| 29296 | 114666 |      3 |         63 |           13 |         20 |     20 |     0 | 0800 |  300 |
| 29297 | 114666 |      3 |         63 |           19 |         27 |     20 |     0 | 0800 |  300 |
| 29298 | 114666 |      3 |         63 |           25 |         19 |     25 |     0 | 0040 |  300 |
| 29299 | 114666 |      3 |         63 |           31 |         35 |     20 |     0 | 0400 |  300 |
| 29300 | 114666 |      3 |         63 |           37 |        114 |     25 |     0 | 0100 |  300 |
| 29301 | 114666 |      3 |         63 |           43 |         30 |     20 |     0 | 0100 |  300 |
| 29302 | 114666 |      3 |         63 |           49 |         28 |     20 |     0 | 0200 |  300 |
| 29303 | 114666 |      3 |         63 |           55 |         16 |     25 |     0 | 0400 |  300 |
+-------+--------+--------+------------+--------------+------------+--------+-------+------+------+
10 rows in set (0.00 sec)

run=114666 and subrun=4;
+-------+--------+--------+------------+--------------+------------+--------+-------+------+-------+
| id    | run    | subrun | string_hub | dom_position | brightness | window | delay | mask | rate  |
+-------+--------+--------+------------+--------------+------------+--------+-------+------+-------+
| 29304 | 114666 |      4 |      29304 |        29304 |      29304 |  29304 | 29304 | 2930 | 29304 |
+-------+--------+--------+------------+--------------+------------+--------+-------+------+-------+
1 row in set (0.01 sec)

run=114666 and subrun=5;
+-------+--------+--------+------------+--------------+------------+--------+-------+------+------+
| id    | run    | subrun | string_hub | dom_position | brightness | window | delay | mask | rate |
+-------+--------+--------+------------+--------------+------------+--------+-------+------+------+
| 29305 | 114666 |      5 |         63 |            3 |          6 |     25 |     0 | 0080 |  300 |
| 29306 | 114666 |      5 |         63 |            9 |         14 |     25 |     0 | 0800 |  300 |
| 29307 | 114666 |      5 |         63 |           15 |         18 |     20 |     0 | 0080 |  300 |
| 29308 | 114666 |      5 |         63 |           21 |         21 |     21 |     0 | 0040 |  300 |
| 29309 | 114666 |      5 |         63 |           27 |          9 |     24 |     0 | 0200 |  300 |
| 29310 | 114666 |      5 |         63 |           33 |         73 |     25 |     0 | 0080 |  300 |
| 29311 | 114666 |      5 |         63 |           39 |         12 |     24 |     0 | 0400 |  300 |
| 29312 | 114666 |      5 |         63 |           45 |         10 |     25 |     0 | 0100 |  300 |
| 29313 | 114666 |      5 |         63 |           51 |         11 |     25 |     0 | 0040 |  300 |
| 29314 | 114666 |      5 |         63 |           57 |         13 |     25 |     0 | 0200 |  300 |
+-------+--------+--------+------------+--------------+------------+--------+-------+------+------+
10 rows in set (0.00 sec)

run=114666 and subrun=6;
+-------+--------+--------+------------+--------------+------------+--------+-------+------+-------+
| id    | run    | subrun | string_hub | dom_position | brightness | window | delay | mask | rate  |
+-------+--------+--------+------------+--------------+------------+--------+-------+------+-------+
| 29315 | 114666 |      6 |      29315 |        29315 |      29315 |  29315 | 29315 | 2931 | 29315 |
+-------+--------+--------+------------+--------------+------------+--------+-------+------+-------+
1 row in set (0.00 sec)

run=114666 and subrun=7;
+-------+--------+--------+------------+--------------+------------+--------+-------+------+------+
| id    | run    | subrun | string_hub | dom_position | brightness | window | delay | mask | rate |
+-------+--------+--------+------------+--------------+------------+--------+-------+------+------+
| 29316 | 114666 |      7 |         63 |            3 |         11 |     25 |     0 | 0400 |  300 |
```

```
| 29317 | 114666 |      7 |         63 |            9 |         33 |     25 |     0 | 0100 |  300 |
| 29318 | 114666 |      7 |         63 |           15 |         22 |     20 |     0 | 0400 |  300 |
| 29319 | 114666 |      7 |         63 |           21 |         18 |     25 |     0 | 0200 |  300 |
| 29320 | 114666 |      7 |         63 |           27 |         11 |     25 |     0 | 0040 |  300 |
| 29321 | 114666 |      7 |         63 |           33 |        127 |     25 |     0 | 0400 |  300 |
| 29322 | 114666 |      7 |         63 |           39 |         21 |     20 |     0 | 0080 |  300 |
| 29323 | 114666 |      7 |         63 |           45 |         16 |     25 |     0 | 0800 |  300 |
| 29324 | 114666 |      7 |         63 |           51 |         13 |     25 |     0 | 0200 |  300 |
| 29325 | 114666 |      7 |         63 |           57 |         15 |     25 |     0 | 0040 |  300 |
+-------+--------+--------+------------+--------------+------------+--------+-------+------+------+
10 rows in set (0.00 sec)

run=114666 and subrun=8;
+-------+--------+--------+------------+--------------+------------+--------+-------+------+-------+
| id    | run    | subrun | string_hub | dom_position | brightness | window | delay | mask | rate  |
+-------+--------+--------+------------+--------------+------------+--------+-------+------+-------+
| 29326 | 114666 |      8 |      29326 |        29326 |      29326 |  29326 | 29326 | 2932 | 29326 |
+-------+--------+--------+------------+--------------+------------+--------+-------+------+-------+
1 row in set (0.01 sec)

run=114666 and subrun=9;
+-------+--------+--------+------------+--------------+------------+--------+-------+------+------+
| id    | run    | subrun | string_hub | dom_position | brightness | window | delay | mask | rate |
+-------+--------+--------+------------+--------------+------------+--------+-------+------+------+
| 29327 | 114666 |      9 |         63 |            5 |          7 |     25 |     0 | 0400 |  300 |
| 29328 | 114666 |      9 |         63 |           11 |          9 |     25 |     0 | 0400 |  300 |
| 29329 | 114666 |      9 |         63 |           17 |         11 |     25 |     0 | 0800 |  300 |
| 29330 | 114666 |      9 |         63 |           23 |         11 |     25 |     0 | 0400 |  300 |
| 29331 | 114666 |      9 |         63 |           29 |         20 |     20 |     0 | 0040 |  300 |
| 29332 | 114666 |      9 |         63 |           41 |         10 |     25 |     0 | 0080 |  300 |
| 29333 | 114666 |      9 |         63 |           47 |         15 |     24 |     0 | 0100 |  300 |
| 29334 | 114666 |      9 |         63 |           53 |         12 |     25 |     0 | 0800 |  300 |
| 29335 | 114666 |      9 |         63 |           59 |         30 |     20 |     0 | 0200 |  300 |
+-------+--------+--------+------------+--------------+------------+--------+-------+------+------+
9 rows in set (0.00 sec)

run=114666 and subrun=10;
+-------+--------+--------+------------+--------------+------------+--------+-------+------+-------+
| id    | run    | subrun | string_hub | dom_position | brightness | window | delay | mask | rate  |
+-------+--------+--------+------------+--------------+------------+--------+-------+------+-------+
| 29336 | 114666 |     10 |      29336 |        29336 |      29336 |  29336 | 29336 | 2933 | 29336 |
+-------+--------+--------+------------+--------------+------------+--------+-------+------+-------+
1 row in set (0.00 sec)

run=114666 and subrun=11;
+-------+--------+--------+------------+--------------+------------+--------+-------+------+------+
| id    | run    | subrun | string_hub | dom_position | brightness | window | delay | mask | rate |
+-------+--------+--------+------------+--------------+------------+--------+-------+------+------+
| 29337 | 114666 |     11 |         63 |            5 |         24 |     20 |     0 | 0080 |  300 |
| 29338 | 114666 |     11 |         63 |           11 |         18 |     25 |     0 | 0080 |  300 |
```

```
| 29339 | 114666 |     11 |         63 |           17 |         18 |     25 |     0 | 0100 |  300 |
| 29340 | 114666 |     11 |         63 |           23 |         23 |     20 |     0 | 0080 |  300 |
| 29341 | 114666 |     11 |         63 |           29 |          8 |     25 |     0 | 0200 |  300 |
| 29342 | 114666 |     11 |         63 |           41 |         25 |     20 |     0 | 0400 |  300 |
| 29343 | 114666 |     11 |         63 |           47 |         11 |     25 |     0 | 0800 |  300 |
| 29344 | 114666 |     11 |         63 |           53 |         14 |     25 |     0 | 0100 |  300 |
| 29345 | 114666 |     11 |         63 |           59 |         20 |     25 |     0 | 0040 |  300 |
+-------+--------+--------+------------+--------------+------------+--------+-------+------+------+
9 rows in set (0.00 sec)
```

Appendix E

Processing data script

Below is the script that I used to process the data. The feature2ppclike module was made by Bart. In this module it is very important to specify which DOM the user wants flashed.

```
$#!/usr/bin/env python

from I3Tray import *
from os.path import expandvars;
import sys
import os
from glob import glob
from string import atof,atoi

load("libdataclasses")
load("libphys-services")
load("libdataio")
load("libflasher-fill")
load("libI3Db")
load("libicepick")
load("libpayload-parsing")
load("libdaq-decode")
load("libDOMcalibrator")
load("libFeatureExtractor") # added by Sarah
```

```
load("libflat-ntuple")   # added by Sarah
load("libDomTools")
load("feature2ppclike")

tray = I3Tray()

#tools = expandvars("$I3_TOOLS")

infile=sys.argv[1]

infile = infile.replace('.i3','')
outfile = infile + '_GDC_CAL_FLASHINFO_FEAT.i3'

infile = infile + '.i3'

inice_rawdata                = "InIceRawData"
  # the name of the "InIce raw" DOMlaunch series frame-object
icetop_rawdata               = "IceTopRawData"
 # the name of the "IceTop raw" DOMlaunch series frame-object
inice_beacon                 = "InIceBeaconHits"
  # the name of the "InIce beacon hits" DOMlaunch series frame-object
icetop_beacon                = "IceTopBeaconHits"
 # the name of the "IceTop beacon hits" DOMlaunch series frame-object
special_rawdata              = "SpecialRawData"
 # the name of the "special DOM" DOMlaunch series frame-object


i3_header_name               = "I3DAQEventHeader"
  # name of IceCube event header
i3_trigger_name              = "I3DAQTriggerHierarchy"
 # name of IceCube trigger
i3_buffer_name               = "I3DAQData"
  # name of raw IceCube buffer data
```

```
dbserver="dbs2.icecube.wisc.edu"
username="www"
workspace = expandvars("$I3_SRC")
#outdir=os.path.join("/home/icecube/sarah/Thesis/IC59_flasher/")
#i3outfilename = os.path.join(outdir, "SPS-CV-DATA-Run00115609_Subrun00000001_decoded.i3")


tray.AddService("I3DbOMKey2MBIDFactory","omkey2mbid")(
    ("host",dbserver),
    ("username",username),
    ("database","I3OmDb")
    )

tray.AddService("I3FlasherFillServiceFactory","flashfill")(
    ("Hostname",dbserver),
    ("Username",username),
    ("DatabaseName","I3OmDb")
    )

tray.AddService("I3ReaderServiceFactory","readerfactory")(
    ("Filename", infile),
#    ("SkipUnregistered",True)
    ("OmitGeometry",True),
    ("OmitCalibration",True),
    ("OmitStatus",True)
    )

tray.AddService("I3DbGeometryServiceFactory","geometry")(
    ("host",dbserver),
    ("username",username),
    ("database","I3OmDb")
    )
```

```
tray.AddService("I3DbCalibrationServiceFactory","calibration")(
    ("host",dbserver),
    ("username",username),
    ("database","I3OmDb")
    )

tray.AddService("I3DbDetectorStatusServiceFactory","status")(
    ("host",dbserver),
    ("username",username),
    ("database","I3OmDb")
    )



tray.AddService("I3PayloadParsingEventDecoderFactory","i3eventdecode")(
#    ("Year",2009),
    ("headerid",i3_header_name),
    ("triggerid",i3_trigger_name),
    ("specialdataid",special_rawdata),
    ("specialdataoms",[OMKey(0,91),OMKey(0,92)]),
    ("flasherdataid","Flasher"),
    ("CPUDataID","BeaconHits")
    )

tray.AddModule("I3Muxer","muxme")

tray.AddModule("I3FrameBufferDecode","i3decode")(
          ("BufferID",i3_buffer_name)
          )

tray.AddModule("I3FlasherFillModule","flashfillmodule")

tray.AddModule("I3IcePickModule<I3FlashersOnlyFilter>","flashfilter")(
("DiscardEvents", True)
)
```

```
tray.AddModule("I3DOMcalibrator","domcalibrator")(  #  also added by Sarah
    ("InputRawDataName","InIceRawData"),
    ("OutputATWDDataName","OfflineCalibratedATWD"),
    ("OutputFADCDataName","OfflineCalibratedFADC"),
    ( "CorrectPedestalDroopDualTau", True ),
    ( "FADCTimeOffset",              -15 ),
    ( "ATWDSaturationLevel",         900 ),
    ( "SubtractTransitTime",         True ),      # Default (new default)
    )

# Extract wafeform features
tray.AddModule( "I3FeatureExtractor", "OfflineFeatures" ) (
   ( "RawReadoutName",             "InIceRawData" ),          # ! Use cleand raw data
   ( "CalibratedFADCWaveforms",    "OfflineCalibratedFADC" ), # Default
   ( "CalibratedATWDWaveforms",    "OfflineCalibratedATWD" ), # Default
   ( "InitialPulseSeriesReco",     "OfflinePulseSeriesReco"), # param of this function
   ( "InitialHitSeriesReco",       "OfflineHitSeriesReco" ),  # Default
   ( "DisableHitSeries",           False ),
   ( "MaxNumHits",                 0 ),
   ( "FastPeakUnfolding",          0 ),    # ! Extract multiple pulses
   ( "FastFirstPeak",              15 ),   # ! always find 1 pulse at least
   ( "MinSpeWidth",                4 ),    # Default
   ( "MaxSpeWidth",                20 ),   # Default
   ( "ExclusionSize",              1 ),    # don't extract from FADC for 25 ns after ATWD
   ( "ADCThreshold",               1.8),   # Threshold at 1.8 times the hardware setting
   ( "TinyThreshold",              0.0 ),  # Don't suppress small pulses
   ( "PMTTransit",                 -1 )    # ! Don't do transit time correction
   )


#tray.AddModule("I3Writer","writer")(
 #    ("filename",outfile),
  #   ("SkipKeys",["CleanIceTopRawData","CleanInIceRawData","allHitsDirty","allHits"])
```

```
  #   )

tray.AddModule('I3feature2ppclike', 'feature2ppclike')(
      ('recohitname', 'OfflineHitSeriesReco'),
      ('selectflasher', True),
      ('flasherinfoname', 'flasher'),
      ('flasherstring', 63),
      ('flasherdom', 51),
      ('selectmask', False),
      ('mask', 64)
      )

tray.AddModule("Dump","dump")

tray.AddModule("TrashCan","trash")

tray.Execute()
tray.Finish()$
```

Bibliography

[1] James Cook. *The Voyages of Captain James Cook.* William Smith, 1776.

[2] Yuval Ne'eman, Yoram Kirsh, and James H. Stith. The particle hunters. *The Physics Teacher*, 26(4):251–252, 1988.

[3] Martinus J. G. Veltman. *Facts and Mysteries in Elementary Particle Physics.* World Scientific Publishing, 2003.

[4] F. Reines and C. L. Cowan. Detection of the free neutrino. *Phys. Rev.*, 92(3):830–831, Nov 1953.

[5] Jr. Cowan, C. L., F. Reines, F. B. Harrison, H. W. Kruse, and A. D. McGuire. Detection of the free neutrino: a confirmation. *Science*, 124(3212):103–104, 1956.

[6] Raj Gandhi, Chris Quigg, Mary Hall Reno, and Ina Sarcevic. Neutrino interactions at ultrahigh energies. *Phys. Rev. D*, 58(9):093009, Sep 1998.

[7] Eric B.Norman. Neutrino astronomy: A new window on the universe. *Sky and Telescope*, 70(2):101 – 104, August 1985. Sky Publishing Corportaion.

[8] The IceCube Collaboration. Icecube preliminary design document revision 1.24, 2001.

[9] Shigeru. Yoshida, Rie. Ishibashi, and Hiroko. Miyamoto. Propogation of extremely high energy leptons in earth: Implications for their detection by the icecube neutrino telescope. *Physical Review D*, 69, 2004.

[10] Ackermann et al. Optical properties of deep glacial ice at the south pole. *Journal of Geophysical Research*, 111:1–26, 2006.

[11] C.J. Moses C.A. Moyer R.A. Serway. *Modern Physics.* Thomsom Brooks/Cole, 2005.

[12] Tyce DeYoung. Neutrino astronomy with ice cube. *e-print archive arXiv:0906.4530 [astro-ph.HE]*, 2009.

[13] Spencer R. Klein. Icecube: A cubic kilomter radiation detector. The IceCube Collaboration, 2008.

[14] R. Abbasi, Y. Abdou, T. Abu-Zayyad, O. Actis, J. Adams, J.A. Aguilar, M. Ahlers, K. Andeen, J. Auffenberg, X. Bai, M. Baker, S.W. Barwick, R. Bay, J.L. Bazo Alba, K. Beattie, J.J. Beatty, S. Bechet, J.K. Becker, K.-H. Becker, M.L. Benabderrahmane, J. Berdermann, P. Berghaus, D. Berley, E. Bernardini, D. Bertrand, D.Z. Besson, M. Bissok, E. Blaufuss, D.J. Boersma, C. Bohm, S. Bser, O. Botner, L. Bradley, J. Braun, S. Buitink, M. Carson, D. Chirkin, B. Christy, J. Clem, F. Clevermann, S. Cohen, C. Colnard, D.F. Cowen, M.V. D'Agostino, M. Danninger, J.C. Davis, C. De Clercq, L. Demirrs, O. Depaepe, F. Descamps, P. Desiati, G. de Vries-Uiterweerd, T. DeYoung, J.C. Daz-Vlez, J. Dreyer, J.P. Dumm, M.R. Duvoort, R. Ehrlich, J. Eisch, R.W. Ellsworth, O. Engdegrd, S. Euler, P.A. Evenson, O. Fadiran, A.R. Fazely, T. Feusels, K. Filimonov, C. Finley, M.M. Foerster, B.D. Fox, A. Franckowiak, R. Franke, T.K. Gaisser, J. Gallagher, R. Ganugapati, M. Geisler, L. Gerhardt, L. Gladstone, T. Glsenkamp, A. Goldschmidt, J.A. Goodman, D. Grant, T. Griesel, A. Gro, S. Grullon, R.M. Gunasingha, M. Gurtner, C. Ha, A. Hallgren, F. Halzen, K. Han, K. Hanson, K. Helbing, P. Herquet, S. Hickford, G.C. Hill, K.D. Hoffman, A. Homeier, K. Hoshina, D. Hubert, W. Huelsnitz, J.-P. Hl, P.O. Hulth, K. Hultqvist, S. Hussain, R.L. Imlay, A. Ishihara, J. Jacobsen, G.S. Japaridze, H. Johansson, J.M. Joseph, K.-H. Kampert, A. Kappes, T. Karg, A. Karle, J.L. Kelley, N. Kemming, P. Kenny, J. Kiryluk, F. Kislat, S.R. Klein, S. Knops, J.-H. Khne, G. Kohnen, H. Kolanoski, L. Kpke, D.J. Koskinen, M. Kowalski, T. Kowarik, M. Krasberg, T. Krings, G. Kroll, K. Kuehn, T. Kuwabara, M. Labare, S. Lafebre, K. Laihem, H. Landsman, R. Lauer, R. Lehmann, D. Lennarz, J. Lnemann, J. Madsen, P. Majumdar, R. Maruyama, K. Mase, H.S. Matis, M. Matusik, K. Meagher, M. Merck, P. Mszros, T. Meures, E. Middell, N. Milke, J. Miller, T. Montaruli, R. Morse, S.M. Movit, R. Nahnhauer, J.W. Nam, U. Naumann, P. Nieen, D.R. Nygren, S. Odrowski, A. Olivas, M. Olivo, M. Ono, S. Panknin, L. Paul, C. Prez de los Heros, J. Petrovic, A. Piegsa, D. Pieloth, R. Porrata, J. Posselt, P.B. Price, M. Prikockis, G.T. Przybylski, K. Rawlins, P. Redl, E. Resconi, W. Rhode, M. Ribordy, A. Rizzo, J.P. Rodrigues, P. Roth, F. Rothmaier, C. Rott, C. Roucelle, T. Ruhe, D. Rutledge, B. Ruzybayev, D. Ryckbosch, H.-G. Sander, S. Sarkar, K. Schatto, S. Schlenstedt, T. Schmidt, D. Schneider, A. Schukraft, A. Schultes, O. Schulz, M. Schunck, D. Seckel, B. Semburg, S.H. Seo, Y. Sestayo, S. Seunarine, A. Silvestri, A. Slipak, G.M. Spiczak, C. Spiering, M. Stamatikos, T. Stanev, G. Stephens, T. Stezelberger, R.G. Stokstad, S. Stoyanov, E.A. Strahler, T. Straszheim, G.W. Sullivan, Q. Swillens, I. Taboada, A. Tamburro, A. Tepe, S. Ter-Antonyan, S. Tilav, P.A. Toale, D. Tosi, D. Turcan, N. van Eijndhoven, J. Vandenbroucke, A. Van Overloop, J. van Santen, B. Voigt, C. Walck, T. Waldenmaier, M. Wallraff, M. Walter, C. Wendt, S. Westerhoff, N. Whitehorn, K. Wiebe, C.H. Wiebusch, G. Wikstrm, D.R.

Williams, R. Wischnewski, H. Wissing, K. Woschnagg, C. Xu, X.W. Xu, G. Yodh, S. Yoshida, and P. Zarzhitsky. Search for neutrino-induced cascades with five years of amanda data. *Astroparticle Physics*, In Press, Corrected Proof:–, 2010.

[15] F. Halzen. Astroparticle physics with high energy neutrinos: from amanda to icecube. *The European Physical Journal C - Particles and Fields*, 46:669–687, 2006. 10.1140/epjc/s2006-02536-4.

[16] Francis Halzen and Spencer R. Klein. IceCube: An Instrument for Neutrino Astronomy. 2010.

[17] Marek Paul Kowalski. *Search for Neutrino-Induced Cascades with the AMANDA-II Detector*. PhD thesis, 2004.

[18] John David Jackson. *Classical Electrodynamics*. John Wiley and Sons, Inc, third edition, 1999.

[19] R. Abbasi et al. Calibration and Characterization of the IceCube Photomultiplier Tube. *Nucl. Instrum. Meth.*, A618:139–152, 2010.

[20] J. Babson, B. Barish, R. Becker-Szendy, H. Bradner, R. Cady, J. Clem, S. T. Dye, J. Gaidos, P. Gorham, P. K. F. Grieder, M. Jaworski, T. Kitamura, W. Kropp, J. G. Learned, S. Matsuno, R. March, K. Mitsui, D. O'Connor, Y. Ohashi, A. Okada, V. Peterson, L. Price, F. Reines, A. Roberts, C. Roos, H. Sobel, and V. J. Stenger. Cosmic-ray muons in the deep ocean. *Phys. Rev. D*, 42(11):3613–3620, Dec 1990.

[21] DUMAND collaboration. Deep underwater muon and neutrino detection. http://www.phys.hawaii.edu/~dumand/, 2010.

[22] Vasilij Balkanov, Igor Belolaptikov, Leonid Bezrukov, Aleksander Chensky, Nikolaij Budnev, Igor Danilchenko, Zhan-Arys Dzhilkibaev, Grigorij Domogatsky, Aleksander Doroshenko, Stanislav Fialkovsky, Oleg Gaponenko, Anatolij Garus, Tatiana Gress, Albrecht Karle, Arkadij Klabukov, Anatolij Klimov, Sergeij Klimushin, Andreij Koshechkin, Viktor Kulepov, Leonid Kuzmichev, Bajarto Lubsandorzhiev, Sergeij Lovzov, Thomas Mikolajski, Michail Milenin, Rashid Mirgazov, Andreij Moroz, Nikolaij Moseiko, Semen Nikiforov, Eleonora Osipova, Dirk Pandel, Andreij Panfilov, Yurij Parfenov, Anatolij Pavlov, Dmitrij Petukhov, Pavel Pokhil, Peter Pokolev, Elena Popova, Michail Rozanov, Valerij Rubzov, Igor Sokalski, Christian Spiering, Ole Streicher, Boris Tarashansky, Thorsten Thon, Ralf Wischnewski, and Ivan Yashin. In situ measurements of optical parameters in lake baikal with the help of a neutrino telescope. *Appl. Opt.*, 38(33):6818–6825, 1999.

[23] V. Aynutdinov and V. Balkanov and I. Belolaptikov and L. Bezrukov and D. Borschov and N. Budnev and A. Chensky and I. Danilchenko and Ya. Davidov and G. Domogatsky and A. Doroshenko and

A. Dyachok and Zh.-A. Dzhilkibaev and S. Fialkovsky and O. Gaponenko and O. Gress and T. Gress and O. Grishin and A. Klabukov and A. Klimov and S. Klimushin and K. Konischev and A. Koshechkin and L. Kuzmichev and V. Kulepov and B. Lubsandorzhiev and S. Mikheyev and T. Mikolajski and M. Milenin and R. Mirgazov and E. Osipova and A. Pavlov and G. Pan'kov and L. Pan'kov and A. Panfilov and Yu. Parfenov and D. Petukhov and E. Pliskovsky and P. Pokhil and V. Poleschuk and E. Popova and V. Prosin and M. Rozanov and V. Rubtzov and Yu. Semeney and B. Shaibonov and A. Shirokov and Ch. Spiering and B. Tarashansky and R. Vasiliev and E. Vyatchin and R. Wischnewski and I. Yashin and V. Zhukov. Search for a diffuse flux of high-energy extraterrestrial neutrinos with the nt200 neutrino telescope. *Astroparticle Physics*, 25(2):140–150, 2006.

[24] Antoine Kouchner. Antares and other neutrino telescopes in the northern hemisphere. *NUCLEAR PHYSICS B-PROCEEDINGS SUPPLEMENTS*, 196:273–278, DEC 2009. 15th International Symposium on Very High Energy Interactions, Paris, FRANCE, SEP 01-06, 2008.

[25] KM3NeT collaboration. website. http://www.km3net.org/home.php, Accessed: May 2010.

[26] NESTOR collaboration. Nestor institute for deep sea research, technology and neutrino astroparticle physics. http://www.nestor.noa.gr/, 2010.

[27] NEMO collaboration. Neutrino mediterranean observatory. http://nemoweb.lns.infn.it/index.htm, 2010.

[28] ANTARES collaboration. website. http://antares.in2p3.fr/, Accessed: May 2010.

[29] Stephan Hundertmark and Antoine Kouchner. High energy neutrino astronomy. *Comptes Rendus Physique*, 6(7):789–797, 2005. Neutrino physics.

[30] VA Zhukov, A Aloupis, EG Anassontzis, N Arvanitis, A Babalis, A Ball, LB Bezrukov, G Bourlis, AV Butkevich, W Chinowsky, PE Christopoulos, A Darsaklis, LG Dedenko, D Elstrup, E Fahrun, J Gialas, C Goudis, G Grammatikakis, C Green, PKF Grieder, SK Karaevsky, P Katrivanos, U Keussen, J Kiskiras, T Knutz, D Korostylev, K Komlev, J Kontakxis, P Koske, JG Learned, VV Ledenev, A Leisos, G Limberopoulos, J Ludvig, J Makris, A Manousakis-Katsikakis, E Markopoulos, S Matsuno, J Mielke, T Mihos, P Minkowski, AA Mironovich, R Mitiguy, S Nounos, DR Nygren, K Papageorgiou, M Passera, C Politis, P Preve, GT Prybylsky, J Rathley, LK Resvanis, M Rosen, N Schmidt, T Schmidt, I Siotis, AE Shnyrev, J Sopher, T Staveris, G Stavrakakis, R Stokstad, NM Surin, V Tsagli, A Tsirigotis, J Tsirmpas, S Tzamarias, O Vasiliev, O Vaskin, W Voigt,

A Vougioukas, G Voulgaris, LM Zakharov, N Ziabko, and NESTOR Collaboration. NESTOR experiment in 2003. *PHYSICS OF ATOMIC NUCLEI*, 67(11):2054–2057, NOV 2004. 4th International Conference on Nonaccelerator New Physics, Dubna, RUSSIA, JUN 23-28, 2003.

[31] Paolo Piattelli. The neutrino mediterranean observatory project. *Nuclear Physics B - Proceedings Supplements*, 143:359–362, 2005. NEUTRINO 2004.

[32] JUAN JOSE HERNANDEZ-REY. The neutrino telescope antares. *Astrophysics and Space Science*, 297:257–267, 2005.

[33] Vincent Bertin. Status and first results of the antares neutrino telescope. *Nuclear Instruments and Methods in Physics Research Section A: Accelerators, Spectrometers, Detectors and Associated Equipment*, 604(1-2, Supplement 1):S136–S142, 2009. ARENA 2008.

[34] Gabrielle Lelaizant. Study on the possible detection of gamma ray bursts with the antares neutrino telescope. *Astrophysics Space Science*, 309:441–445, April 2007.

[35] C. Distefano. Km3net: towards a km3-scale neutrino telescope in the mediterranean sea. *Nuclear Physics B - Proceedings Supplements*, 190:115–120, 2009. Proceedings of the Cosmic Ray International Seminars.

[36] S. Barwick et al. Neutrino astronomy on the 1-KM**2 scale. *J. Phys.*, G18:225–248, 1992.

[37] P. O. Hulth et al. The AMANDA experiment. 1996.

[38] E. Andres, P. Askebjer, S. W. Barwick, R. Bay, L. Bergstrm, A. Biron, J. Booth, A. Bouchta, S. Carius, M. Carlson, D. Cowen, E. Dalberg, T. DeYoung, P. Ekstrm, B. Erlandson, A. Goobar, L. Gray, A. Hallgren, F. Halzen, R. Hardtke, S. Hart, Y. He, H. Heukenkamp, G. Hill, P. O. Hulth, S. Hundertmark, J. Jacobsen, A. Jones, V. Kandhadai, A. Karle, B. Koci, P. Lindahl, I. Liubarsky, M. Leuthold, D. M. Lowder, P. Marciniewski, T. Mikolajski, T. Miller, P. Miocinovic, P. Mock, R. Morse, P. Niessen, C. Prez de los Heros, R. Porrata, D. Potter, P. B. Price, G. Przybylski, A. Richards, S. Richter, P. Romenesko, H. Rubinstein, E. Schneider, T. Schmidt, R. Schwarz, M. Solarz, G. M. Spiczak, C. Spiering, O. Streicher, Q Sun, L. Thollander, T. Thon, S. Tilav, C. Walck, C. Wiebusch, R. Wischnewski, K. Woschnagg, and G. Yodh. The amanda neutrino telescope: principle of operation and first results. *Astroparticle Physics*, 13(1):1 – 20, 2000.

[39] J.D. Zornoza. Results from the amanda neutrino telescope. *Nuclear Physics B - Proceedings Supplements*, 165:196 – 199, 2007. Proceedings of the Cosmic Ray International Seminars, Proceedings of the Cosmic Ray International Seminars.

[40] M. Ackermann, J. Ahrens, X. Bai, M. Bartelt, S.W. Barwick, R. Bay, T. Becka, J.K. Becker, K.-H. Becker, E. Bernardini, D. Bertrand, D.J. Boersma, S. Böser, O. Botner, A. Bouchta, O. Bouhali, J. Braun, C. Burgess, T. Burgess, T. Castermans, W. Chinowsky, D. Chirkin, J. Conrad, J. Cooley, D.F. Cowen, A. Davour, C. De Clercq, T. DeYoung, P. Desiati, P. Ekström, T. Feser, M. Gaug, T.K. Gaisser, R. Ganugapati, H. Geenen, L. Gerhardt, A. Goldschmidt, A. Groß, A. Hallgren, F. Halzen, K. Hanson, R. Hardtke, T. Harenberg, T. Hauschildt, K. Helbing, M. Hellwig, P. Herquet, G.C. Hill, D. Hubert, B. Hughey, P.O. Hulth, K. Hultqvist, S. Hundertmark, J. Jacobsen, K.H. Kampert, A. Karle, J.L. Kelley, M. Kestel, G. Kohnen, L. Köpke, M. Kowalski, M. Krasberg, K. Kuehn, H. Leich, M. Leuthold, I. Liubarsky, J. Ludvig, J. Lundberg, J. Madsen, P. Marciniewski, H.S. Matis, C.P. McParland, T. Messarius, Y. Minaeva, P. Miocinovic, R. Morse, K.S. Münich, R. Nahnhauer, J. Nam, T. Neunhöffer, P. Niessen, D.R. Nygren, H. Ögelman, Ph. Olbrechts, C. Pérez de los Heros, A.C. Pohl, R. Porrata, P.B. Price, G.T. Przybylski, K. Rawlins, E. Resconi, W. Rhode, M. Ribordy, S. Richter, S. Robbins, J. Rodríguez Martino, H.-G. Sander, S. Schlenstedt, D. Schneider, R. Schwarz, A. Silvestri, M. Solarz, J. Sopher, G.M. Spiczak, C. Spiering, M. Stamatikos, D. Steele, P. Steffen, R.G. Stokstad, K.-H. Sulanke, I. Taboada, L. Thollander, S. Tilav, W. Wagner, C. Walck, M. Walter, Y.-R. Wang, C. Wendt, C.H. Wiebusch, R. Wischnewski, H. Wissing, K. Woschnagg, and G. Yodh. The icecube prototype string in amanda. *Nuclear Instruments and Methods in Physics Research Section A: Accelerators, Spectrometers, Detectors and Associated Equipment*, 556(1):169–181, 2006.

[41] The antarctic treaty, opend for Signatures 1 December 1959. 402 UNITS 71, art 72 (entered into force 23 June1961).

[42] *Protocol on Environmental Protection to the Antarctic Treaty.* The Antarctic Treay system, opened for signature on 4 October 1991. 30 ILM (1991) (entered into force 14 January 1998).

[43] National Science Foundation. Project icecube comprehensive environmental evaluation. 2004.

[44] Miocinovic Predrag. Muon energy reconstruction in the antarctic muon and neutrino detector array (amanda). UMI-30-62680.

[45] Per Askebjer, Steven W. Barwick, Lars Bergström, Adam Bouchta, Staffan Carius, Eva Dalberg, Kevin Engel, Bengt Erlandsson, Ariel Goobar, Lori Gray, Allan Hallgren, Francis Halzen, Hans Heukenkamp, Per Olof Hulth, Stephan Hundertmark, John Jacobsen, Albrecht Karle, Vijaya Kandhadai, Igor Liubarsky, Doug Lowder, Tim Miller, Pat Mock, Robert M. Morse, Rodin Porrata, P. Buford Price, Austin Richards, Hector Rubinstein, Eric Schneider, Christian Spiering, Ole Streicher, Qin Sun, Thorsten Thon, Serap Tilav, Ralf Wischnewski, Christian Walck, and Gaurang B.

Yodh. Optical properties of deep ice at the south pole: absorption. *Appl. Opt.*, 36(18):4168–4180, Jun 1997.

[46] L. G. Henyey and J. L. Greenstein. Diffuse radiation in the Galaxy. *Annales d'Astrophysique*, 3:117–+, jan 1940.

[47] P. Buford Price and Lars Bergström. Optical properties of deep ice at the south pole: scattering. *Appl. Opt.*, 36(18):4181–4194, Jun 1997.

[48] Dmitry Chirkin. Study of ice transparency with icecube flashers. IceCube Collaboration, University of Wisconsin.

[49] IceCube collaboration. Aha wiki page. http://wiki.icecube.wisc.edu/index.php/Aha, May 2008.

[50] IceCube collaboration. Spice 2 dust logger tilt webpage. http://icecube.wisc.edu/~dima/work/WISC/ppc/fit/tilt/model/, 2009.

[51] Dimitry Chirkin. Spice powerpoint. presented at IceCube collaboration meeting, September 2010.

[52] Dimitry Chirkin. ppc readme files. http://icecube.wisc.edu/~dima/stuff/, 2010.

[53] Pingyu Liu. A new phase function approximating to mie scattering for radiative transport equations. *Physics in Medicine and Biology*, 39(6):1025, 1994.

[54] Dimitry Chirkin. Photon propagation code powerpoint. presented at IceCube collaboration meeting, 2010.

[55] J. Lundberg, P. Miocinovic, K. Woschnagg, T. Burgess, J. Adams, S. Hundertmark, P. Desiati, and P. Niessen. Light tracking through ice and water–scattering and absorption in heterogeneous media with photonics. *Nuclear Instruments and Methods in Physics Research Section A: Accelerators, Spectrometers, Detectors and Associated Equipment*, 581(3):619–631, 2007.

[56] Christopher Wendt. Personal correspondance, December 2010.

[57] Christopher Wendt. String 63 azimuthal orientation fits. http://icecube.wisc.edu/~chwendt/string-63-azimuthal-orientation-fits/, 2010.

[58] Dawn Williams. Status of flasher runs. Presented at IceCube collaboration meeting, May 2011.